DISSERTATIONES
SCIENTIAE
MATERIALIS
UNIVERSITATIS
TARTUENSIS
41

MAHTAB SALARI MEHR

Microstructure optimization of atomic layer deposited chromium-containing ternary compound thin films

DISSERTATIONES SCIENTIAE MATERIALIS UNIVERSITATIS TARTUENSIS
41

DISSERTATIONES SCIENTIAE MATERIALIS UNIVERSITATIS TARTUENSIS
41

MAHTAB SALARI MEHR

Microstructure optimization of atomic layer deposited chromium-containing ternary compound thin films

UNIVERSITY OF TARTU
Press
1632

Institute of Physics, Faculty of Science and Technology, University of Tartu.

The Dissertation was admitted on July 1, 2026, in partial fulfillment of the requirements for the degree of Doctor of Philosophy in Materials Science and was allowed for defense by the Scientific Council on Materials Science of the Faculty of Science and Technology, University of Tartu.

Supervisors: Dr. Hugo Mändar, Associate Professor in Materials Science, Institute of Physics, University of Tartu.

Dr. Lauri Aarik, Research Fellow in Materials Science, Institute of Physics, University of Tartu

Dr. Taivo Jõgiaas, Research Fellow in Materials Science, Institute of Physics, University of Tartu

Opponents: Dr. Per Eklund, Professor in Materials Chemistry, Department of Chemistry, Ångström Laboratory, Uppsala University

Dr. Henrik Pedersen, Professor in Inorganic Chemistry, Department of Physics, Chemistry and Biology, Linköping University

Defense: September 2, 2026, University of Tartu, Estonia

The research was funded by the Estonian Research Council (ERS grants TEM-TA25, TEM-TA31, PSG448, PRG2594), the Center of Excellence in Sustainable Green Hydrogen and Energy Technologies (grant TK210U5) and the European Regional Development Fund (TK134 “Emerging orders in quantum and nanomaterials”).

ISSN 2228-0928 (print)
ISBN 978-9908-57-309-0 (print)
ISSN 2806-2574 (pdf)
ISBN 978-9908-57-310-6 (pdf)

University of Tartu Press
www.tyk.ee

CONTENTS

ORIGINAL PUBLICATIONS and AUTHOR CONTRIBUTION

I. Mahtab Salari Mehr, Lauri Aarik, Taivo Jõgiaas, Aarne Kasikov, Jekaterina Kozlova, Loïc Vidal, Karine Mougin, Hugo Mändar, "Atomic Layer Deposition, Mechanical, Wear Resistance, and Optical Properties of $(Cr_{1-x}Al_x)_2O_3$ Films on Si (100)", 50 (2024) 50367–50376, Ceramics International, https://doi.org/10.1016/j.ceramint.2024.09.382.

Author's contribution: Participation in preparation of the films by atomic layer deposition. Characterization of the films using X-ray diffraction, X-ray reflectivity, transmission electron microscopy, nanoindentation, scanning probe microscopy, and spectroscopic ellipsometry. Preparation of the original draft.

II. Mahtab Salari Mehr, Lauri Aarik, Taivo Jõgiaas, Hugo Mändar, "Annealing Effect on Structural and Mechanical Properties of Atomic Layer Deposited Cr_2O_3 Films Doped with Ti and Al", IEEE conference (NAP) Proceedings, 2024, https://doi.org/10.1109/NAP62956.2024.10739705.

Author's contribution: In situ high-temperature X-ray diffraction, X-ray reflectivity measurements in the X-ray diffractometer. Characterization of the films using nanoindentation. Preparation of the original draft.

III. Mahtab Salari Mehr, Lauri Aarik, Taivo Jõgiaas, Aarne Kasikov, Elyad Damerchi, Hugo Mändar, "Mechanical and Optical Properties of Cr_2O_3 Thin Films Grown by Atomic Layer Deposition Method Using Cr $(thd)_3$ and Ozone." Nanomaterials, 13 (2023) 2702, https://doi.org/10.3390/nano13192702.

Author's contribution: Participation in preparation of the ternary Cr-Ti-O films by ALD. Characterization of atomic layer deposited binary Cr_2O_3 films and ternary Cr-Ti-O films using X-ray diffraction, X-ray reflectivity, nanoindentation, and spectroscopic ellipsometry. Preparation of the original draft.

IV. Mahtab Salari Mehr, Lauri Aarik, Taivo Jõgiaas, Aivar Tarre, Aarne Kasikov, Kaspar Roosalu, Hugo Mändar, "Ti doped Cr_2O_3 Thin Films: Atomic Layer Deposition, Mechanical and Optical Properties", Journal of Alloys and Compounds, 968 (2023) 172041, https://doi.org/10.1016/j.jallcom.2023.172041.
Author's contribution: Characterization of films using X-ray diffraction, X-ray reflectivity, nanoindentation, spectroscopic ellipsometry. Preparation of the original draft.

V. Mahtab Salari Mehr, Lauri Aarik, Taivo Jõgiaas, Aarne Kasikov, Tanel Käämbre, Rainer Pärna, Ramin Ghiyasi, Maarit Karppinen, Hugo Mändar, "Structural, Mechanical, and Optical properties of Atomic Layer Deposited $(Cr_{1-x}Al_x)_2O_3$ films on sapphire substrates", Materials Advances, 2026 (accepted, in print)

Author's contribution: Participation in the preparation of the films by ALD. Participation in the characterization of the phase composition and crystal quality of the films using high-resolution X-ray diffraction. Characterization of the films using X-ray reflectivity, nanoindentation, and spectroscopic ellipsometry. Preparation of the original draft.

ABBREVIATIONS

ALD	atomic layer deposition
Me	Ti, Al, Hf
XRF	X-ray fluorescence spectroscopy
GIXRD	grazing incidence X-ray diffraction analysis
α	incidence angle
α_c	critical angle of total external X-ray reflection
2θ	X-ray diffraction angle
HRHRD	high-resolution X-ray diffraction
XRR	X-ray reflectivity
XAS	X-ray absorption spectroscopy
XPS	X-ray photoelectron spectroscopy
HRTEM	high-resolution transmission electron microscopy
EDX (EDS)	energy-dispersive X-ray spectroscopy
FWHM	full width at half maximum
λ	wavelength
SPM	scanning probe microscopy
CTO	chromium titanium oxide
CAO	chromium aluminum oxide
CHO	chromium hafnium oxide
PLD	pulse laser deposition
PVD	physical vapor deposition
CVD	chemical vapor deposition
T_G	growth/deposition temperature
RF	radio frequency
H	hardness
E	elastic modulus
E_g	optical band gap
n	refractive index
k	extinction coefficient
ϕ (φ)	phi-scan
RT	room temperature
MEMS/NEMS	micro/nano-electromechanical systems
t	thickness
ρ	density
$<D>_v$	X-ray apparent volume weighted mean crystallite size
ID	indent displacement

THE CLAIM OF THE THESIS

This thesis demonstrates that the optical, mechanical, and tribological properties of chromium oxide thin films, synthesized by atomic layer deposition (ALD) using the novel chromium precursor of $Cr(thd)_3$, can be systematically engineered by controlling the composition of ternary $(Cr,Me)_2O_3$ films, where Me = Ti, Al, Hf. The work establishes ALD processes through precursor selection and parameter optimization, and shows that compositional control enables targeted tuning of film structure and functional properties. It further claims that the choice of substrate can affect film structure, mechanical and optical performance, and in the case of ternary $(Cr,Al)_2O_3$, and $(Cr,Ti)_2O_3$ films, the thermal phase compositional stability is remarkably increased compared with that of binary Cr_2O_3. Overall, this work establishes a pathway to engineer ALD-grown ultra-thin films with tailored properties that are not achievable in binary-component Cr_2O_3 films, thereby expanding their industrial applicability.

1. INTRODUCTION

Chromium (III) oxide (Cr_2O_3, with mineral name eskolaite) is a multifunctional ceramic material that has attracted attention for a wide range of protective and electronic applications because of its unique combination of outstanding mechanical, chemical, and multifunctional electronic properties. Bulk Cr_2O_3 is among the hardest oxides (reported hardness up to ~ 44.7 GPa) and exhibits high wear resistance, low friction, and excellent corrosion resistance, making it an excellent candidate for protective and tribological coatings [1,2,3]. At the same time, Cr_2O_3 is a p-type semiconductor [4,5] with useful magnetoelectric responses [6], and its optical and magnetic [7,8] characteristics make it promising for application in magneto-optical components, spintronics, non-volatile magneto-electric memory devices, MEMS, and integrated device architectures [6,9–12].

Considering these applications, the effort on tailoring properties of Cr_2O_3 thin films has continued to meet the technological demands. For instance, the optical bandgap and magnetic response must be adjustable for magneto-optical and spintronic technologies [6–9], strong adhesion together with compatible thermal expansion [13] is essential when Cr_2O_3 serves as an interlayer, or diffusion barrier [13,14], or hard coating serving as a surface protection layer [2,3,12,15]. This has motivated continued research on precise deposition and chemical modification of Cr_2O_3-based films.

One powerful route to property engineering is the creation of ternary (and co-doped) chromium-oxide films. Introducing selected cationic or anionic dopants or forming Cr-Me-O ternaries permits deliberate tuning of carrier concentration [16], bandgap [17–19], mechanical [20], corrosion resistance [21], and barrier performance [22].

Atomic layer deposition (ALD) is particularly well suited to address these challenges because it enables atomic-scale thickness control, conformal coverage over complex geometries, and precise doping/stoichiometry control, all essential for device integration [23–26]. ALD chemistry for Cr_2O_3 has been shifted from early processes based on chromyl chloride (CrO_2Cl_2) [27], being a Cr(VI) precursor with high environmental and health concerns, toward Cr(III) β-diketonate precursors [28] in combination with strong oxidants (e.g., O_3). This transition reduces reliance on Cr(VI) halide precursors but still does not eliminate whole process hazards, because reactive oxidants and volatile reaction products (including ligand-derived organics and potentially corrosive species in halide-based chemistries) still require appropriate handling [29].

This thesis investigates how ALD enables us to synthesize multicomponent films with controlled elemental composition and how the elemental composition variation could influence the mechanical properties, optical performance, and thermal stability of the oxide thin films.

2. BACKGROUND

2.1. Thin films prospective applications and deposition

The term of thin film refers to a thin layer of material that extends infinitely along any two directions, but is restricted along the third direction, and its thickness varies from a fraction of a nanometer to a few micrometers [30]. These films are routinely employed to alter surface characteristics of bulk materials or to create functional components or devices [30–32]. Bulk materials (i.e., films with a thickness of several microns or more) have fixed physical and chemical properties; however, when thickness reduces beyond a certain limit, the characteristics of the films begin to change drastically, enabling the achievement of unique properties. The thickness and structure of the films influence their various properties and performance [31–33]. The idea of thin films development back to the development of low-cost photovoltaics, and since the 1960s, thin-film technologies began to be implemented on an industrial scale for semiconductor and reflective applications [34]. Nowadays, thin film materials have been studying and considering for optical [35,36]; magnetic [37,38]; electrical [39,40]; thermal barrier layers [41–43]; chemical resistance [44]; sensor [45–47]; and protective [48,49] applications. A thin film forms when a material is grown on a solid substrate by controlled condensation of atomic, molecular, or ionic species by physical deposition or chemical deposition techniques (Figure 1). Physical deposition methods cover the techniques of thermal growth of solid films involving vaporization or sputtering of materials from a source while the chemical deposition methods result in the formation of thin films on a solid substrate by reaction of chemical constituents. The various methods of thin film fabrication have been mentioned in the form of a flowchart in Figure 1. Based on the needs, characteristics, and application of the films, the deposition technique can be selected [50].

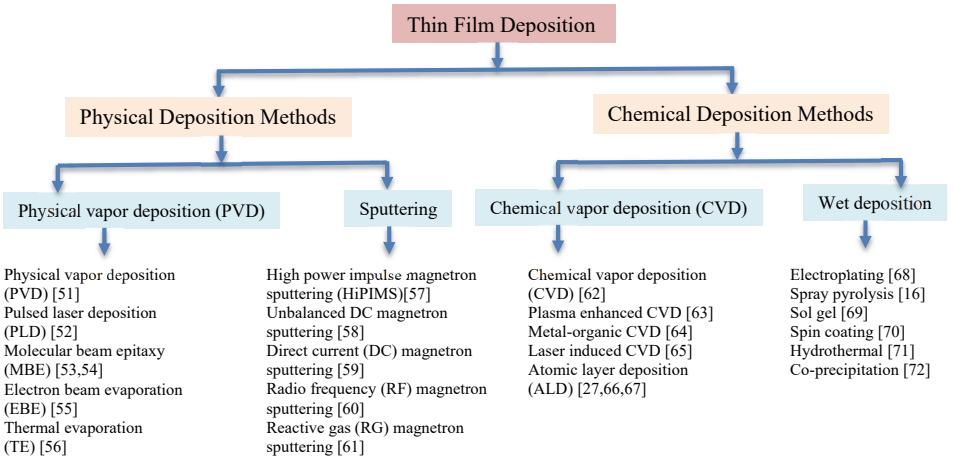

Figure 1. Category of various methods of thin film fabrication.

2.2. Chromium oxide films, their prospective properties and applications

The transition metal oxides (TMOs) are compounds consisting of oxygen atoms bound to transition metals (Cr_2O_3, CuO_2, TiO_2, ZrO_2, etc). Their distinctive magnetic, optical, and electrochemical behaviors make them suitable for a variety of applications, including catalysis and energy storage [73].

Among these oxides, chromium oxides with the general chemical formula of Cr_xO_y, belonging to the family of transition metal oxides, have attracted much interest in the past decade due to their unique properties and wide range of applications. Chromium (Cr) is known to exist in different valence states (+1, +2, +3, +4, and +6) and form various oxides like CrO, CrO_2, CrO_3, Cr_2O, Cr_2O_3, Cr_3O, Cr_3O_4, Cr_3O_8, Cr_5O_{12}, and Cr_8O_{21} [74,75]. There are a large number of oxide phases of chromium such as Cr_2O, CrO, CrO_2, Cr_2O_3, Cr_3O_4, Cr_8O_{11}. Thermodynamically, the most stable in this list is rhombohedral α-Cr_2O_3 with the mineral name eskolaite (hexagonal cell parameters: a = 4.9570 Å, c = 13.5923 Å, Figure 2) [76].

Eskolaite is a technologically important material owing to the convergence of a variety of mechanical, physical, and chemical properties that offer interesting opportunities for both fundamental research and technological applications.

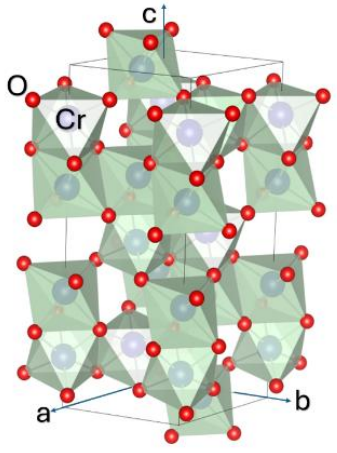

Figure 2. Unit cell model of rhombohedral α-Cr_2O_3 (made by the VESTA program [77]).

Eskolaite is one of the hardest transition metal oxides, showing hardness values from 25 to 44.7 GPa [1–3]. It has low friction coefficient and high wear resistance [1,15], high melting point (~2435 °C [74]), corrosion resistance [78], exciting magneto-electric [6], ferromagnetic, antiferromagnetic, flexomagnetic [8], and catalytic properties [79]. α-Cr_2O_3 offers interesting magnetoelectric properties in its various forms. Intrinsically, Cr_2O_3 exhibits antiferromagnetic characteristics, where Cr^{3+} ion moments are aligned antiferromagnetically with their spins parallel to the rhombohedral c axis below the Neél temperature of ca. 307 K [80,81]. However, this antiferromagnetic character in α-Cr_2O_3 can also be tuned

to weak ferromagnetism [82] and even superparamagnetic, where a better degree of control in size and magnetic anisotropy distribution can be effectively achieved [83,84]. Besides tunable magnetic behaviour, Cr_2O_3 also showed efficient electric transport properties. Despite its intrinsic insulating nature, Cr_2O_3 is considered as a good *p*-type conducting oxide with a bandgap of ~3 eV, showing that its conductivity values can be tuned to $1 \cdot 10^{-2}$ to $2.5 \cdot 10^{-3}$ S cm^{-1} based on growth conditions [5]. These properties have made this transition metal oxide a good candidate for protective coatings in tribological applications [12,85], gas sensors [11], solar energy absorbers [86], corrosion-resistant applications in magnetoelectric random access memories and THz spintronic devices [9,10]. Chromium oxide coatings have been developed for the protection of the tape-bearing surface of the digital compact cassette (DCC) [15]. Considering the wide range of applicability, different techniques have been used for the development of Cr_2O_3 thin films (Figure 1).

2.2.1. Mechanical properties of chromium oxide films

The previous reports demonstrate that the Cr_2O_3 thin films possess a high hardness and moduli [20,85,87–90], as can be observed in Table 1, however, variations in microstructure, film density/porosity, and composition, chromium oxide coatings can lead to different values. For instance, Mohammadtaheri *et al.* reported a hardness of ~29.7 GPa for Cr_2O_3 coatings deposited by reactive magnetron sputtering, attributed to dense microstructure and stoichiometric single-phase of Cr_2O_3 coatings [1]. In contrast, obtained hardness values of ~36 GPa for chromium oxide film; however, for the films that unreacted Cr existed, relying on the XRD results, decrease in hardness values were observed. Because the hardness of Cr metal is obviously lower than that of the α-Cr_2O_3 phase, the unreacted Cr leads to the lower hardness of the films [2].

Similarly, *Huang et al.* demonstrated high hardness of 44.7 GPa, due to improved crystallinity and formation of *α*-Cr_2O_3 [3]. The importance of the Cr_2O_3 stoichiometry was even more pronounced in the case of oxygen-deficient (Cr-rich) films exhibited reduced hardness of ~16–18 GPa due to higher defect density and porosity [15,87]. Seems that the most common range of hardness of relatively thick (from several hundred nanometers to micrometer) film containing eskolaite phase remains approximately at 30 GPa. Besides the films with thickness values in the range of several micrometers, the atomic layer deposited chromium oxide coatings with thickness values of 147 nm showed hardness of ~22.5 GPa and modulus of ~200 GPa [66], and the 80 nm films in another report showed the hardness value of 19 GPa [89]. Overall, the highest mechanical performance of chromium oxide is associated with dense, highly crystalline, near-stoichiometric α-Cr_2O_3, while lower values arise from poor crystallinity, sub-stoichiometric composition, or insufficient energy during deposition, as discussed above. Tribological test results exhibited that Cr_2O_3 coated substrates possessed better wear resistance under sliding wear test conditions, which can be related to the high hardness of the surface, and low coefficient of friction [15,87].

Table. 1 Different hardness and moduli values of chromium oxide films reported previously. The full names of the methods are shown as presented in the original publication.

The growth method of films	Thickness	H (GPa)	E (GPa)	Ref.
reactive magnetron sputtering	1.5 μm	29.7	304.9	[1]
arc ion plating	–	36	300	[2]
vacuum cathodic arc	1.4 μm	44.7	285	[3]
rf-sputtering	200 μm	29.5	209	[15]
ALD	147 nm	22.5	200	[66]
RF reactive magnetron sputtering	1.8 μm	21	234	[85]
reactively sputtering	100 nm	25	–	[87]
post-annealing of Cr	80 nm	19	175	[89]

2.2.2. Optical properties of chromium oxide films

Chromium (III) oxide (Cr_2O_3, eskolaite) thin films show a broad but consistent set of optical fingerprints in the UV–visible range, yet the reported numerical values of absorption band position vary substantially because the optical response depends strongly on growth route, crystallinity, defect chemistry, and post-deposition treatment. The following five bands are the most pronouncing and know: at 600 nm (~2.1 eV), 460 nm (~2.7 eV), 355 nm (~3.5 eV), and around 250 nm (~5.0 eV) [91], while Karlsson similarly reported absorption around ~2.1 eV and ~2.7 eV with an additional weaker feature near ~3.4 eV [92]. In stoichiometric Cr_2O_3, the prominent visible absorption bands around ~2.2 eV and ~3.0 eV are commonly attributed to Cr^{+3} ligand-field (d–d) transitions [93]. Reported optical band gaps (*Eg*) for Cr_2O_3 films cluster in the 3eV range, but the literature contains both direct and indirect interpretations of the absorption edge depending on the film composition and the structural state. For materials treated as direct-gap semiconductors, hydrothermally synthesized Cr_2O_3 showed a direct band gap of ~3.2 eV obtained using a Tauc analysis [94]. In another study focusing on annealing effects, the direct gap was reported as ~3.18–3.26 eV before annealing and increased to ~3.32–3.38 eV after annealing at 500 °C, consistent with structural ordering, grain size increase, and defect reduction during heat treatment [95]. In contrast, several works interpret the absorption edge as indirect, especially for amorphous or partially crystallized films. For example, chromium oxide film deposited using the CVD technique displayed an indirect gap of ~2.95 eV for amorphous films annealed at 400 °C and ~3.2 eV for crystalline films annealed at 500 °C [96]. Similarly, evaporated Cr films oxidized to an amorphous oxide by annealing in air at 570 K were reported with an indirect gap of ~3.3 eV. The refractive index in the UV–Vis region was reported to fall in the range ~1.3–2.1, with visible-region values of ~1.6–1.9 before annealing and ~2.2–2.4 after annealing, again suggesting that heat treatment increases optical density/ordering or reduces porosity and hydroxyl content [56]. For CVD films grown from chromium acetylacetonate, an indirect transition with 3.0–3.1 eV was reported, together with an additional absorption band near ~2.75 eV that is not

itself a band gap but a distinct optical feature [5]. For radio-frequency sputtered chromia prepared at different oxygen partial pressures, spectroscopic ellipsometry yielded a notably higher refractive index at 633 nm of ~2.20–2.76, together with a direct optical gap of ~3.7 eV [97]. Taken together, these reports indicate that "the Cr_2O_3 band gap" is best treated as a processing-dependent optical edge that can appear direct-like or indirect-like depending on film disorder, defect states, and the analysis modelling.

2.3. Methods to improve properties of chromium oxide films

2.3.1. Role of deposition parameters

Finding the appropriate deposition parameters is one of the keys to developing films with desired properties. Different deposition process parameters, for instance deposition temperature (T_G), process pressure, and oxygen flow rate, strongly influence the structure, adhesion, and other properties of the chromium oxide films [88,97,98]. For instance, Hones *et al.* showed that Polycrystalline films with a single α-Cr_2O_3 phase were obtained in the range between 15 and 25% oxygen in the sputtering gas at a T_G value exceeding ~227 °C, exhibiting hardness values exceeding 30 GPa, with high adhesion. In addition to mechanical performance, the optical response of sputtered chromium oxide (e.g., refractive index and absorption edge behavior) has also shown variability with deposition conditions, reflecting changes in stoichiometry, crystallinity, and defect content [97]. Similar conclusions were emphasized by Mohammadtaheri *et al.,* showing that a dense stoichiometric Cr_2O_3 structure is responsible for the hard chromium oxide coating, and depositing hard Cr_2O_3 coatings is a highly critical task, requiring optimization of deposition parameters [99]. For atomic layer deposition (ALD), process optimization extends beyond T_G to include the choice of metal precursor and co-reactant as well as the pulse and purge durations, because these parameters govern surface saturation, impurity incorporation, growth rate, and ultimately film structure and adhesion [27,67]. For instance, Tarre *et al.* demonstrated that stoichiometric Cr_2O_3 films with a low impurity level can be grown from CrO_2Cl_2 and CH_3OH in the self-limited ALD mode at T_G up to 420 °C. At higher T_G, decomposition of CrO_2Cl_2 caused marked deviations from the self-limited growth, and at lower T_G (<330 °C), the precursors were insufficiently reactive for achieving an acceptable growth rate. Together, these examples illustrate that the final properties of chromium oxide films are tightly coupled to the process window, and the desired performance requires controlling of deposition parameters rather than relying on nominal chemistry alone.

2.3.2. Post-deposition thermal treatment

Post-deposition thermal treatment (annealing) is widely reported as an effective strategy for tailoring the structure-property relationships of chromium oxide thin films. In general, the literature indicates that amorphous Cr-O films tend to exhibit

lower hardness and elastic modulus, whereas films that become crystalline after appropriate heat treatment often show improved mechanical performance. For instance, it was found that the amorphous chromium oxide film deposited at 150 °C in pure argon has a hardness of 21 GPa, increased to 25 GPa upon crystallization by annealing at 300 °C [87]. Because annealing simultaneously modifies multiple microstructural factors such as crystallinity, defect density, residual stress state, and grain size, both annealing temperature and duration must be carefully controlled. In particular, although crystallization can strengthen the film, annealing may also reduce hardness if it promotes stress relaxation and significant grain growth, since elevated temperatures increase diffusion and grain-boundary mobility. These competing effects have been discussed in several studies [87,88,99]. For instance, the hardness of Cr_2O_3 films decreased from 25 GPa to 16 GPa by increasing annealing temperature from 300 to 700 °C. Annealing also strongly affects the optical and functional (e.g., sensing) properties of chromium oxide films. For optical behavior, it has been reported that the as-deposited films can exhibit very low transmittance, which may improve after annealing due to changes in phase composition, defect states, and film densification [100]. An increase in the annealing temperature of Cr_2O_3 from 350 to 450 °C has initiated the increase of grains from a diameter of 30 to 130 nm, accompanied with the electrical resistance of the film. Importantly, annealing can also be used to tune surface reactivity and thus gas-sensing selectivity, because adsorption sites, grain boundaries, and defect chemistry change with thermal history. For example, the highest response to NH_3 was reported for Cr_2O_3 films annealed at 450 °C, whereas films annealed at 400 °C showed stronger response to toluene vapors, and films annealed at 350 °C exhibited better sensitivity to NO_2 and acetone vapors [101]. These results highlight annealing as a powerful but not universally beneficial post-treatment: it can enhance crystallinity and optical transparency, yet may also reduce hardness through stress relaxation and coarsening, making optimization of annealing conditions essential for any targeted Cr_2O_3 thin film application.

2.3.3. Doping and formation of ternary compound films

Converting the binary Cr-O type of Cr_2O_3 to ternary Cr-Me-O type of compound could offer new opportunities for tailoring the properties of this material. For example, formation of ternary films of Cr-Zr-O type has resulted in increasing its hardness up to 40 GPa (ranking to a superhard type of film) by preserving this value at high temperatures up to 500 °C [20]. In addition to mechanical durability improvement, doping with different elements was a successful method to provide different n-type or p-type conductivity, an increase in transmittance in visible light, and changing of optical band gap behavior [16,102–105]. For instance, decrease in direct optical band gap energy from 2.92 eV to 2.6 eV was observed with an increase in Cu content. UV–Vis absorption and Tauc's plot showed a red shift in the optical bandgap of pristine Cr_2O_3 from 2.85 eV to 2.75 eV when it is doped with Ni [103]. A ternary Cr-Al-O film deposited by the cathodic arc method displayed high absorptance of 0.924, thermal stability, and solar selectivity

performance, making the film a promising candidate for high-temperature photothermal conversion [105]. The list of ternary chromium oxide films using different elements, by different deposition techniques, has been collected in Table 2, including a list of properties that these films displayed.

Table 2. List of published ternary component oxide films containing Cr.

Ternary composition	Deposition technique	Structure and properties	Ref.
Cr-Zr-O	RF sputtering	H ≥ 40 GPa, stable up to 500 °C.	[20]
Cr-Al-O	cathodic arc ion plating	high absorptance solar selectivity of 0.919/0.225.	[105]
Cu doped Cr_2O_3	sol-gel	reduction of direct E_g from 2.94 to 2.51 eV.	[18]
Ti-Cr-O	sputtering	H = 30.9 ± 4.9 GPa, corrosion-resistant.	[21]
Cu_xCrO_2	spray pyrolysis	*p*-type transparent conducting.	[106]
TiO_2:Cr	chemical bath deposition	direct transition E_g decrease from 3.26 to 3.14 eV. electrical conductivity.	[107]
Cr_2O_3–TiO_2	flame spraying	H= 9.1 GPa, wear resistant improvement.	[108]
Cr_2O_3-25%TiO_2	plasma spray	H = ~9.2 GPa.	[109]
Ti-doped Cr_2O_3	PLD	weak ferromagnetism at RT.	[110]
Ni-Doped Cr_2O_3	sol-gel	90% of transmittance in visible light, direct transition E_g = 2.71 to 2.85 eV .	[111]
Cr-doped SnO_2	spray pyrolysis	*n*-type conductivity direct transition E_g 3.49–3.68eV.	[102]
Cr-doped TiO_2	D.C. sputtering	indirect transition E_g decrease to 2.91 eV (3.27 eV for TiO_2).	[104]
$(Al_{1-x}Cr_x)_2O_3$	cathodic arc evaporation	H = ~11 to 23 GPa, E = 190 to 375 GPa.	[112]
$(Cr,Al)_2O_3$	DC sputtering	H = 24–27 GPa , E = 190–230 GPa.	[113]
Cr_2O_3–Al_2O_3 composite	atmospheric plasma spraying	improving wear-resistance compared with Cr_2O_3.	[114]
Al_2O_3:Cr_2O_3	RF sputtering	sensitivity to ammonia gas at room temperature.	[115]
Ni^{2+}-doped Cr_2O_3	co-precipitation	direct transition E_g from 2.85 (Cr_2O_3) to 2.75 eV.	[103]
Cr-O-N	cathodic arc evaporation	H = 19 to 30 GPa and wear resistant.	[116]
Cr-V-O	RF sputtering	H = 38 GPa for corundum structured film.	[117]
Al-Cr-O	cathodic arc evaporation	hydrogen permeation barrier properties.	[118]
$(Al_xCr_{1-x})_{2+y}O_{3-y}$	cathodic arc evaporation	H = 26–30 GPa.	[119], [120]
Mg-doped *α*-Cr_2O_3	polymer precursor method	chromo-resistive controlled by Cr^{6+}/Cr^{3+} ratio.	[121]

2.4. ALD of chromium oxide films, used precursors, and properties

ALD technique has been considered for deposition of chromium oxide films for mostly as hard [66], high-temperature stable [II][1], corrosion-protective [122] and semiconductor films [123] in various microelectronics, micro electromechanical (MEMS) or nanoelectromechanical (NEMS) systems and advanced tooling applications [27,67,122]. A list of used Cr precursors in combination with an oxygen source, T_G, structural and properties of the films has been listed in Table 3.

Table 3. List of the previously published chromium oxide ALD precursors.

Cr precursor	Oxidant	T_G	Film characteristics	Ref.
$Cr(acac)_3$	O_3	300 °C	affective barrier protection against alkaline and chloride	[122]
$Cr(acac)_3$	O_3	300 °C	Excessive O_3 exposure reveals a linear etching mechanism.	[67]
CrO_2Cl_2	CH_3OH	330–420 °C	CrO_2Cl_2 decomposition at T_G>420°C.	[27]
CrO_2Cl_2	CH_3OH	420 °C	H=22.5 GPa, E = 200 GPa	[66]
CrO_2Cl_2	CH_3OH	375 °C	chemical stable.	[124,125]
CrO_2Cl_2	H_2O	~100–180 °C	chromium oxide bottom layer enhanced metal–substrate adhesion.	[126]
$Cr(acac)_3$	O_3	240–270 °C	p-type semiconducting $CuCrO_2$ films E_g=3.09 eV.	[123]
$Cr(thd)_3$	O_3	225, 275 °C	α-Cr_2O_3 seed layer for α-Al_2O_3 growth.	[28]

Various inorganic and organometallic metal precursors together with ozone, water and hydrogen peroxide have previously been used to synthesize Cr_2O_3 by ALD. Some of these precursors like CrO_2Cl_2, being one of the often-used precursors for chromia, is toxic, since hexavalent chromium similar with other toxic heavy metals has the ability of contamination and issue in marine environment, considering the toxic effects on animal health and other organisms in the aquatic environment [127–129]. Considering this, it is preferred to replace precursors with 3+ oxidation state of Cr to have more environmentally friendly deposition process. Additionally, previous studies have reporting problems relating to chlorine contamination when CrO_2Cl_2 with CH_3OH or H_2O have been used to growth Cr_2O_3 by ALD [27,130]. Thus, chromium acetylacetonate ($Cr(acac)_3$) and tris (2,2,6,6 tetramethyl heptane 3,5 dione) chromium (III) ($Cr(thd)_3$) can be considered as alternatives to overcome these problems. The growth of chromium oxide films with eskolaite structure using ($Cr(acac)_3$) and O_3 has been reported previously at T_G of 300 °C, resulting in films with Cr^{+3} oxidation state according

[1] In the following the references denoted with Rome numbers refer to the original publications of this thesis listed in chapter "ORIGINAL PUBLICATIONS and AUTHOR CONCRIBUTION"

to the XPS analysis with no measurable carbon impurity [67], while the ALD of the 9–20 nm thick Cr_2O_3 film as seed layer for deposition of α-Al_2O_3, was reported at substrate temperature of 225 °C from $Cr(thd)_3$ and O_3.

2.5. Reported ALD ternary Cr-Me-O films by today

The number of studies on ternary chromium oxide containing films grown by ALD is limited. Table 4 summarizes previously used precursors in the ALD of these ternary film compositions and the structural and characteristic changes in the films. However, as discussed in Section 2.3.3, doping and formation of the different heterostructures can be the way for tailoring the mechanical, optical and electrical properties of chromia, thereby expanding its application possibilities. Therefore, given the precise control over thickness and composition that ALD offers for ternary thin films, more studies are needed. For instance, $CrCuO_2$ films grown by ALD using ($Cu(thd)_2$) and ($Cr(acac)_3$) as the metal precursors, with ozone as oxygen source, showed p-type semiconducting behavior with direct bandgap value of 3.09 eV and visible light transmittance above 75% [123]. This performance is slightly higher than transmittance range of 32–75% for $CuCrO_2$ films fabricated by sol–gel technique [131,132].

Table 4. Summary of published studies on ternary oxide films containing Cr.

Film	Precursors used	T_G (°C)	Structure	Ref.
$CuCrO_2$	[($Cr(acac)_3$-O_3]+ [($Cu(thd)_2$-O_3]	240–270	• amorphous	[123]
TiO_2–Cr_2O_3 nanolaminate	[$TiCl_4$-CH_3OH]+ [CrO_2Cl_2-CH_3OH]	375	• rutile phase on sapphire • anatase on Si	[124]
Cr–Ti–O	[$TiCl_4$-CH_3OH]+ [CrO_2Cl_2-CH_3OH]	420	• α-Cr_2O_3	[125]
$(Cr,Al)_2O_3$	[$Cr(thd)_3$-O_3] +[TMA-O_3]	275	• X-ray amorphous	[I], [V]
$(Cr,Ti)_2O_3$	[CrO_2Cl_2-CH_3OH] +[$TiCl_4$-H_2O]	275	• α-Cr_2O_3	[IV]

2.6. ALD of TiO_2, Al_2O_3, HfO_2, their prospective properties and applications

Films of titanium dioxide (TiO_2), aluminum oxide (Al_2O_3), and hafnium oxide (HfO_2) are among the most extensively studied oxides for deposition by atomic layer deposition (ALD). Their properties have been described previously in a review made by Ponraj *et al.* [133]. Therefore, in this work, only the list of the most important properties of those oxides is included.

Aluminum oxide (Al_2O_3) is a widely used ceramic material known for its excellent wear resistance, high mechanical hardness, broad optical transparency,

and strong diffusion-barrier performance. The most often observed polymorphs of crystalline Al_2O_3 are α-Al_2O_3 (corundum, a = 4.757 Å, c = 12.987 Å, PDF Card No. 71-3646), γ-Al_2O_3 (a = 7.9 Å, PDF Card No.10-0425), and η-Al_2O_3 (a = 7.914 Å, PDF Card No. 79-1557). The 3D models of unit cells of these crystal structures are shown in Figure 3. With its wide band gap and reliability as an insulating oxide, Al_2O_3 has been used as a high-permittivity (high-k) component in metal-oxide–semiconductor (MOS) gate stacks [134]. These characteristics make Al_2O_3 suitable for protective and barrier layers, microelectronic device architectures, energy-storage systems, and optical components [134–136].

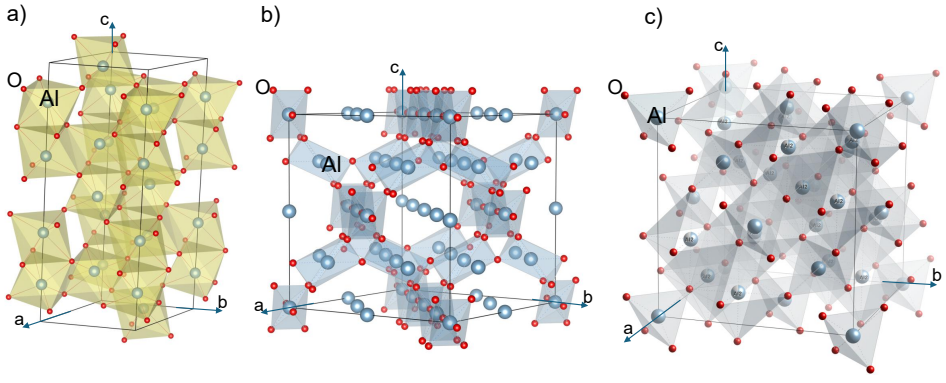

Figure 3. Unit cell models of the (a) rhombohedral α-Al_2O_3 (PDF Card No. 71-3646), (b) cubic γ-Al_2O_3 (PDF Card No.10-0425), and (c) cubic η-Al_2O_3 (PDF Card No. 79-1557) phases.

Titanium dioxide (TiO_2) is similarly recognized as a high-k dielectric and stands out as one of the most promising photocatalytic materials. Its chemical stability and effective barrier properties, combined with strong photocatalytic activity, make TiO_2 highly attractive for environmental remediation, pollutant degradation, and solar-energy applications. Two mostly observed crystalline phases for titanium dioxide are anatase (a = 3.77 Å, c = 9.42 Å, PDF Card No. 01-075-2552) and rutile (a = 4.593 Å, c = 2.959 Å, PDF Card No. 21-1276), as illustrated by the models of unit cells in Figure 4. TiO_2 plays an important role in photovoltaic technologies and water-splitting devices, and it is widely investigated for self-cleaning surfaces, biomedical sensing, and optical coatings [137–139].

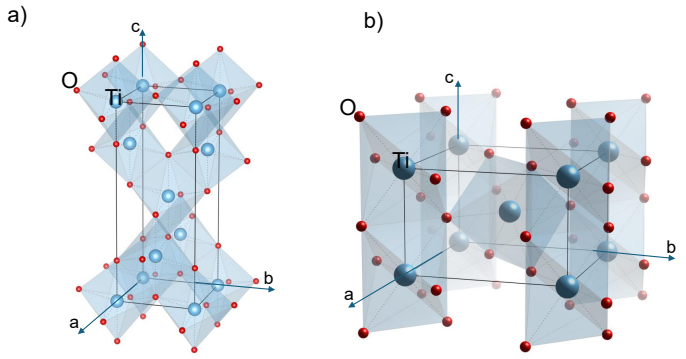

Figure 4. Unit cell models of tetragonal crystal structures of a) anatase (PDF Card No. 01-075-2552), b) rutile phases of TiO_2 (PDF Card No. 21-1276).

Hafnium oxide (HfO_2) is distinguished by its high dielectric constant ($k \approx 25$), wide band gap ($E_g \approx 5.7$ eV), excellent thermal and mechanical stability, low leakage current, high breakdown field (3.9–6.7 MV/cm), and broad optical transparency spanning from the ultraviolet (UV) to the infrared (IR) region. These properties have driven significant interest in HfO_2 for use as a high-k dielectric in advanced electronic devices and as a low-loss optical material in UV optics. HfO_2 is widely applied in electronics and optoelectronics, for example MEMS, where it serves as a high-permittivity insulating layer that reduces electro-resonator gaps and enhances capacitive electromechanical coupling [140–143]. The most commonly observed crystalline phases of hafnium dioxide are monoclinic ($a = 5.25$ Å, $b = 5.18$ Å, $c = 5.12$ Å; PDF Card No. 6-0318) tetragonal ($a = 3.5775$ Å, $c = 5.1996$ Å; PDF Card No. 01-078-5756), and cubic ($a = c = 5.0950$ Å; PDF Card No. 53-0560) structures, as illustrated by the 3D unit cell models shown in Figure 5.

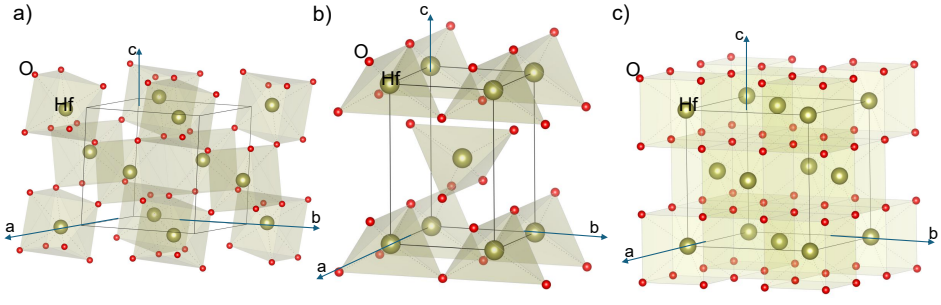

Figure 5. Unit cell models of a) monoclinic (PDF Card No. 6-0318), b) tetragonal (PDF Card No. 01-078-5756), and c) cubic (PDF Card No. 53-0560) phases of HfO_2.

3. RESEARCH GAP IN ALD OF TERNARY CR-ME-O FILMS

As mentioned in chapter 2, chromium (III) oxide (α-Cr_2O_3, eskolaite) is an industrially crucial material, especially in the field of microelectronics, but it is limited in real-world use. Fabrication of ternary Cr-Me-O thin film materials would be one possibility to solve existing issues. However, the field lacks a systematic studies investigating ALD from binary Cr_2O_3 to ternary Cr-Me-O thin film materials with improved and tailorable chemical composition, structural, mechanical and optical properties. The number of published studies on ultra-thin ternary chromium-containing oxides grown by ALD remains small, especially when taking into account the need to move away from chromium (VI) based chemistries toward chromium (III) precursors.

This thesis addresses these gaps by establishing a materials engineering framework for ternary chromium oxides through doping and mixing strategies to tailor film properties, using designed supercycles for composition control and examining composition–structure–property relationships in the films. By engineering $(Cr, Me)_2O_3$ type compositions, ultra-thin chromia films can be used at higher temperatures together with higher wear resistance and a tunable optical band gap, not achievable in binary Cr_2O_3 thin films.

4. RESEARCH OBJECTIVES

The first goal of this research was to understand how the mechanical, tribological, optical properties, and thermal stability of the Cr_2O_3 thin films, synthesized by a novel precursor combination, (tris (2,2,6,6 tetramethyl heptane 3,5 dione) chromium (III) ($Cr(thd)_3$)) and ozone O_3, depend on process parameters of ALD.

Secondly, to investigate whether it is possible to tune the mechanical and optical properties and increase the thermal stability of the chromium oxide by doping and mixing it with TiO_2, Al_2O_3, and HfO_2.

Finally, the effect of the substrates, including single crystals of Si (100), α-Al_2O_3 (001), α-Al_2O_3 (012), and amorphous SiO_2, on the film structure and properties was investigated.

The research aimed to create a comprehensive study about the engineering and architecture of binary and ternary chromium-containing oxide films to introduce more mechanically and thermally durable coatings with adjustable optical performance, considering the benefits of sustainability and economic efficiency by extending the service life of applications.

5. METHODS

5.1. Atomic Layer Deposition

Atomic layer deposition (ALD) has emerged as a crucial thin film deposition technique for applications in nanoelectronics, catalysis, and other fields, owing to its high conformality on 3D nanostructured substrates and its precise, atomic level control over the film thickness [23]. The method is based on self-limiting gas solid reaction between two or more gaseous precursors and a solid substrate [25]. Deposition of the thin film takes place layer by layer it means vapors of precursor chemical are introduced sequentially with the purge steps between to remove excess reactants and by-products. The experimental parameters such as T_G, reactant pressures, their exposure duration, and the lengths of the purging time are adjusted to ensure self-limiting surface reactions, leaving only chemisorbed species on the surface. Under these conditions, the film growth is self-limiting, ensuring that uniform films with excellent conformality can be deposited even onto complex-shaped large area substrates, and film thicknesses can be accurately controlled simply by controlling the number of reaction cycles [133].

In applications like catalysis, energy storage, and photovoltaics, there is increasing interest in more complex materials such as doped, ternary, and quaternary materials. Because ALD controls growth at the atomic level, it enables the fabrication of homogeneous multicomponent and multilayer thin films by depositing atomic layers of different materials in a controlled sequence [23].

The most common approach for the synthesis of a doped or ternary material by ALD is to alternate between several cycles of two binary ALD processes in a so-called supercycle. By performing k cycles of binary process AC_x and l cycles of binary process BC_y, a ternary AB_wC_z film can be deposited, where C is a non-metal atom (e.g., O, N). This approach allows for the tuning of the composition by choosing a certain cycle ratio of $k/(k + l)$.

A key challenge of the supercycle approach in ALD is that the individual binary processes typically must share overlapping temperature windows. Otherwise, decomposition or insufficient reactivity leads to non-ideal growth. Advances in reactor designs with rapid thermal control may enable different temperatures for individual cycles. However, homogeneous mixing of the deposited materials is not guaranteed [23]. The dopant atoms may be spaced too far apart in the direction normal to the film surface, or one cycle of the dopant ALD process may result in too high a density of dopant atoms in a given lateral plane. To overcome these issues, the selection of a small enough bilayer period is essential to ensure optimal dopant distribution throughout the film [23].

Alternative approaches to the synthesis of ternary films are to co-inject the precursors by pulsing the two precursor vapor streams into the reaction chamber together. Even two precursors can be dissolved in a specific ratio in a solvent and then injected. This results in an adsorbed monolayer containing two different precursor molecules, which is converted into a mixed multicomponent film by exposure to the co-reactant. The primary limitation of this approach is growth

governed by competitive precursor adsorption, where the ability of ALD in conformality coating and compositional uniformity is potentially lost if the partial pressures of the precursor gases are not perfectly homogeneous in complex architectures like trenches [23].

5.2. X-ray fluorescence

X-ray fluorescence spectrometry (XRF) is a rapid, non-destructive technique for qualitative and quantitative elemental analysis from B to U, with sensitivity in the range of 10^{-8} g. The truly multi-elemental character, acceptable speed and economy, ease of automation, portability, and the possibility to directly analyse solid samples without prior acid digestion. For ultra-thin films (thickness ≤50 nm), XRF is particularly valuable because techniques such as EDS and SIMS often contain a substantial signal contribution from the substrate, which is difficult to exclude reliably. In XRF, the sample is irradiated with an intense incident X-ray beam. Some of the energy is scattered, but some is absorbed within the sample, leading to inner ionization, ejecting electrons from the lower energy levels (usually K and L), making the electronic structure of the atom unstable. The resulting vacancy is filled by an electron falling from a higher energy level, releasing the energy difference of the two orbitals involved as a photon. Because these photon energies are characteristic of each element, the emitted spectrum identifies the elements present. The term -fluorescence- is applied to phenomena in which the absorption of radiation at a specific energy results in the re-emission of radiation of a different energy. The intensity of the energy measured by detectors is proportional to the abundance of the element in the sample [144].

5.3. X-ray diffraction and X-ray reflectometry

Knowing of structural properties of a material is essential because the atomic structure is in tight correlating with the physical and chemical properties of the material. X-ray diffractometry (XRD) is a standard method to determine structure-related parameters (phase composition, crystal structure, lattice parameters, size, shape and preferential orientation of crystallites, internal stresses, and film thickness). In crystalline materials, coherent (elastic/Rayleigh) scattering from periodically spaced atomic planes interferes constructively at specific diffraction angles (2θ), producing the diffraction pattern used for structure determination. The condition for constructive interference is given by Bragg's law, $2dsin(\theta)=\lambda$, which relates the interplanar spacing (d) to the wavelength (λ) and the Bragg diffraction angle (θ) [145]. In laboratory instruments, Cu $K\alpha_1$ ($\lambda_{K\alpha 1}$ = 0.154059 nm, X-rays are monochromatized) or Cu $K\alpha$ radiation ($\lambda_{K\alpha}$ = 0.15418 nm, a combination of Cu $K\alpha_1$ and Cu $K\alpha_2$ radiations, X-rays are not monochromatized) is commonly used [146]. Because X-ray interaction with atoms is relatively weak, the penetration depth of X-rays in the material, which depends on X-ray energy,

the sample's absorption, and the incidence angle (α) of X-rays with respect to the sample surface, can reach several tens of micrometers. Therefore, when studying structure parameters of thin films and surfaces, a grazing-incidence X-ray diffraction (GIXRD) technique is often used that suppresses bulk contribution and enhances the weak surface diffraction signal [146,147].

X-ray reflectivity (XRR) is a non-destructive technique used to characterize thin films. The strength of the XRR technique resides in the use of an X-ray beam with a very low angle of incidence ω (from near zero to ~2–3), making the method very sensitive to surface features due to the low penetration of the X-ray beam. Since it is independent of crystallinity, XRR can be applied to both crystalline and amorphous materials. The technique provides accurate information on film thickness, density, surface roughness, and interface roughness, making it a powerful tool for thin-film characterization [147].

5.3.1. Grazing incidence X-ray diffraction

The GIXRD technique is suitable for studying phase composition, crystal structure, lattice parameters, crystallite size, and preferred crystallite growth orientation of the thin films. In GIXRD, the angle α ranges from 0.1 to 1° The low incidence angle produces signals with higher intensity from the top layers of the sample as the beam length of the rays increases within these layers, which, in turn, increases the volume of the irradiated material. From GIXRD patterns recorded at different values of α, it is possible to obtain structural information at different depths of the sample [147–149].

Anisotropic distribution of grain orientations in a material is referred as preferred orientation or texture. The texture status can be quantitatively characterized by the texture coefficient calculated using the intensities of XRD reflections as:

$$TC(hkl) = \frac{\frac{\mathrm{I(hkl)}}{\mathrm{I_0(hkl)}}}{\frac{1}{\mathrm{N}}\sum\left(\frac{\mathrm{I(hkl)}}{\mathrm{I_0(hkl)}}\right)} \quad (1)$$

where *I (hkl)* is the observed relative intensity, integrated over the whole area of a *hkl* reflection and I_0 *(hkl)* is the relative intensity of the same reflection either calculated for an ideal powder sample with structure parameters from the database ICSD or taken from the corresponding data-card from PDF-2 database, *N* is the number of observed reflections and the sum is calculated over all observed reflections [150].

Once positions, heights and areas of reflections are determined, an estimation of the crystallite size can be calculated using Scherrer's formula, $<D>_v = \lambda / (\beta \cos \theta)$, where λ is the wavelength of the X-rays, β is the physical integral width of a diffraction reflection corrected by broadening of the instrumental peak (based on standard reference material LaB_6, SRM-660) and θ is the Bragg angle of the reflection [151]. To obtain the intrinsic peak

broadening, β was corrected for instrumental broadening using the relation $\beta^2 = \beta_{exp}^2 - \beta_{inst}^2$ [152].

5.3.2. High-resolution X-ray diffraction (HRXRD) and analysis of sample mosaicity

The aim of high-resolution X-ray diffraction is to resolve as well as possible the diffraction peaks that are closely spaced diffraction pattern. This is achieved by reducing the angular divergence of the primary beam, the acceptance of the detector and monochromatizating of X-rays. Typically, a monochromator is employed to condition the incident beam, producing a highly collimated and nearly parallel, free from Cu K_β and almost free from characteristic Cu $K\alpha_2$ component X-ray beam. For example, a two-bounce Ge (220) monochromator of SmartLab can reduce the instrumental resolution of the diffraction pattern to approximately 0.009°, while four-bounce Ge (440) monochromator of SmartLab increases the resolution down to 0.0015°[1].

The ω-scan (rocking scan) in a $2\theta/\omega$ geometry is commonly used to assess material quality, including defect density, film orientation, and epitaxial quality. This measurement is performed by fixing the detector at or near a Bragg reflection and rotating the sample around the ω-axis, or by synchronous and equidirectional rotation of the detector and X-ray tube arms around a stationary sample. Because the scan probes the crystallographic direction normal to the atomic planes, it is sensitive to variations in the orientation of these planes and to deviations from ideal crystal alignment. In highly oriented single-crystal materials, the intensity decreases rapidly as ω is varied away from the Bragg condition, resulting in a sharp peak. In contrast, powder samples or materials with random grain orientation exhibit diffraction intensity over a wider ω scan range, since a large number of crystallites will satisfy the Bragg condition at almost any sample orientation. The full width at half maximum of the rocking curve ($FWHM_\omega$) serves as an indicator of crystal alignment and epitaxial quality. The smaller $FWHM_\omega$ values correspond to stronger film orientation and high epitaxial quality, whereas larger values indicate a broader distribution of crystallographic orientations [147].

The in-plane measurement in X-ray diffraction is used to determine the crystallographic orientation of a thin film parallel to the sample surface, i.e. how the crystal lattice is aligned laterally with respect to the substrate, rather than along the surface normal. While conventional $2\theta/\omega$ scans mainly provide information about the out-of-plane (growth direction) texture, in-plane orientation requires probing lattice planes that are tilted with respect to the surface normal, which is commonly achieved using an azimuthal phi (ϕ) scan. In this method, the diffractometer is first positioned at fixed 2θ and ω angles corresponding to a specific off-axis reflection, and then the sample is rotated around its surface normal over 360° while recording the diffracted intensity. The resulting ϕ scan reveals the rotational

[1] X-ray diffraction analysis of thin films. Training Textbook. Rigaku 2009, 176 page.

symmetry of crystallographic planes within the film plane: discrete peaks indicate a well-defined epitaxial in-plane alignment, while a continuous or broad intensity distribution suggests random in-plane orientation or fiber texture. By comparing the angular positions of the film and substrate peaks in the ϕ scan, the relative in-plane epitaxial relationship between film and substrate can be directly determined [147].

5.3.3. X-ray reflectivity (XRR)

The XRR technique resides in the use of an X-ray beam with a very low angle of incidence α. The XRR measurement is performed by using $\theta/2\theta$ scan at angles from near zero to 4 to 10° in 2θ (Figure 6), depending on the structure complexity. The parameters calculated by fitting the observed XRR pattern are the following: root-mean roughness (σ), thickness (t) and density 1(ρ) of the sample surface and/or every layer in the laminate-type thin films material. The typical t range that XRR can determine is from ~2 nm to ~300 nm (depending on the surface roughness and density gradients in the material) and σ can be determined in the range from 0.5 to 6 nm. The density of the sample surface, consisting just from a single element, can be calculated from α_c, as $\rho = K(\alpha_c)^2$, where $K=\pi A/(r_e\lambda^2 N_A Z)$, r_e is the classical electron radius, A is the atomic (molar) mass, Z is the atomic number, and N_A is Avogadro's number [147,148,153].

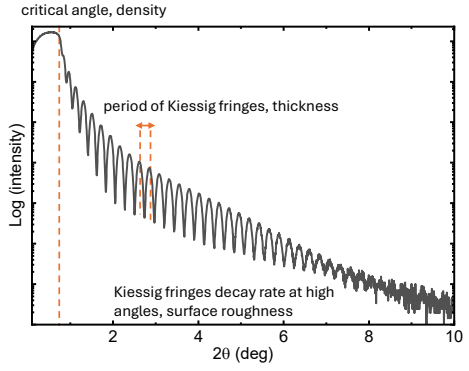

Figure 6. X-ray reflectivity pattern exhibiting relations between the features of the pattern and the parameters obtained by modelling of XRR patterns.

5.4. X-ray absorption spectroscopy (XAS) and X-ray photoelectron spectroscopy (XPS)

XAS is a technique that probes the local electronic and structural environment of a selected element by measuring its X-ray absorption as a function of photon energy near an absorption edge. When an X-ray excites a core electron, the resulting absorption features are divided into X-ray absorption near-edge structure

(XANES) and extended X-ray absorption fine structure (EXAFS). XANES is sensitive to the oxidation state, coordination geometry, and electronic structure of the absorbing atom, while EXAFS reports numbers, types, and distances to ligands and neighboring atoms from the absorbing element. The significant advantage of XAS over X-ray crystallography is that the local structural information around the element of interest can be obtained even from disordered samples, such as amorphous thin films. An XAS spectrum is obtained by measuring the modulation of the sample absorption coefficient as a function of the incident X-ray beam energy [154].

XPS is a surface-sensitive characterization method based on the detection of electrons emitted from a material after irradiation with X-rays. By analyzing the kinetic energy of these photoemitted electrons, it is possible to determine both the elemental composition and the chemical environment of atoms present at or near the surface. The technique is particularly powerful due to its high surface specificity and its capability to distinguish different chemical states of the same element. XPS can detect all elements except hydrogen and helium, and it has been widely applied across a broad range of materials, including polymers, textiles, geological samples, and semiconductor systems, to investigate surface composition and chemistry [155].

5.5. Nanoindentation and wear measurements

Mechanical properties of solid surfaces and thin films are important in a wide range of applications, including those requiring tribological performance. Among the mechanical properties, elastic–plastic deformation behavior, hardness, elastic modulus, scratch resistance, film-substrate adhesion, residual stresses, time-dependent creep and relaxation properties, fracture toughness, and fatigue are the most interesting ones. Nanomechanical properties of thin films are commonly measured using depth-sensing nanoindentation techniques. During the indentation process, the nanoindentation apparatus continuously monitors the applied load and the position of the indenter relative to the specimen surface, that is, the indentation depth or displacement. Indentation experiments can be carried out at penetration depths of only about 5 nm [156]. Oliver and Pharr in 1992 developed an analysis method for instrumented indentation tests that allows hardness and reduced elastic modulus to be determined from the unloading response, for the characterization of small-scale materials [157,158]. A schematic representation of a typical data set obtained with a Berkovich indenter by this method can be observed in Figure 7. The indentation load, (P), is applied to the sample, resulting in a displacement (h), relative to the initial undeformed surface. For modeling purposes, the deformation occurring during loading is assumed to consist of both elastic and plastic components, leading to the formation of a permanent hardness impression. During unloading, it is assumed that only the elastic displacements are recovered. This method cannot be applied to materials in which plasticity

reverses during unloading, while computational calculations confirmed that reverse plastic deformation is usually negligible.

Several parameters allow us to determine the elastic modulus E and hardness H of the films. P_{max} is the maximum load applied by the indentation tip, h_f is the final depth of the indent, h_{max} is the maximum displacement achieved by the tip, and S is the contact stiffness; $S=dp/dh_{h=hmax}$. represents the elastic recovery of the material during load removal and is commonly described using a power-law function; $P(h) = \alpha\ (h - h_f)^m$, where α and m are power-law fitting constants [157,158].

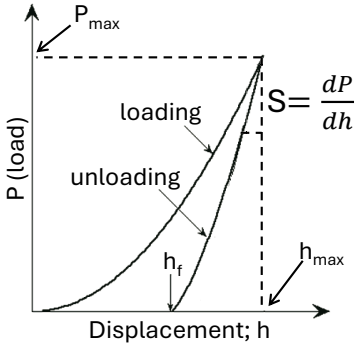

Figure 7. Load – displacement curve of a quasistatic nanoindentation measurement [157].

In this case, the hardness of the material is equal to the mean contact pressure, i.e. the ratio of the applied maximum load and projected area of the indent;

$$H = \frac{P_{max}}{A(h)} \tag{2}$$

The exact procedure is based on analysis of the unloading curve shown schematically in Figure 8. During the test, load and displacement are measured directly, and the hardness and elastic modulus are then calculated from the unloading response using the estimated contact area, A, and the indentation geometry. The contact area depends on the geometry of the indenter tip, which may be spherical, conical, or pyramidal. In this work, the Berkovich tip is considered, which is three-sided pyramid with a face angle of 65.27°.

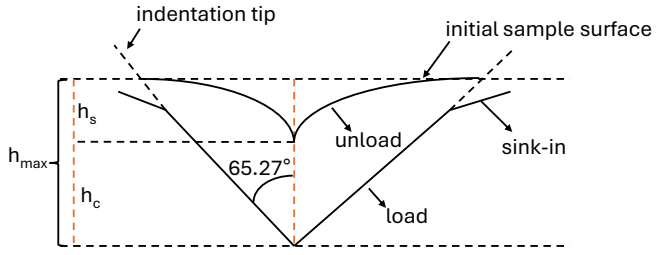

Figure 8. Schematic of the loading-unloading process under applied load, including parameters characterizing the contact geometry.

The contact area function, *A(h),* defines the relationship between the projection of the contact area and the displacement of the tip in the sample. For the ideal geometry of this type of tip, the contact area function is

$$A(h) = 24.5h_c^2, \tag{3}$$

where h_c is the contact depth calculated from the maximum indentation depth h_{max}, maximum load P_{max}, and contact stiffness S, the value of displacement that includes both elastic and plastic deformation. h_s in Figure 4 shows us the level of sink-in. The amount of sink-in depends on the applied load, stiffness of the material, and probe geometry. Assuming that pile-up is negligible, the elastic models show that the amount of sink-in, h_s, is given by:

$$h_s = \epsilon P_{max}/\mathrm{S}, \tag{4}$$

where ϵ is a constant that depends on the geometry of the indenter, and for Berkovich tip it is equal to 0.75. Thus, in this regard, h_c can be calculated as

$$h_c = h_{max} - \frac{0.75\,P_{max}}{\mathrm{S}} \tag{5}$$

The elastic modulus is determined based on its connection to the contact area and the unloading stiffness that has been measured;

$$S = \frac{2\beta E_{eff}\sqrt{\mathrm{A}}}{\sqrt{\pi}} \tag{6}$$

Where E_{eff} is the effective elastic modulus calculated by

$$\frac{1}{E_{eff}} = \frac{1-\nu^2}{E} + \frac{1-\nu_i{}^2}{E_i} \tag{7}$$

The effective elastic modulus considers that both the sample (with Young's modulus E and Poisson's ratio ν), and the indenter (with elastic constants E_{i} and ν_{i}) undergo elastic deformation. Furthermore, the stiffness S is calculated using a general relationship that does not depend on the specific shape or geometry of the indentation [157–159].

In the Oliver–Pharr analysis, the contact area is determined from the contact depth h_c, but this method does not consider the pile-up of material around the indentation mark, which is observed in many elastic–plastic materials. When pile-up happens, the actual contact area becomes larger than the value predicted by the method. As a result, both the hardness and the elastic modulus are calculated as higher than their true values, sometimes by as much as 50%. This problem occurs because the contact depth is determined using an elastic contact analysis, which cannot properly account for pile-up [157–159].

5.5.1. Substrate effect on the thin film mechanical properties

Indentation testing of thin films on substrates is challenging because the substrate affects the measured response. The indentation behavior of a film-substrate system is governed by a complex interaction between the elastic and plastic properties of both the film and the substrate, which makes isolating the film's intrinsic mechanical properties difficult. According to the previous reports, the effect of the substrate hardness on the film hardness was negligible in the case of soft films on hard substrates because the plastic deformation was contained within the film, and the substrate yielded plastically only when the indenter penetrated the substrate [159,160]. But this is possible only when the true contact area can be calculated by accounting for the material that piled up around the indent. If the contact area is calculated with the Oliver–Pharr method, which ignores pile-up, the hardness appears to rise with indentation depth, which is considered a substrate effect. However, changes in hardness with indentation depth are not caused by pile-up alone, but may also result from surface roughness, substrate effects, and film damage such as cracking or delamination. When a hard film is deposited on a soft substrate, the substrate significantly affects the measured hardness of the film since the soft substrate begins to deform plastically even when the indentation depth is still smaller than the film thickness. Compared to hardness, measuring the elastic modulus of thin films by nanoindentation is much more affected by the substrate. This is because the elastic deformation caused by the indenter is not limited to the film; it extends deep into the substrate, especially when the film is very thin. As a result, even at small indentation depths (less than about 10% of the film thickness), the stiffness of the substrate influences the measured contact stiffness [160]. As a rule of thumb, indentation depths below approximately 10% of the film thickness are often used to minimize substrate influence. However, the accuracy of the measured hardness also depends on surface deformation effects such as pile-up or sink-in, which can affect the estimated contact area.

5.5.2. Nanowear measurements of thin films

The nano-wear test is a nanotribological characterization method for evaluating the wear durability of thin films on the nanometer scale and nano/micro-Newton scale. Wear tests can be applied using the same tribo-indenter and Berkovich tip. A scanning wear test is performed by scanning an area a prescribed number of passes at an elevated setpoint and then measuring the height difference from the surrounding area to calculate the amount of material worn away (Figure 9). To measure wear performance, the wear scan area, indentation load, and number of wear scan cycles are adjusted in the program. Using the post-wear scanning probe microscope images and the TriboView program (Hysitron, Inc. 6.0.0.0), it is possible to calculate the height in the worn area and wear volume for the sample (equations 8 and 9). The apparent rough spikes in Figure 9 b are the result of Z-axis scaling in Gwyddion (version 2.71), and the actual surface is much smoother in reality.

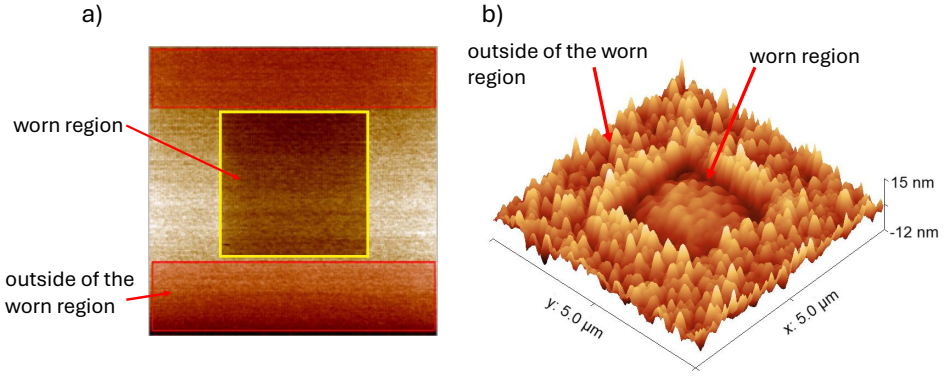

Figure 9. a) 2D post wear image to calculate wear volume. b) 3D post wear image of the thin film, where the inside and outside of the wear region can be clearly observed.

The wear height (W_h) and wear volume (W_v) is calculated based on the post-wear topographic scanning probe microscope (SPM) images using the following formula

$$W_h = |H_o| - |H_i|, \tag{8}$$

$$W_v = S \times W_h\,, \tag{9}$$

where H_o is the average height of the area outside the wear region (as shown in Figure 9), and H_i is the average height of the area inside the wear region (Figure 9) and S is the area of the wear scan size. Before these calculations, background subtraction in TriboView is applied to remove any overall tilt or large-scale curvature from the post-wear image. This operation flattens the scan by fitting and subtracting a plane or low-order surface so that H_o and H_i are measured with respect to the same baseline.

5.6. Optical properties by spectroscopic ellipsometry

Optical property refers to a material's response to exposure to electromagnetic radiation, in particular, to visible light. Visible light lies within a very narrow region of the spectrum, with wavelengths ranging between about 0.4 μm and 0.7 μm. The optical phenomena that occur within solid materials involve interactions between the electromagnetic radiation and atoms, ions, and/or electrons. Parameters such as the refractive index, extinction coefficient, and optical band gap are crucial for evaluating the suitability of thin films for optical coatings [35], solar absorbers [161], and optoelectronic [9] applications, as they determine the transmission, reflection, and absorption behavior of the material [162,163].

When light proceeds from one medium into another, some of the light radiation may be transmitted through the medium, some will be absorbed, and some will be reflected at the interface between the two media. Light that is transmitted into the material experiences a decrease in velocity, resulting in a bend at the interface. This bending of light is called refraction. The index of refraction n of a material is defined as the ratio of the velocity in a vacuum c to the velocity in the medium ν, ($n = \frac{c}{\nu}$). The magnitude of n depends on the wavelength of the light [163].

Spectroscopic ellipsometry (SE) is a non-destructive optical technique that characterizes polarized light reflection from a sample's surface. SE is used to characterize thin films and bulk materials. Film can be a single or multi-layer film with a preferred thickness between 1 nm and 1000 nm (or 1μm). The method is based on unpolarized light that is sent through a polarizer allowing only light with a certain electric field orientation to pass through. Linearly polarized light travels to the sample and reflects from the surface as elliptically polarized. Ellipsometry measures two values, amplitude ratio (tan (ψ)) and the phase difference (Δ), which describe the change in the polarization after light has interacted with the sample. The method can be used to analyze material properties, such as thickness and refractive index. It can be used for flat, transparent, and semitransparent films. Ellipsometry is an indirect method, and the measured γ and Δ cannot be converted directly into the optical constants of the sample. A model analysis and data fitting must be performed. By fitting and modelling, n, and extinction coefficient (k) in each wave length is achieved as optical constants of the sample. Later, using these constants we can calculate other optical values. For instance, absorption coefficient (α) is calculated as

$$\alpha = 4\pi k/\lambda \,, \tag{10}$$

where k is the wavelength (λ) dependent extinction coefficient.

The procedure of estimating the optical band gap is via fitting the experimentally determined absorption coefficient to the Tauc equation, which is a power-law expression in the form of

$$(\alpha h\nu)^{1/n}=A(h\nu-E_g), \tag{11}$$

where α is absorption coefficient being a function of wavelength $\alpha(\lambda)$, h is Planck constant, E_g is the optical band gap of a semiconductor, ν is frequency, A is a proportionality constant, and n is the Tauc exponent. Tauc exponent is typically chosen as one of four values depending on the type of dominating transition in a studied semiconductor and according to the commonly used rules:

n = 1/2 for direct (allowed) transitions,

n = 3/2 for direct (forbidden) transitions,

n = 2 for indirect (allowed) transition,

n = 3 for indirect (forbidden) transitions [162].

The dominant optical transition was identified by comparing Tauc plots constructed using different exponent values and evaluating the linearity of the absorption-edge region. The transition model yielding the most pronounced linear dependence and the most reliable extrapolation to the photon-energy axis was considered to best represent the optical absorption process in the investigated films. In the present work, Tauc plots calculated using (n = 1/2) and (n = 2) were analyzed.

6. EXPERIMENTAL DETAILS

6.1. Atomic layer deposition of thin films

The films investigated in this study were deposited on Si (100), SiO_2, sapphire substrates by the atomic layer deposition (ALD) method. The exact deposition conditions and time schedules for binary[1] Cr_2O_3 and ternary[2] CTO[3], CAO[4] films detailed in the original publications I, III, IV, and V.

Ternary chromium hafnium oxide films (CHO)[5] films were deposited using an in-house built flow-type thermal ALD reactor [164] at T_G=275 °C.

The metal precursors for deposition of Cr_2O_3 were $Cr(thd)_3$ (99.99%, Strem Chemicals, Inc), and $HfCl_4$ (99.9%, Strem Chemicals, Inc) for deposition of HfO_2. Ozone (O_3) was used as an oxygen source.

The deposition of CHO films included, depending on the desired composition, from 1 to 500 ALD cycles of $Cr(thd)_3$-O_3 followed by one ALD cycle of $HfCl_4$-O_3. That kind of supercycle was repeated from 8 to 800 times to achieve films with approximately similar thickness values (Table 5). The ALD cycle parameters used in $Cr(thd)_3$-O_3 and $HfCl_4$-O_3 deposition processes, including metal precursor exposure, N_2 purge, O_3 exposure, N_2 purge, were 5, 2, 2, 5 s, and 2, 2, 5, 5 s, respectively. During the deposition, the total gas pressure in the reaction chamber was maintained at about 210–220 Pa, and the nitrogen carrier gas flow rate at 230 sccm. It is worth mentioning that all deposited films in the current research were visually uniform in colour on the substrates.

Table 5. ALD supercycles used for deposition of CHO films using k × ($Cr(thd)_3$-O_3) + ($HfCl_4$-O_3).

Supercycle formula	Number of ALD supercycles	Thickness (nm)
500(Cr-O) + (Hf-O)	8	36
225(Cr-O) + (Hf-O)	16	36
75(Cr-O) + (Hf-O)	45	34
35(Cr-O) + (Hf-O)	100	33
15(Cr-O) + (Hf-O)	180	32
5(Cr-O) + (Hf-O)	500	40
(Cr-O) + (Hf-O)	800	78
$HfCl_4$ + O_3	500	80

[1] binary denotes the film containing two different elements.

[2] ternary denotes the film containing three elements.

[3] chromium titanium oxide.

[4] chromium aluminum oxide.

[5] chromium hafnium oxide.

6.2. Characterization methods

Films were characterized in terms of elemental and phase composition, crystallinity, crystallite size, mosaicity, thickness, mass density, surface roughness, ionic state of metal elements, hardness, elastic modulus, wear resistance, refractive index, extinction coefficient and optical band gap energy.

Elemental compositions used for calculating of atomic growth per cycle (AGPC) were measured on (XRF) spectrometer ZSX400 (Rigaku). For a few Cr-Al-O/Si, and Cr-Al-O/sapphire films the mapping of elements in thin lamella cross-section (prepared on FEI Helios NanoLab 600 Dual Beam system) of films was measured using scanning transmission electron microscopy (STEM) on FEI Titan Themis 200 operated at 200 kV and equipped with SuperX energy-dispersive X-ray (EDX) spectrometer (FEI, Bruker).

Phase composition of the films was characterized by XRD using either parallel beam medium resolution (MR) grazing incidence (GI, incident angle ω = 0.5°) geometry, or symmetrical θ/2θ and in-plane setup in high resolution (HR) setup where Ge (220) two-bounce monochromator was implemented for X-ray monochromatizing. Most of the measurements were performed at room temperature. For in-situ high temperature XRD and XRR analysis a sample chamber DHS 1100 (Anton Paar) was used for heating the films from 300 °C to 900 °C in steps of 100 °C with total of 30 min measurement at every step and a ramp of 10 °/min in between the steps. Phase composition of a few films was determined using transmission electron diffraction (ED) on microscope (ARM-200F, JEOL).

Thickness, density and surface roughness of the films were characterized by XRR in medium or high-resolution geometry. XRR and XRD measurements were performed on an X-ray diffractometer SmartLab (Rigaku) using scintillation detector and Cu Kα radiation (λ=0.154059 nm (HR) or λ=0.15418 nm (MR), tube power 8.1 kW). Programs GlobalFit (Rigaku), PDXL (Rigaku), an upgraded version of AXES [165] and ICDD database PDF-2 (versions 2017–2023) were used for XRD and XRR data analysis.

Oxidation state of Cr in the Cr-Al-O/sapphire films was analyzed using XAS by measuring photocurrent (0.1 eV spectral resolution) in total electron yield mode on Solid State Endstation (SSES) of the FinEstBeAMS beamline at the MAX IV synchrotron light source in Lund, Sweden. A clean mesh of Au located behind the last optical element was used for normalizing the observed signal to a reference signal. Additionally, XPS were collected at normal emission using a Gammadata/Scienta SES100 hemispherical analyser and a Thermo VG Scientific XR3E2 non-monochromatic dual-anode X-ray source (Al-K_α/Mg-K_α), at an overall spectral resolution of approximately 0.8 eV. The analyser energy scale calibration was checked against the $4f_{7/2}$ line from a cleaned gold foil at 84.0 eV binding energy. Relevant to estimating elemental composition from XPS survey scans, the constant (i.e., independent of photoelectron kinetic energy) analyser transmission function was checked against accessible core level lines of clean Au, Ag and Cu samples, and additionally asserted by constant magnification in spatial imaging (in the non-energy-dispersive direction) of a structured test sample

through the electron optics over the entire used kinetic energy range. Spectral components fitting and elemental composition analysis from survey spectra were done using CasaXPS software, taking into account the photoionization cross-sections at the excitation energy used, and the measurement geometry. To estimate the (kinetic energy dependent) depth range of origin of detected photoelectrons, their inelastic mean free path (IMFP) was estimated using the TPP2M formula [166] and also weighed into the XPS sensitivity factor of each core level. Since the sapphire substrate is an insulating material, sample charging had to be corrected. This was done by adjusting the adventitious carbon (typically present in ex situ measured samples) C 1s peak to 285 eV binding energy (assuming sp^3-hybridised carbon species to be dominant). However, recent systematic studies on this widely used C 1s XPS referencing method have shown that adventitious carbon tends to reference itself to the vacuum level rather than to the Fermi level of either the sample or the spectrometer. Hence, its position in the Fermi-level referenced binding energy scale would become subject to change corresponding to eventual variation of the work function differences between the spectrometer and any of the samples in the series [167]. Therefore, the calibration was additionally verified by comparison with several films deposited simultaneously on silicon substrates during the same ALD process, which did not exhibit charging effects. Furthermore, the consistency of the O 1s and Al 2s peak positions, as well as their relative energy separations, was checked against the reported NIST X-ray Photoelectron Spectroscopy Database (accessed Apr. 22, 2026). After confirming consistency throughout this careful calibration procedure, we gained confidence in reporting the observed binary/ternary oxide binding energy shifts of ~1 eV for the Al 2s peak and ~1.5 eV for the O 1s peak. Given the uncertainty of this procedure, which we estimate to be on the order of ~0.25 eV, as well as possible spectral multiplet variations caused by crystal-field changes induced by composition-dependent lattice strain [168,169], we could not rule out a reverse energy shift of the Cr 2p peaks in the binary/ternary oxide comparison, relative to the Al 2s shift, as suggested in some literature. However, the evidence is insufficient to claim this with certainty.

Hardness, elastic modulus, and wear resistance of the deposited films were investigated using nanoindentation on Hysitron Triboindenter TI 980 (Bruker) using a Berkovich-type diamond tip. Fused quartz (Bruker) served as a calibration standard that showed hardness and elastic modulus of ~9.2 ± 0.9 GPa and ~70 ± 6 GPa, respectively (Figure 10). Before starting the measurement of samples calibration and renewing the probe area function was performed by applying averaging over 20 measurement points of the standard sample. Measurements were performed under the load of 500 μN repeated at about 30 different points on each sample. Measurements located at maximum of five defective points showing hardness and modulus values falling considerably outside of the values at the remaining measurement points were removed before averaging and calculating standard deviations. The effect of substrate on the hardness and elastic modulus values of the films was minimized by observing the data points near the

indenter tip displacement of 5 to 15 nm for the films in the thickness range of 30 to100 nm.

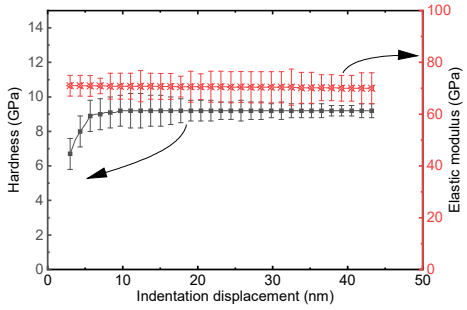

Figure 10. Results of nanoindentations (mean values) on the Bruker standard fused quartz sample to test the reliability of the probe area function and find the lowest valid displacement range.

The wear height (W_h) and wear volume (W_v) over area of 3×3 μm^2 (Cr-Al-O films) or 5×5 μm^2 (Cr-Hf-O films) were calculated (as discussed in 4.5.2) from the post-wear topographic scanning probe microscope (SPM) images using the computer program TriboView (Bruker). Track areas of 2×2 and 1×1 μm^2 were used to study the wear-resistant properties of the films. Wear tests were performed under loads in the range of 60 to 180 μN using 2, 6, and 10 passes.

Refractive index (n), and extinction coefficient (k), of the films in the wavelength range of 225–954 nm (photon energy 1.3–5.5 eV) were determined using SE GES5E and SEA software (Semilab Sopra). Two Tauc-Lorentz oscillators in one-layer model were used for both binary and ternary films (Cr-Ti-O, Cr-Al-O, Cr-Hf-O deposited by $Cr(thd)_3$ in combination with O_3 as a Cr-O source. In the case of Cr-Ti-O films where CrO_2Cl_2 was the Cr precursor, a mix of Tauc-Lorentz + Lorentz oscillators was implemented together with a model consisting of two layers: the main investigated layer and a low-density top layer taking into account a possible surface roughness effect. E_g was determined from Tauc plots using either direct allowed or indirect allowed transition models.

7. RESULTS AND DISCUSSION

This chapter gives the overview of the studies made in the investigation of the Cr_2O_3 film properties [III], deposition of CTO films using different precursor combinations and substrates [III,IV], and growth of the CAO [I,V] and CHO films. Moreover, it will give an overview of how the properties of the Cr_2O_3 films mixed with Ti, Al, and Hf depend on their elemental composition.

7.1. Atomic layer deposition of Cr_2O_3 using $Cr(thd)_3$ and ozone

To investigate how the growth and properties of Cr_2O_3 thin films synthesized using $Cr(thd)_3$ and O_3 depend on T_G, films were deposited 2000 ALD cycles in the T_G range of 200 to 300° [III]. As shown in Figure 11 a, Cr atomic growth per cycle increased from 0.09 to 0.35 atom/nm^2 (corresponding to 0.032–0.105 Å/cycle or 0.0032–0.0105 nm/cycle) as T_G increased from 200 °C to 275 °C. For comparison, when T_G was increasing from 150 °C to 300 °C, the growth rate of Cr_2O_3 films deposited from $Cr(acac)_3$ and O_3 increased from ~0.035 to ~0.3 Å/cycle [67] and 0.9 to 1.0 Å/cycle at T_G of 375 °C for Cr_2O_3 films deposited by CrO_2Cl_2 and CH_3OH [27]. The relatively low growth rate observed with $Cr(thd)_3$ and O_3 can be advantageous for fabricating ternary or doped films, as it enables more uniform dopant distribution and better control over dopant concentration.

XRR results demonstrated that the film density values for the films deposited by 2000 cycles, showed only minor variation across the investigated T_G range, increasing slightly from 4.8 to 5 g/cm^3 (Figure 11 a). The small increase in density correlates with the structural changes investigated using the GIXRD analysis (Figure 11 b). With increasing T_G from 250 to 300C, an overall increase in total diffraction intensity as well as changes in the relative intensities of the diffraction peaks were observed. At $T_G \leq 225$ °C, the films were X-ray amorphous. In contrast, the films deposited at T_G from 250 °C to 275 °C showed a crystalline structure with diffraction reflections corresponding to the eskolaite phase. Furthermore, notable changes in the relative intensity values of the observed diffraction reflections were detected when the T_G increased from 275 to 300 °C. These changes were characterized by texture coefficients (*TC*) calculated for the dominating 012, 104, 110 and 116 reflections as a function of the T_G (Table. 6). The highest *TC* was observed for the 104 reflections for the film deposited at T_G = 275 °C, however, for the film deposited at T_G = 300 °C, the highest *TC* was observed for the 012 reflection.

Table 6. Texture coefficient (*TC*) values calculated for different reflections for Cr_2O_3 films at T_G of 275 and 300 °C.

hkl	TC at 275 °C	TC at 300 °C
012	0.9 ± 0.09	1.4 ± 0.14
104	1.6 ± 0.16	0.7 ± 0.07
110	0.3 ± 0.03	0.8 ± 0.08
116	1.0 ± 0.1	0.9 ± 0.1

The film deposited at 300 °C showed more polycrystalline character compared to the textured films deposited at temperatures from 250 to 275 °C. Surface roughness values of the films changed from 0.4 to 3.4 nm by increasing T_G from 200 to 300 °C, being in relation with the changes in phase composition of films from X-ray amorphous to polycrystalline and textured structure.

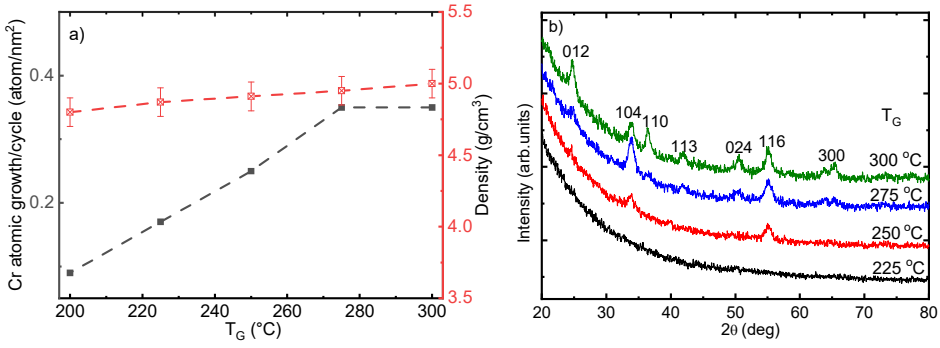

Figure 11. a) Cr_2O_3 mass growth and density. b) GIXRD patterns of Cr_2O_3 films deposited at different T_G. The labels at the reflections are Miller indices of atomic planes of eskolaite phase.

However, for depositions made at 275 °C and 300 °C using ALD cycle parameters of 5/2/5/5 s, the samples positioned near the precursor inlet were found, based on XRF results, to be thinner than those located farther away. To better understand this phenomenon, additional depositions were made using different O_3 pulse durations (Figure 12 a).

An increase in Cr atomic growth per cycle was observed as the O_3 exposure time increased from 1 to 3 s. However, when O_3 exposure time exceeded 3 s the atomic growth rate of films decreased (Figure 12 a). This suggests that an excessive amount of ozone in the reaction zone at these T_G may lead to the formation of volatile or gaseous phase byproducts, such as metal oxide with a higher oxidation state (e.g. CrO_3) [170], thereby reducing the film growth. A similar behavior has previously been reported for the deposition process using $Cr(acac)_3$ and O_3, showing that the growth rate per cycle of Cr_2O_3 films depended on the O_3 exposure duration, and excessive O_3 pulse time led to the continuous and spontaneous etching of the growing film [67].

GIXRD analysis revealed that the crystallinity of the films improved as the O_3 exposure time increased from 1 s to 2 s. However, when the ozone exposure exceeded 2 s, a gradual decrease in the intensity of diffraction peaks was observed, indicating a decrease in film crystallinity (Figure 12 b, at 3 s and 5 s).

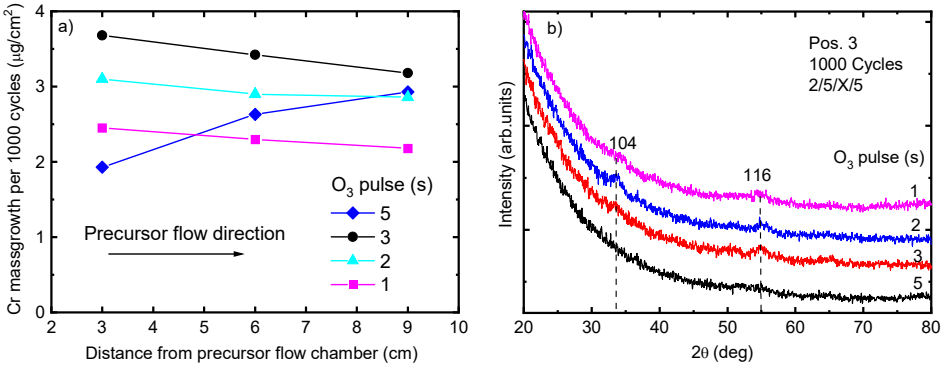

Figure 12. a) The variation of Cr mass growth of Cr_2O_3 deposited at T_G = 275 °C using different O_3 exposure times as a function of substrate distance from the precursor gas flow chamber. b) GIXRD patterns showing the indexed reflections of the eskolaite phase at different O_3 exposure times (x) and purging time of 5 s.

The thickness of the Cr_2O_3 films changed linearly from 5 to 21 nm by increasing the number of ALD cycles from 500 to 2500 for films deposited at T_G = 275 °C with constant precursor pulses of 5/2/2/5 (Figure 13 a). Microstructure analysis of the films showed structural changes from X-ray amorphous for the film with thickness of 5 nm to polycrystalline by increasing thickness up to ~21 nm (Figure 13 b). Since GIXRD is not sensitive enough for measuring the crystallinity of films with thickness at and below 5 nm, it was not possible to determine the presence or absence of crystalline seeds in the thinnest (5 nm) film of this study.

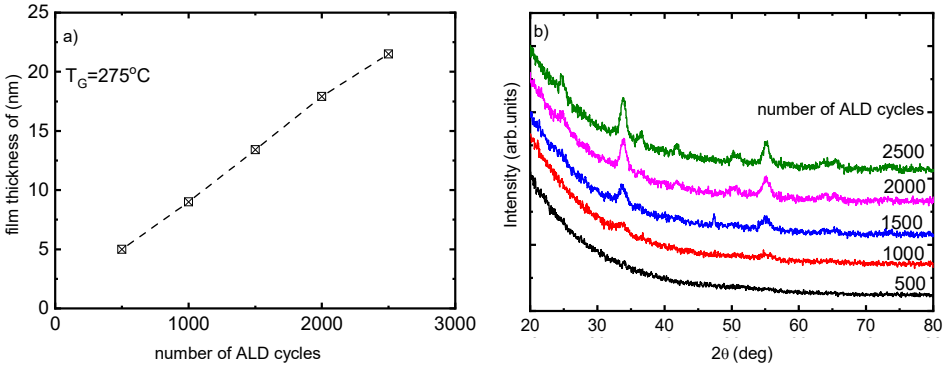

Figure 13. a) The variation of Cr_2O_3 film thickness with the number of ALD cycles deposited at T_G = 275 °C and precursor pulses and purging duration of 5/2/2/5 (s). b) GIXRD patterns of Cr_2O_3 films deposited in variation with the number of ALD cycles. The labels at the reflections are Miller indices of atomic planes of the eskolaite phase.

7.2. Atomic layer growth of ternary compound films

The film growth rate was characterized as a surface density of Cr and Me (Me = second metal precursor, including Ti, Al or Hf) atoms deposited per one ALD cycle. The results showed that the growth rate of Ti and Al was higher when deposition was performed on surfaces previously exposed to $Cr(thd)_3$ and O_3 compared to the values seen in the case of the deposition of binary TiO_2 and Al_2O_3 under the same conditions. For instance, the growth rate of Ti atoms was the highest when an ALD supercycle consisting of fifteen $Cr(thd)_3$ and O_3 cycles followed by one $TiCl_4$ and O_3 was applied. Under these conditions, the Ti growth rate reached approximately 3.5 atoms/nm^2, which is about 1.8 times higher than obtained when TiO_2 was deposited on a silicon substrate (Figure 14 a). Similarly, the growth rate of Ti atoms was the highest when using the ALD supercycle consisting of ten cycles of $CrCl_2O_2$-CH_3OH and one cycle of Ti-O, resulting in a growth rate of about 2.9 atoms/nm^2 for Ti, about 2.4 times higher than when TiO_2 was deposited on a silicon substrate. Al growth rate reached approximately 2.7 times higher on Cr-O surface compared with its growth rate when Al_2O_3 was deposited on Si substrate. However, in the case of Hf atoms, the situation was different. The growth rate of Hf atoms was remarkably higher in the case of deposition of binary HfO_2 on Si compared when less than 15 cycles of Cr-O had been used in super-cycle of Cr-Hf-O deposition (Figure 14 a).

This points to a more efficient nucleation of TiO_2 and Al_2O_3 on Cr_2O_3 compared to that on the already deposited layer of TiO_2 and Al_2O_3, but less efficient nucleation of HfO_2 on Cr_2O_3 compared to that of the binary deposited HfO_2 film. Since the efficiency of forming the nucleation centers is proportional to the area of the substrate, a possible explanation for this higher growth rate could be related to the differences in roughness values of binary component Cr_2O_3 deposited by ($CrCl_2O_2$-CH_3OH), and TiO_2 films, e.g., 6 nm compared to 4.5 nm, respectively, 2.5 nm to 0.58 nm for binary Cr_2O_3 deposited by $Cr(thd)_3$-O_3 and Al_2O_3 films, respectively, and 3.7 nm for binary HfO_2 film. For the ternary films, by increasing the concentration of Me element in the films (decrease in Cr-O cycles in the ALD super-cycle), the growth rate of Cr decreased. For CTO films, the Cr growth rate was higher when $CrCl_2O_2$-CH_3OH was used as the Cr-O source than when $Cr(thd)_3$-O_3 was employed. In addition, the decrease in Cr growth rate for both CTO film types was much smaller than that observed for the CAO and CHO films (Figure 14 b).

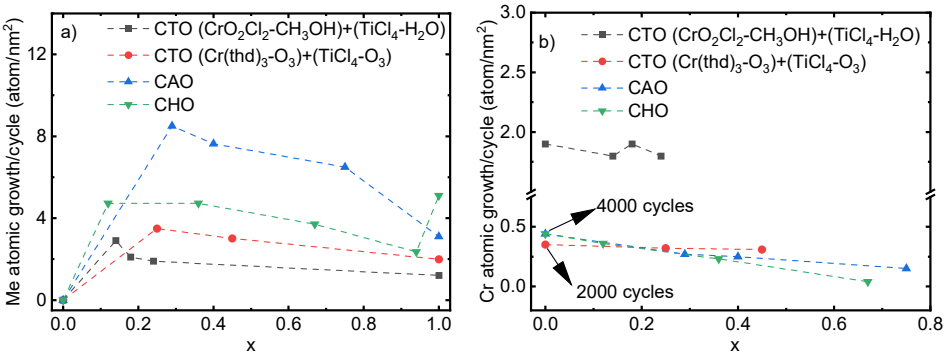

Figure 14. Atomic density of a) Ti, Hf, and Cr atoms and b) Cr atoms as a function of the x = Me/(Me+Cr) on Si substrate (Me= Ti, Al or Hf).

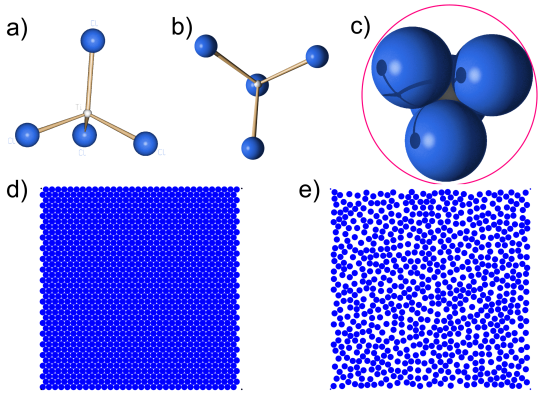

Figure 15. Models of $TiCl_4$ molecule in a) 3D ball and sticks mode; b) top view in ball and sticks mode; c) top view in space filled mode surrounded by a cycle with a diameter of 0.614 nm. Distribution of cycles with a diameter of 0.614 nm on a square area of approximately 20 × 20 nm^2 in two different arrangements: d) hexagonal closed packed and e) random. The closed-packed structure fits 1216 cycles (filling rate 89%, corresponding atomic density of Ti = 3.0 nm^{-2}) and the random distribution fits approximately 724 ±15 cycles (filling rate 54 %, density of Ti atoms = 1.8 nm^{-2}) [IV].

The possible reason for the growth rate differences could be the dissimilar structure and differences in the density of atoms on the atomic planes of eskolaite and anatase. Taking into account the approximately 0.614 nm diameter of the $TiCl_4$ molecule and assuming that during the adsorption of $TiCl_4$, only one of the Cl atoms will be released and no exchange reactions take place among the rest of three Cl atoms, the theoretical limit of the growth rate when expecting hexagonal closed-packed or random arrangement of the adsorbed molecules on the substrate would be approximately 3.0 Ti atoms/nm^2 per cycle or 1.8 Ti atoms/nm^2 per cycle (Figure 15), respectively. When comparing the ratio of observed growth rate, it is expected that the atomic growth rate of 1.8 Ti atoms/nm^2 calculated for the random distribution model is more realistic limit for estimating the theoretical

growth rates (more details in [IV]). Density and distribution of –OH sites, that is, directly proportional to the density of oxygen atoms on the surface, could be one of the main factors that determine the nucleation efficiency [171]. Crystal structure 3D visualization and calculation of atomic number density of oxygen atoms on the preferred (001) growth plane of eskolaite and anatase (001) plane showed two times higher density of O for eskolaite (14 atoms/nm^2 compared with 7 atoms/nm^2 for anatase), indicating eskolaite offers a more efficient substrate for the adsorption of $TiCl_4$ molecules.

The decrease in growth rate of Hf after Cr-O cycles can be explained by the presence of large $Cr(thd)_3$ ligands (steric hindrance), suppressing the successful reaction of $HfCl_4$ with the surface and decreasing their adsorption due to the lower density of chemisorption sites on the surface. In ALD, growth proceeds only when precursor molecules adsorb onto available surface sites, remain sufficiently stable on the surface, and react completely with the subsequent co-reactant pulse. Consequently, the quality and reproducibility of an ALD process depend strongly on the adsorption and desorption behavior of the precursor molecules, as well as on the chemical state of the substrate surface and the reactor conditions [25,172].

The observed divergence in suppressed Hf incorporation on a Cr-O surface relative to binary HfO_2, but enhanced Ti incorporation on a Cr-O surface relative to the anatase phase of TiO_2 can be rationalized by surface-chemistry-controlled chemisorption and substrate-dependent nucleation effects inherent to ALD. Specifically, the amount of metal precursor adsorption during the pulse is governed by the density and nature of reactive surface functionalities generated by the immediately preceding $Cr(thd)_3$-O_3 step (e.g., hydroxylated vs. bridged oxygen terminations, defect sites, and local acidity/basicity). For $HfCl_4$, it is observed that the Cr-O termination produced at the ternary growth temperature is comparatively less favorable for $HfCl_4$ chemisorption than an HfO_2-terminated surface. In contrast, $TiCl_4$ can exhibit substrate-enhanced nucleation when presented with a surface offering a higher density of reactive oxygen-based sites than that of a crystalline anatase TiO_2 surface under identical conditions; both theoretical and experimental studies emphasize that $TiCl_4$ adsorption and ligand dissociation are highly dependent on the availability and reactivity of surface functional groups.

Steric effects are also highly important. Even when many reactive sites are present, precursor ligands may occupy significant surface area and prevent neighboring sites from being accessed. This steric hindrance can limit the achievable surface coverage and therefore reduce the growth per cycle relative to the ideal thickness of a complete structural layer. Thus, adsorption in ALD is governed not only by the number of reactive sites but also by the molecular size, geometry, and packing behavior of the precursor. In practice, bulky ligands may improve volatility but simultaneously reduce surface accessibility, creating a trade-off between gas-phase transport and surface reactivity [24,25].

7.3. Structural characteristics of the Cr-containing ternary oxide films

The influence of dopant type and its concentration on the phase composition, crystallinity, and preferred orientation of chromium oxide-based thin films was investigated for three types of Cr-containing ternary component oxides.

The structure of the chromium titanium oxide (CTO) deposited by super-cycle $10 \times (CrO_2Cl_2 - CH_3OH) + l \times (TiCl_4 - H_2O)$, where l = 1, 2, 3, resulting in ternary films with the value of x from 0.14 to 0.24, respectively, was crystalline containing eskolaite on both Si and SiO_2 substrates (Figure 16 a, b). This phase was identified by diffraction reflections observed at diffraction angles of 33.59°, 39.8°, 55.01°, 63.61°, 73°, indexed as 104, 006, 116, 214 and 10.10 (ICDD PDF-2 card number 00-038-1479). Cell parameters of the eskolaite phase did not depend on the ALD super-cycle and substrate type and matched within the standard deviation with the cell parameters of a single crystal of eskolaite. This result was expected if we take into account the relatively low concentration of Ti in all of the films (maximum 9 atomic%) and the small differences in atomic radii of Cr^{3+} (0.62 Å) and Ti^{4+} (0.68 Å) [76,173]. The growth of the eskolaite phase showed a preferred orientation for all of the CTO films, grown both on Si and SiO_2 substrates. Texture coefficient (*TC*) was the highest for the 006 reflection and showed an increase from 1.7 to 2.6 for films on Si substrates and remained constant at about 2.0 for films on SiO_2 substrates when the concentration of Ti increased. Although only the symmetrical $\theta/2\theta$ XRD analysis enables the determination of the preferred growth plane unequivocally, it was still possible to conclude (with a precision of +/–20° that takes into account the asymmetricity of the GIXRD geometry) that for all of the CTO films the growth of eskolaite phase proceeded preferentially in the crystallographic [001] direction. For the CTO films deposited by ALD super-cycle $k \times (Cr(thd)_3\text{-}O_3) + (TiCl_4\text{-}O_3)$, the phase composition of the films changed from crystalline to X-ray amorphous by increasing the value of atomic ratio x = Ti/(Ti+Cr) from 0 to 0.45 (Figure 16 c), indicating that increasing the Ti concentration in the films led to a decrease in the crystalline fraction of the films. It is important to note that these CTO films were thinner (in the thickness range of 20 to 22 nm) compared with the films that were deposited by $k \times (CrO_2Cl_2\text{-}CH_3OH) + l \times (TiCl_4\text{-}H_2O)$.

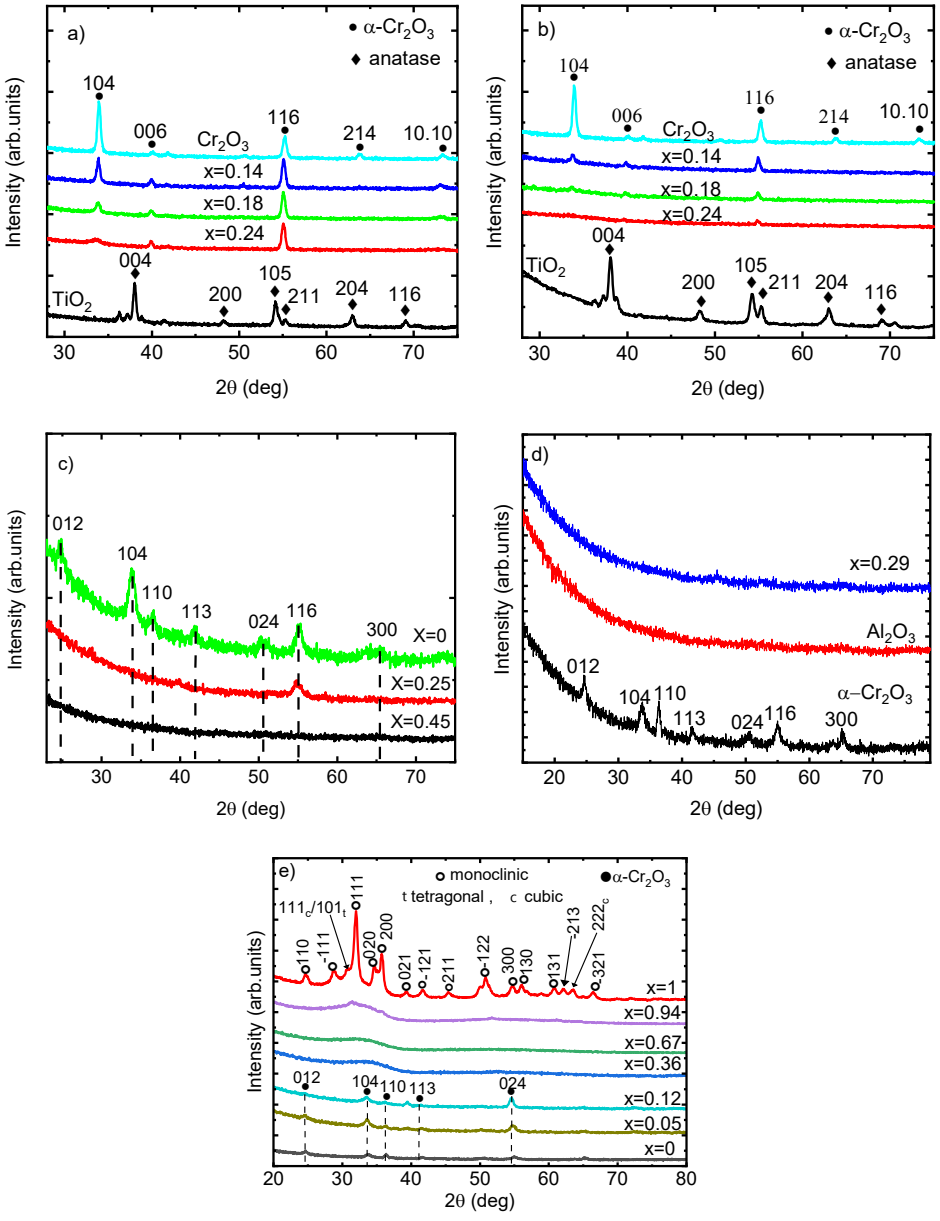

Figure 16. GIXRD patterns of CTO films deposited by 10 × (CrO_2Cl_2 – CH_3OH) + l × ($TiCl_4$ – H_2O) ALD super-cycle (l = 0, 1, 2, 3) on a) Si and b) SiO_2, and c) CTO films deposited by k × ($Cr(thd)_3$–O_3) + ($TiCl_4$–O_3) ALD super-cycle (k = 15, 30) , d) CAO, and e) CHO films on Si substrates.

CAO films deposited by $k \times (Cr(thd)_3\text{-}O_3) + (TMA\text{-}O_3)$ were either amorphous or barely detectable nanocrystalline (Figure 16 d). The amorphous structure of binary Al_2O_3 films, being in agreement with the previously published reports [174], was confirmed by the absence of any reflections on the GIXRD pattern. CAO films with different values of $0.29 \leq x \leq 0.94$ showed no diffraction peaks using GIXRD in standard configuration (e.g. step size 0.04° and a scan speed of 4.0 deg/min) (Figure 16 d).

To verify the amorphous structure of these films HRTEM and EDX analyses were performed next. EDX mapping confirmed the uniform distribution of Al and Cr across the film with $x = 0.40$, with no compositional gradients or distinct Al- or Cr-rich regions observed (Figure 17 a). High-resolution STEM analysis (Figure 15 b) together with fast Fourier transform (FFT) (Figure 17 b inset) revealed the presence of nanocrystallites with cubic symmetry and mean diameter of approximately 3–5.5 nm. Since the standard type of GIXRD did not show any remarkable diffraction from crystalline material in the CAO films, an approximately fourteen times slower GIXRD scan was performed for Al_2O_3 and CAO films. This slow-scanned GIXRD pattern of the CAO film showed three broad and weak peaks at 36.4°, 45.4° and 64.2° (Figure 17 c). The pattern from binary Al_2O_3 did not exhibit any, even barely visible, reflections, confirming again the X-ray amorphous structure of this film [I]. The crystallite size calculated from the integral width of the weak reflections from CAO film using the Scherrer equation was between 3 and 5 nm, matching well with values calculated from TEM images. Indexing of these reflections showed that these reflections can be identified as 311, 400, and 440 belonging to a phase that is isostructural with cubic η- or γ-Al_2O_3, assuming that their unit cell parameter is increased approximately from 0.799 nm to 0.817 nm. Simulation of GIXRD patterns (Figure 5 in [I]) for the candidate phases showed that the nanocrystalline phases that have η- and γ-Al_2O_3 structure and show preferred growth in the crystallographic (100) plane with mosaicity of approximately 30° are relatively similar and exhibit only three stronger reflections whose positions match well with the positions of the observed reflections of CAO films. Although these three low intensity and broad reflections did not allow to give any decisive conclusions about the structure of the observed crystallites, the increase of cell parameter of the CAO films can be explained by remarkable difference in radiuses of Cr^{3+} (0.63 Å) and Al^{3+} (0.54 Å) ions where the replacement of smaller Al^{3+} by larger Cr^{3+} has to be compensated by an increase in the unit cell parameter.

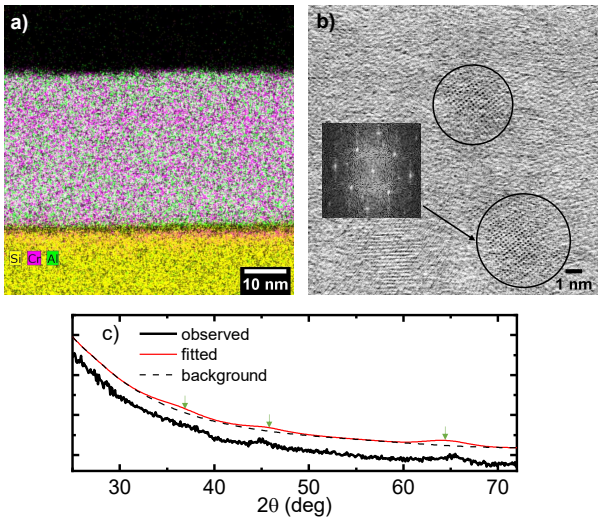

Figure 17. a) EDX mapping of the Al, Cr, and Si elements in the cross-section and b) high magnification image of ternary film with $x = 0.40$, with an inset showing the FFT pattern from the crystalline area in the film surrounded by a circle. c) GIXRD pattern of the same film together with its fitting curve (in vertical offset), amplifying visualization of three weak and broad reflections.

The structure of the ternary $(Cr_{1-x}Hf_x)_2O_3$ films showed a significant dependence on the Hf concentration in the films (Figure 16 e). When Hf atomic ratio (x) was up to 0.12, the films displayed crystalline phase and became X-ray amorphous when $x \geq 0.36$. The crystalline phase(s) in the film appeared again when x increased to 0.94. Reflections at diffraction angles of 24.53°, 33.62°, 36.29°, 41.51°, 50.29°, 54.90°, 65.18° were identified originating from the following atomic planes of α-Cr_2O_3: 012, 104, 110, 113, 024, 116 (ICDD PDF-2 card # 38-1479), appeared when $0.05 \leq x \leq 0.12$. However, in the binary HfO_2 film a mixture of monoclinic HfO_2 (ICDD PDF-2 card # 00-006-0318) and tetragonal HfO_2 (ICDD PDF-2 card # 01-078-5756) appeared. A very weak reflection was observed for the Hf reach film with $x = 0.94$, which can be assigned to tetragonal indexed as 101 (or cubic indexed as 111). Its shift to a higher angle of approximately 0.4° compared the position of HfO_2 reflection of the corresponding phase, can be explained by the doping effect of Cr atoms. In the binary HfO_2 film, monoclinic HfO_2 phase (ICDD PDF-2 card number 00-006-0318) appeared together with traces of tetragonal HfO_2 (ICDD PDF-2 card number 01-078-5756).

The influence of dopant incorporation was also clearly reflected in the density and surface morphology of the films. The density of both binary Cr_2O_3 films deposited by CrO_2Cl_2-CH_3OH (97 nm) and $Cr(thd)_3$-O_3 (~55 nm) on a silicon substrate was 5.23 g/cm^3 which matches well with the density of eskolaite phase (5.23 g/cm^3, ICDD PDF-2 card number 00-038-1479). For the films deposited by super-cycle $10\times$ (CrO_2Cl_2-CH_3OH) + l × ($TiCl_4$-H_2O), by increasing the concentration of Ti, the density of films decreased (Figure 18 a). Similar behavior was observed for the films deposited by super-cycle $k\times$($Cr(thd)_3$-O_3) + ($TiCl_4$-O_3).

For all ternary systems, the film density remained between the densities of the two corresponding binary oxides, and with increasing x = Me (Me + Cr), Me = Ti, Al, Hf, it progressively approached the density of the binary Me_xO_y film, and was not considerably influenced by the structure of the films (Figure 18 a). For instance, the decrease in density of the CTO films deposited with different ALD processes, by increasing the concentration of Ti can be explained by the difference in densities of Cr_2O_3 and TiO_2 anatase (3.96 g/cm^3, ICDD PDF-2 card number 01-075-2552). The density of the binary HfO_2 film of 10 g/cm^3 did not differ remarkably from the theoretical density of monoclinic HfO_2 phase (10.24 g/cm^3, ICDD PDF-2 card number 00-006-0318). The density of ternary CHO films increased with increasing the concentration of Hf in the films, remaining between the density values of binary Cr_2O_3 and binary HfO_2 (Figure 18 a). This increase can be explained again, as in the case of CTO films, by the higher density of HfO_2 compared with Cr_2O_3 films. The density of the Al_2O_3 film was 3.15 g/cm^{3,} which is considerably lower compared with that of α-, γ- and η- Al_2O_3 phases (ICDD PDF-2 card numbers 01-074-7229, 01-074-4629, 00-010-0425, 01-079-1557), but remained close to the range of densities observed previously for amorphous alumina films deposited by ALD at T_G of 450 °C [175].

Variation in roughness values (Figure 18 b) was in correlation with structural changes of the films (Figure 16). Decrease in roughness of CTO films deposited with different ALD processes, by increasing the atomic ratio of Ti (x) can be directly related to the decrease in relative crystallinity (decrease in peak intensities, Figure 16 a, c, e) of the films, indicating refinement in crystallite size of the films. It is worth noting that the lower roughness value of binary Cr_2O_3 films deposited by $Cr(thd)_3$-O_3 compared with the film deposited by $CrCl_2O_2$-CH_3OH, is due to their lower thickness, which causes lower crystallinity and a smoother surface (more details in publication [III]). In CHO films the roughness decreased monotonically from 1.7 to 0.3 nm as x increased from 0.05 to 0.94, whereas the higher surface roughness of 2.5 nm for binary chromium oxide and 3.5 nm for binary HfO_2 can be attributed to their markedly higher crystallinity (Figure 16 e).

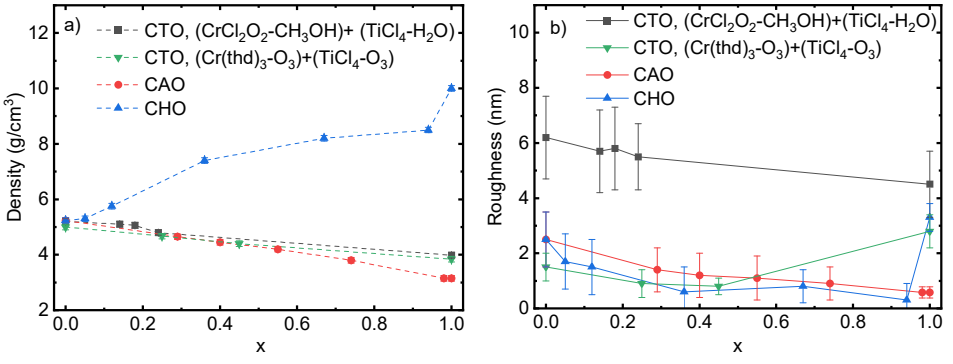

Figure 18. a) density and b) roughness values variation of binary and different chromium oxide-based ternary films on Si substrates, in variation with changes of x.

It is worth noting that the XRR oscillation patterns did not showed formation no evidence of superlattice formation in any of the ternary films, even when a large number of $Cr(thd)_3$-O_3 subcycles was used, which is also confirmed by cross-sectional EDX mapping in Figure 17 a, displaying the uniform distribution of metal elements in the film.

7.4. Hardness and elastic modulus of ternary films

The nano-indentation results showed that the mechanical properties (hardness, elastic modulus) of binary component chromium oxide thin film were remarkably different compared to these properties of ternary component CTO, CAO or CHO-type thin films.

In case of CTO films deposited using ($CrCl_2O_2$-CH_3OH) and ($TiCl_4$-H_2O) with thickness from 76 to 95 nm, the maximum observed hardness was approximately 20.5 GPa (at 15 nm indent displacement, *ID*) (Figure 19 a). This value was 5−7 GPa higher compared to the hardness of binary component Cr_2O_3 and TiO_2 films deposited at the same temperature, at the same indent displacement (~15 and ~12 GPa, respectively). The films on SiO_2 substrate showed similar hardness values to those on Si substrate [IV]. Similarly, the CTO films deposited by $Cr(thd)_3$-O_3 in combination with $TiCl_4$-O_3, with thickness in the range of 20 to 22 nm, showed hardness values approximately 3–4 GPa higher compared to the binary chromium oxide deposited by $Cr(thd)_3$-O (Figure 19 b).

Hardness of the pristine Cr_2O_3 film with ~55 nm deposited by $Cr(thd)_3$-O_3 process showed value of ~14 GPa. Maximum hardness of CAO films deposited using $k \times (Cr(thd)_3\text{-}O_3) + (TMA\text{-}O_3)$ with thickness from 35 to 50 nm was in the range of 17.5−18.4 GPa (*ID* = 10 nm) when the relative concentration of aluminum atoms (*x)* was in the range of 0.29 and 0.40 (Figure 19 c). It is important to note that the observed increase in hardness at high indentation displacements of CAO films with $x = 1.0$ and 0.98 is the effect of the Si substrate that has a slightly higher hardness of ~12 GPa [I]. Slightly higher maximum hardness of 19 GPa (*ID* = 10 nm) was observed for the CHO films (thickness in this series from 30 to 35 nm) deposited by $k \times (Cr(thd)_3\text{-}O_3) + (TMA\text{-}O_3)$ when atomic ratio, *x,* of Hf atoms was only 0.05 (Figure 19 d). The hardness of the other films of this composition in the range of *x* from 0.12 to 0.67 did not differ remarkably from the hardness of the binary chromium oxide film when considering the standard deviation of hardness.

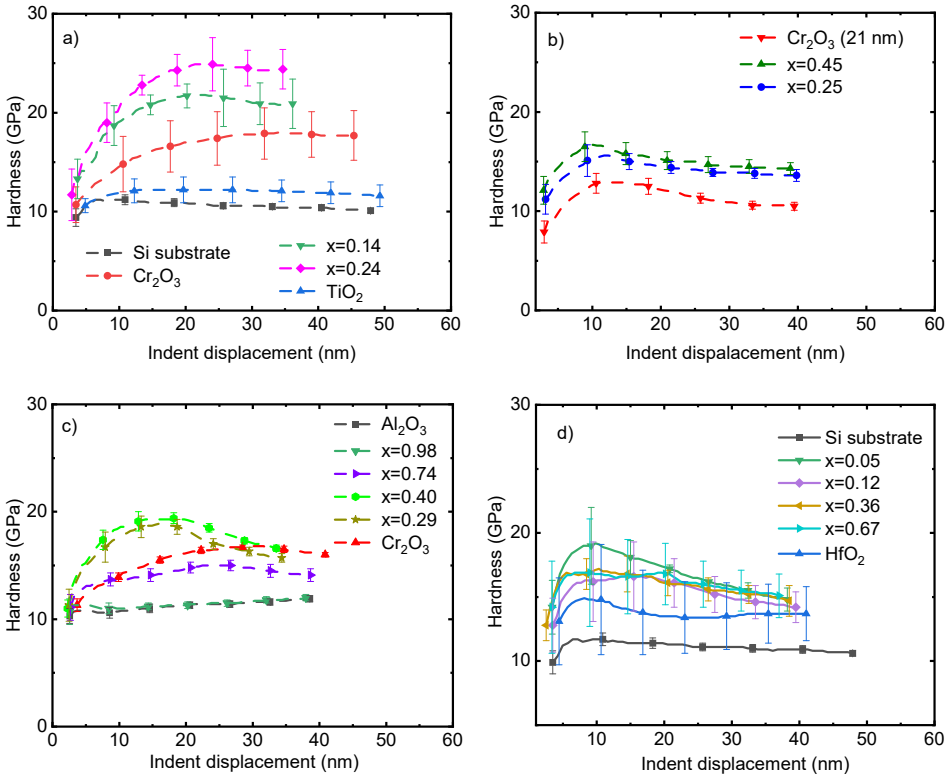

Figure 19. Mean values of hardness in variation of indent displacement for a) CTO deposited by 10 × ($CrCl_2O_2$-CH_3OH) + ($TiCl_4$-H_2O), b) CTO films deposited by k × ($Cr(thd)_3$-O_3) + ($TiCl_4$-O_3) where $k = 15$, and 30, c) CAO and d) CHO films on Si substrate containing different relative concentrations (x).

Crystallite size, crystallinity and phase composition in terms of amorphous and crystalline phase fraction in materials are important properties that are related to mechanical properties [176]. Quantitative estimation of amorphous phase concentration in semicrystalline ultra-thin films is difficult and often not even possible because of the very small volume of diffracting material, various aberrations of the grazing incidence setup, and complicated texture effects. Therefore, for understanding and explaining the changes in the mechanical properties of the films, the crystallinity of the films in this work was characterized using unequivocally estimated parameters like X-ray apparent crystallite size ($<D>_v$) and total index of contrast (*TIC*) that is proportional with total diffraction intensity, being, in turn, proportional to the total volume of crystalline phase.

$<D>_v$ in crystallographic [104] direction of eskolaite in CTO films obtained using 10 × ($CrCl_2O_2$-CH_3OH) + l × ($TiCl_4$-H_2O), showed a considerable decrease from 28 to 7 nm by increasing the Ti/(Ti+Cr) ratio from 0 to 0.24 (Figure 20). This decrease was accompanied by an increase of the hardness of the films (Figure 19 a, and Figure 20). The change in $<D>_v$ was in correlation with change in the relative intensities of diffraction reflections: a decrease in the intensity of 104 reflection and smaller changes for the others (Figure 16 a). These variations

of diffraction intensities were quantitatively also confirmed by decreasing of total index of contrast, *TIC,* about 2 times compared with binary chromium oxide [Figure 5 in [IV]]. The changes in the preferred growth direction from initial polycrystalline towards textured growth in the direction of [001], as the plane of the lowest free energy and simultaneously expectedly also the plane of the highest hardness, could also be the reason why the hardness of the films increased by increasing Ti concentration. Decrease of $<D>_v$ below 30 nm and appearance of preferred orientation support the generally accepted opinion that in materials with small crystallite size ($<D>_v$ < 30 nm), the grain boundary-related and diffusion-dominated mechanisms are mainly responsible for offering remarkably harder materials compared with those where the crystallites are larger, and the dislocation-controlled mechanisms are prevailing [177]. The films on SiO_2 substrate showed similar hardness values to those on Si substrate [IV].

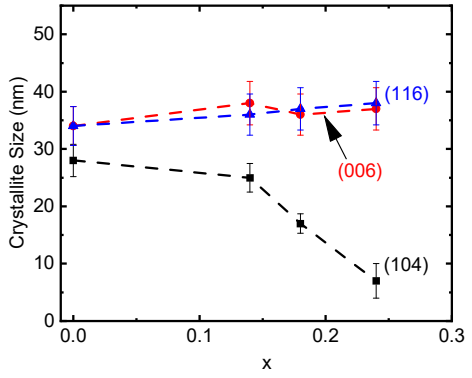

Figure 20. Crystallite size of CTO films deposited by 10 × ($CrCl_2O_2$-CH_3OH) + *l* × ($TiCl_4$-H_2O) process (*l* = 1, 2, 3) in the direction of normal for crystallographic planes (104), (006) and (116) as a function of *x* on Si substrate [IV].

As discussed previously, the hardness of the binary Cr_2O_3 film with ~55 nm deposited by $Cr(thd)_3$-O_3 process was ~14 GPa, while the amorphous aluminum oxide film displayed hardness of ~10.7 GPa. In case of the mechanical behaviour of the CAO films, the presence of nanocrystallites, sized 3–5.5 nm with cubic symmetry in the amorphous matrix (Figure 17) can be the reason for higher mechanical properties compared with binary chromium oxide and aluminum oxide films. Thus, the increase in hardness values of CAO films can be explained by the formation of amorphous/crystalline nanocomposite structure. The formation of nanocrystallite/amorphous composite structure may be the result of higher hardness of CTO thin films deposited from $Cr(thd)_3$ and ozone in combination with $TiCl_4$ and ozone [III]. The presence of amorphous phase among nanocrystallites causes a reduction of dislocation activity in the nanocrystallites. Additionally, the interface between the amorphous and crystalline phases decreases the grain boundary sliding activity. Also, crack propagation blocking in the amorphous phase by the presence of nanocrystallites leads to the hardness increase in the films [178,179]. The increase in hardness of the CAO films can also be attributed to the formation of nanocrystallites with cubic structures. This is supported by

previous reports showing that cubic aluminum oxide films possess hardness comparable to that of the hard corundum structure [119]. Although for the CHO films, the increase in hardness values is not remarkable compared with CTO and CAO films, the ternary films with x-ray amorphous structure did not experienced decrease in hardness values. We assume that a similar mechanism of the formation of nanocrystallite/amorphous composite structure could also cause this behaviour (Figure 19 d).

The Young's elastic modulus (E) of the films followed the same trend as the hardness showed. Figure 21 compares the highest observed E values for ternary films with values of E for binary chromium oxide film at an indent displacement of 10% of the film thickness. The CTO films produced by ALD super-cycle of 10 × ($CrCl_2O_2$-CH_3OH) + ($TiCl_4$-H_2O) showed increase in E from 152 GPa to 205 GPa (at 10 nm indent displacement) by increasing x from zero to 0.24. The elastic modulus of the CAO and CHO ternary films deposited by super-cycles of k × ($Cr(thd)_3$-O_3) + (TMA-O_3) and k × ($Cr(thd)_3$-O_3) + ($HfCl_4$-O_3) showed the maximum modulus of 168 ± 6 GPa, which was higher compared to 151 ± 8 GPa for binary Cr_2O_3 deposited by $Cr(thd)_3$-O_3 process.

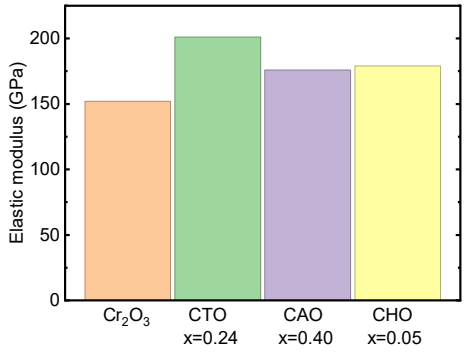

Figure 21. Elastic modulus of binary chromium oxide and ternary films with the highest hardness values at indent displacement of 10% of the film thickness values.

7.5. Wear resistant performance of the ternary films

Resistance of films to elastic deformation (characterized by H/E ratio), but also to plastic deformation and wear (determined from H^3/E^2 ratio) was analyzed in detail by applying wear-resistant measurements in case of CAO and CHO ternary component films. The calculations showed that the ternary films with x in the range displayed all ternary films displayed a higher H^3/E^2 ratio compared with binary oxide films, indicating the higher resistance of ternary films to plastic deformation (Figure 22). To investigate, we applied wear-resistant measurements to binary and some selected ternary films. The variations of wear rate for Cr_2O_3 and Al_2O_3 films and CAO films with x = 0.40 under wear loads of 60, 90, 120, 150 μN were performed (Figure 23 a). Here, the scan size was 3×3 $\mu m^{2,}$ and the wear track area was 2×2 μm^2. The wear rate of the ternary film was considerably lower in comparison with both binary oxide films. The lowest wear rate was

observed for the ternary film with the highest values H^3/E^2 value. The post-wear scanning probe microscope images from the worn surface of the binary and ternary films under 90 µN confirmed the amount of material removal and surface deformation for the binary films. Absence of wear debris from the surface indicated that plastic deformation by abrasive wear was dominant [180], (Figure 12 in [I]). However, the worn surface for the ternary film with x = 0.40 exhibited barely visible deformation, indicating higher wear resistance of the film (Figure 11 and 12 in [I]). The wear rate of the thin ternary chromium aluminum oxide films in this research decreased by about 80%, while in previous research reports, the wear rate reduction in Cr_2O_3-Al_2O_3 composite film by 43.8 % compared with the Cr_2O_3 coating was reported by the addition of 20 wt% of Al_2O_3 [114].

The dependence of wear rate on the number of wear cycles for the load of 90 µN and track dimension of 2 × 2 µm^2 displayed that by increasing the number of wear cycles, the value of the wear rate of both binary oxide and ternary film decreased (Figure. 23. b). Decrease in wear rate by increasing wear cycles in ceramic films may be due to the formation of a tribo-film, consisting of reaction products and fine debris, creating a smooth and relatively soft surface, enhancing lubrication, and reducing wear [181].

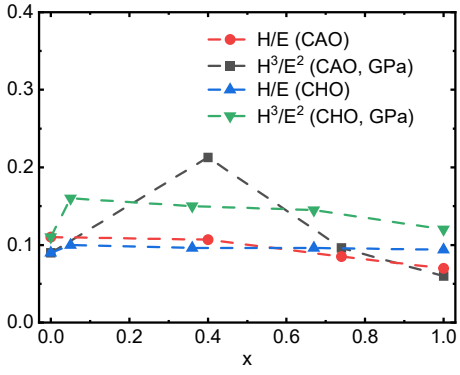

Figure 22. H/E and H^3/E^2 ratios for CAO and CHO films.

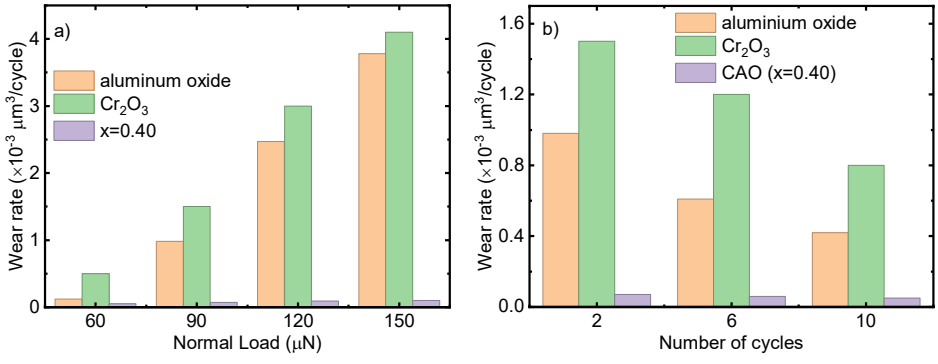

Figure 23. a) the variation of wear rate of the binary and ternary CAO film with x = 0.40 inside the track with area of 2 × 2 µm^2 as a function of indentation load, b) variation of wear rate of the films as a function of the number of wear cycles under a wear load of 90.

The wear profiles of the Cr_2O_3, HfO_2, and ternary Cr-Hf-O films with a scan size of 5×5 μm^2, wear area of 2×2 μm^2 have been displayed in Figure 24 a. The wear depth of the Cr_2O_3 films decreased when Hf was introduced into the film. It can be observed that binary films and the ternary film with $x = 0.05$ showed uniform worn areas in comparison with the worn area of the ternary films with $x = 0.67$. We assume that in these films, wear does not occur by complete removal of material from the area under tip sliding, but rather by material transformation from one side to the other side of the worn area, making the height in the worn area uneven (Figure 24 a and b).

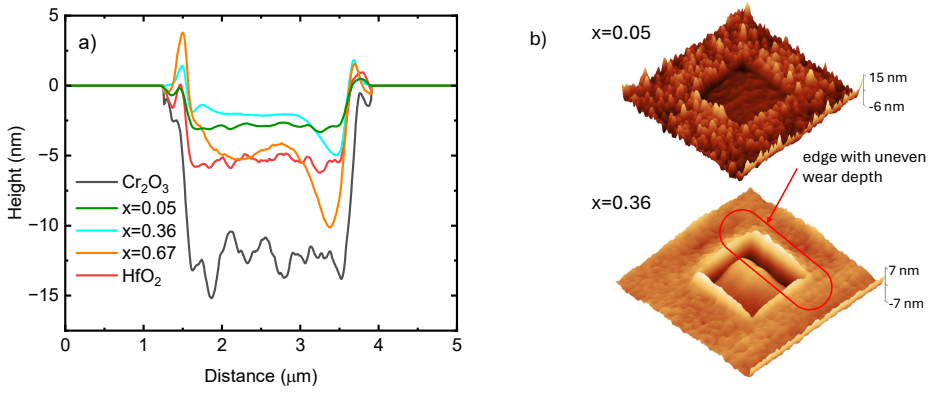

Figure 24. a) wear profile of the binary and ternary chromium hafnium oxide films under a wear load of 150 μN. b) post-wear scanning probe microscope images of two CHO films at the wear track region exhibiting uniform ($x = 0.05$) and nonuniform ($x = 0.36$) worn areas.

The decrease in the wear rate of this film compared with the Cr_2O_3 film, demonstrates that in the ternary films, the higher hardness causes resistance to deformation under the working environment.

7.6. Optical properties of the ternary oxide films

The refractive indices (n) calculated for binary Cr_2O_3 and TiO_2 deposited by $CrCl_2O_2$-CH_3OH, and $TiCl_4$-H_2O ALD processes, respectively, on Si were ~2.53 and ~2.47 at 633 nm, respectively. No remarkable dependence of n on the concentration of Ti was observed for the ternary CTO films deposited using combinations of $CrCl_2O_2$-CH_3OH and $TiCl_4$-H_2O (Figure 25). Also, no remarkable changes in extinction coefficient k were observed by increasing m from 0 to 3 and it was equal to 0.05 at a wavelength of 633 nm, and no big change was observed in the absorbance of these films with different x values. The value of n for the binary Cr_2O_3 film with 21 and 50 nm thickness deposited by $Cr(thd)_3 + O_3$ was 2.35 and 2.28, respectively, at a wavelength of 633 nm. The CTO films with a thickness of 20–22 nm grown from ($Cr(thd)_3$-O_3) + ($TiCl_4$-O_3) showed constant

refractive index value of ~2.42. A decrease of n from 2.2 ± 0.09 to 1.9 ± 0.09 at the same wavelength by increasing x from 0.29 to 0.55 was observed in the ternary CAO films (Figure 25). n at a wavelength of 633 nm changed from in the range of 2.36 to 2.19 in CHO films by variation of x in the range of 0.05 to 0.67 (Figure 25). For the CHO films with x values of 0.05 and 0.12, demonstrating eskolaite phase (Figure 16), the value of n shifts close to the binary Cr_2O_3 film. However, in the CHO film with $x = 0.94$, the value of n was 1.94, which is slightly lower than the refractive index of the pristine HfO_2 film (2.09). This can also be attributed to the structural changes of the films. While binary HfO_2 is crystalline, containing monoclinic phase as a major phase and also tetragonal or cubic phase, the ternary Hf reach film with x = 0.94 contained mostly an X-ray amorphous structure with a very weak peak belonging to the tetragonal (or cubic) phase.

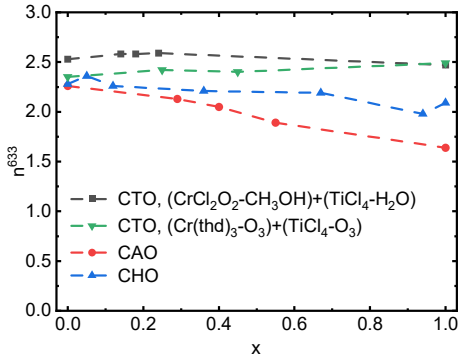

Figure 25. Variation of refractive index values at wavelength of 633 nm, as a function of x for ternary films.

Band gap energy *(E_g)* for binary Cr_2O_3 film deposited by $Cr(thd)_3 + O_3$ with a thickness of 55 nm on Si substrate was ~2.75 (0.1) eV, calculated for indirect transition. The 95 nm thick binary chromium oxide film deposited by $CrO_2Cl_2 + CH_3OH$ showed an indirect transition E_g of 3.0 eV [IV].

In the case of CTO films where $CrO_2Cl_2 + CH_3OH$ was used as Cr-O sources, the indirect E_g exhibited a decrease with the increase of Ti concentration in the film towards the minimum value of E_g ~2.20 eV at $x = 0.24$ [IV]. The main change in E_g was observed between the binary Cr_2O_3 and CTO film with x = 0.14. The additional increase in x did not cause remarkable changes in the E_g (Figure 26 a). The similar behavior in indirect bandgap values of the CTO films deposited by combination of $Cr(thd)_3$-O_3) and ($TiCl_4$-O_3) was observed, where the values of E_g of ~2.0 and ~2.2 eV for the CTO films with $x = 0.25$ and $x = 0.45$ were observed, respectively [III]. The decrease in band gap values by increasing the concentration of the doping element can be related to changes in the average bond energy, which is a function of the composition of films. The reduction of E_g by doping of Cr_2O_3 has been observed previously and explained by the formation of an impurity-like band in the Cr_2O_3 host [103]. For the CAO films, the indirect allowed transition model also showed a decrease from ~2.75 ± 0.1 eV for the Cr_2O_3 film to

~2.65 ± 0.1 eV by increasing x to 0.4. By increasing the value of x to 0.55, E_g shifted to 3.3 eV (Figure 26 b). It was not possible to calculate the E_g value for the Al_2O_3 film and those of ternary CAO films containing high concentrations of Al atoms because Eg values of these films seemed to approach the bandgap energy of alumina (~6.4 eV [182]) that was almost at or just above the maximum spectral limit (ca 5.5 eV) of the used ellipsometer.

Indirect transition band gap energy calculations for CHO films showed that by adding Hf to the Cr_2O_3 film in a relative concentration (x) range of 0.05 to 0.36 did not change the E_g of chromium oxide films considerably, and the value of indirect E_g stayed in the range of ~2.75 to ~2.80 eV (Figure 26 c). The obtained data from this work showed that the optical properties of chromium oxide films can be tailored for different applications, from photovoltaic to semiconducting applications, by forming ternary films.

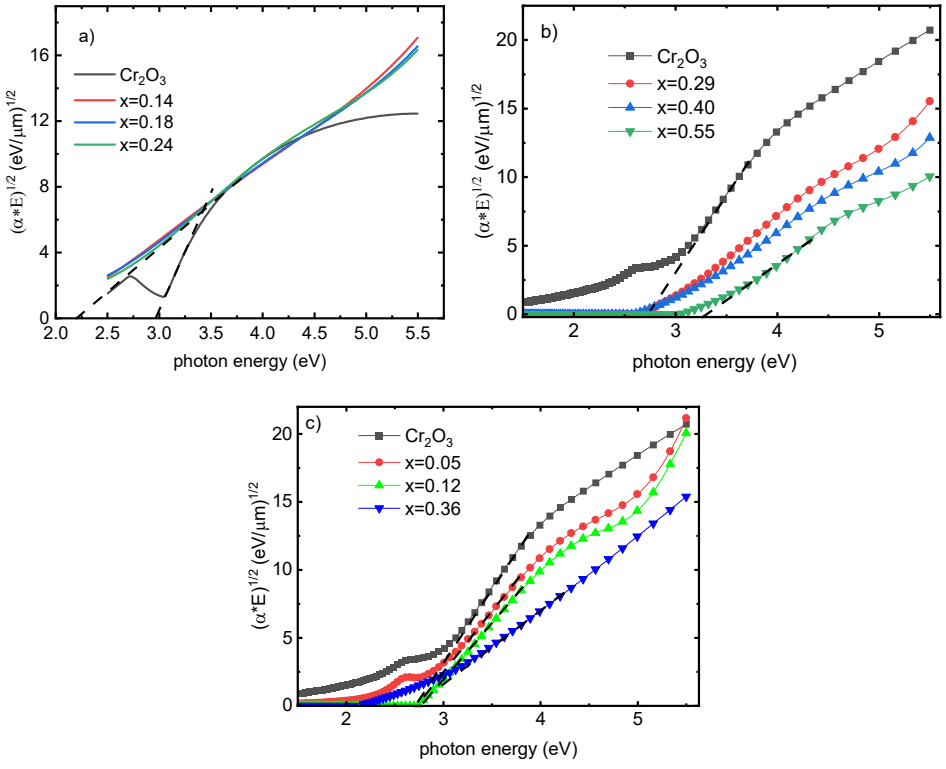

Figure 26. Tauc plots calculated a) CTO films deposited by $k \times (CrO_2Cl_2\text{-}CH_3OH) + (TiCl_4\text{-}H_2O)$ [IV], and b) CAO , c) CHO films with different values of x, using the indirect transition model.

7.7. CAO films on sapphire substrate.

In order to achieve well-crystalline films with precise crystallographic orientation, the ternary chromium aluminum oxide films were deposited on α-Al_2O_3 (001) (c-plane sapphire), which often serves as a substrate for epitaxial growth of thin films. Since chromium oxide can crystallize on sapphire substrate both in the form of trigonal α-Cr_2O_3 or tetragonal CrO_2 structure [183]. the XAS analysis was used to determine the oxidation state of chromium for the films on c-plane sapphire. The Cr 2p spectra data confirmed a stable Cr^{3+} oxidation state with octahedral coordination for all the ternary films (Figure 27), matched well with previously reported absorption spectra of chromium oxide films containing chromium in a stable 3+ oxidation state [184,185].

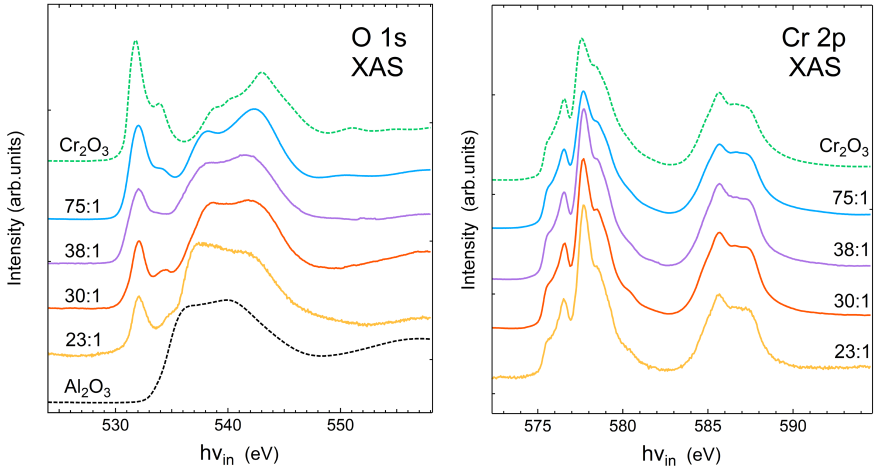

Figure 27. Cr 2p and O 1s edge X-ray absorption spectra of binary chromium oxide, aluminum oxide, and ternary CAO films [V].

According to XRD analysis, the binary aluminum oxide film was amorphous. The phase composition of the ternary $(Cr_{1-x}Al_x)_2O_3$ films was amorphous or crystalline depending on the concentration of Al in the films, which was controlled by the number of Cr-O subcycles in the ALD supercycle k × ($Cr(thd)_3$-O_3) + (TMA-O_3). By increasing the number of k to 23 and above, a crystalline structure appeared. For the film deposited with $k \geq 38$, splitting in the peaks was observed, which can be due to the formation of crystalline domains with slightly different cell parameters due to variations in Al concentration (Figure 28 a).

Epitaxial orientation relation was determined by φ-scan and in-plane measurements for the films deposited by $k = 45$. The φ-scan analysis for the family of {1 0 10} lattice planes revealed three well-defined peaks for both films on c-plane sapphire substrates overlapping at one and the same φ positions, confirming the epitaxial in-plane orientation of the films (Figure 28 b). The in-plane $\theta/2\theta$ scan of the 110 reflection for the same film confirmed the crystalline epitaxial growth of the films, with a hexagonal structure. The epitaxial relations were determined

as (0001) [11–20] film || (0001) [11–20] c-plane Al_2O_3 (Figure 5 in [V]). Results of rocking curve (ω-scan) out-of-plane measurements for 006 reflections for the films on c-plane sapphires enabled the estimation of the structural quality of the films. While the width of the rocking curve ($FWHM_\omega$) for binary Cr_2O_3 film was 0.32°, The minimum value of $FWHM_\omega$ = 0.1° was measured for the films deposited with $38 \leq k \leq 75$ in the ALD, demonstrating better crystal quality in the ternary films compared with binary chromium oxide.

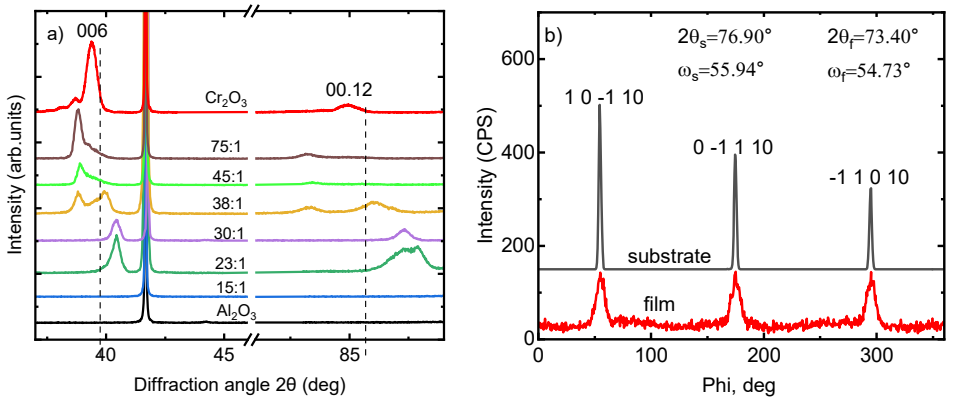

Figure 28. a) XRD patterns of $(Cr_{1-x}Al_x)_2O_3$ films on sapphire. The reflections are labelled by Miller indices. The patterns are identified by the k:1 numbers showing the number of Cr-O subcycles in the ALD supercycle. The dashed lines show the atomic planes of eskolaite from the database (PDF-2 card 38–1479). b) φ scans in asymmetric geometry of the films deposited by 45:1 subcycle ratio.

The indentation analysis demonstrated dependence of both hardness and elastic modulus values, displaying dependency of the mechanical properties of ternary $(Cr_{1-x}Al_x)_2O_3$ films on the composition and microstructure of the films (Figure 29). The highest hardness, about 28 GPa at ID of ~7 nm, was observed for the ternary film deposited by k = 38, which can be related to changes in crystallinity, characterized often by $\langle D \rangle_v$ as discussed previously in this work. Binary Cr_2O_3 on c-plane sapphire contained crystallites sized at 23.2 nm. For the CAO ternary films, crystallites with sizes ranging from 16.5 nm to 24.5 nm were observed. In the film deposited by k = 38, the crystallites with slightly different lattice parameters also exhibited different values of $\langle D \rangle_v$ = 22 nm and $\langle D \rangle_v$ =16.5 nm.

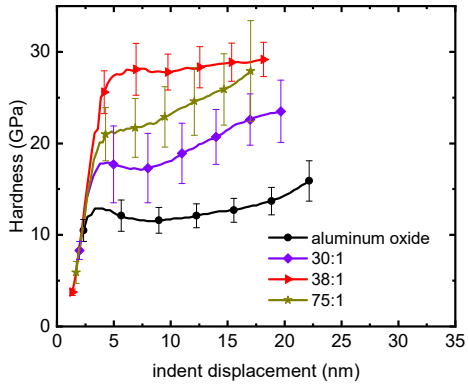

Figure 29. Mean values of hardness of the ternary CAO films on c-plane sapphire at different indentation depths. The ternary films are identified by the *k*:1 numbers showing the number of Cr-O subcycles in the ALD supercycle $k \times (Cr(thd)_3\text{-}O_3) + (TMA\text{-}O_3)$.

The presence of an amorphous phase in the film and formation of a crystalline/ amorphous composite structure was investigated using annealing experiments, since one of the assumptions mentioned previously in relation to the amorphous phase could be one of the reasons for high hardness. To test this hypothesis, the films with high hardness were annealed at 800 °C, and any structural changes were analyzed by HRXRD. The film deposited by $k = 38$ did not show any structural changes after annealing (Figure 30), indicating the absence of a considerable amorphous phase.

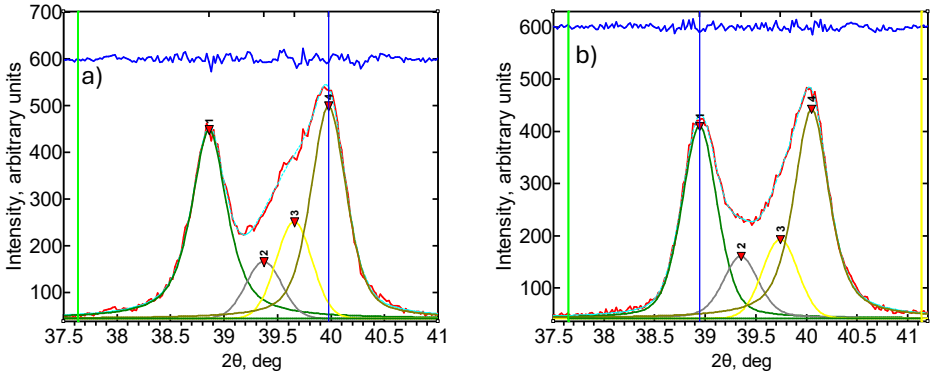

Figure 30. Observed, fitted and difference (offset applied) patterns for selected reflections of a) as-deposited and b) after annealing, for the film deposited by ALD subcycle ratio of *k:l* = 38:1.

7.8. Thermal stability of ternary $(Cr_{1-x}Me_x)_2O_3$ films

Too investigate the structural evaluation of the ternary films and binary chromium oxide film at high temperatures, the selected CAO and CTO films, all deposited using $Cr(thd)_3$ and O_3 as Cr-O source, The remarkable change in *FWHM* value was recorded when the heating temperature exceeded 500 °C (Figure 31 a) and decrease in *FWHM* of about 30% was observed at 600 °C. the structural and materials characteristic change by annealing at 500 °C was reported previously, where after annealing, the edge of absorption moved towards the red range of the wavelength after being annealed at 500 °C [186]. Also, the transformation from amorphous to crystalline chromium oxide film with a hexagonal corundum-type structure has been reported [187]. A decrease in *FWHM* values is as a result of an increase in crystallite size. The increase in crystallite size of the eskolaite phase during annealing can be explained as a result of an increase in diffusivity and mobility of grain boundaries [188]. Ternary CTO containing $x = 0.25$ and $x = 0.45$ and chromium aluminum oxide (CAO) films with a close atomic ratio of Al compared to CTO films showed no structural changes by increasing annealing temperature up to 900 °C (Figure 31. b). The high-temperature structural stability of the ternary films is likely due to their specific elemental composition, which raises the temperatures at which crystallization and recrystallization begin compared with binary chromium oxide films.

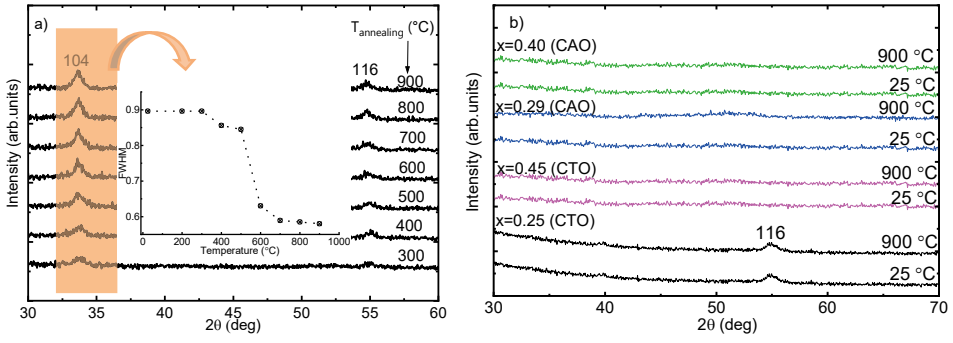

Figure 31. GIXRD patterns of a) binary Cr_2O_3 and b) ternary chromium titanium oxide (CTO) and chromium aluminum oxide (CAO) films with similar atomic ratios at different annealing temperatures. Reflection is denoted by Miller indices corresponding to the eskolaite phase.

The layer structure of the films is important for explaining the behaviour of films in various applications. The initial assumed transition layer thickness for as-deposited films was considered to be 1 nm in modelling. For the binary Cr_2O_3 film, formation of a transition layer with a thickness of 11 nm and a density of 2.8 g/cm^3 was observed at 900 °C [II]. This density was remarkably lower than the density of eskolaite and slightly higher than the density of amorphous SiO_2 (2.2 g/cm^3 [189]), indicating that the major amount of this layer was most probably amorphous with a composition of $(Si_{1-x}Cr_x)O_2$. In the case of CTO films, the

thickness increase of the transition layer was 4 times after annealing at 900 °C, whereas this increase appeared just between 800 and 900 °C. The thickness of transition layer for CAO films did not change remarkably during the annealing, demonstrating that CAO films have the best among the studied types of films oxygen diffusion barrier properties at high temperatures up to 900 °C. This result is supported by previously published results showing better substrate protection by Al_2O_3 coating against oxidation at high temperatures compared with chromium oxide [190]. A slight increase in density of CTO films was observed at an annealing temperature of 700 °C for x = 0.25, changing from 4.7 to 4.9 by increasing the annealing temperature up to 900 °C. No remarkable changes were observed for the density of the CAO film up to 900 °C, confirming the high thermal stability of these films.

CTO film with x = 0.25 exhibited only a slight density increase at 700 °C, rising from 4.7 to 4.9 by 900 °C. In contrast, the CAO film showed no significant density change up to 900 °C, indicating its superior thermal stability (Figure 32 a). At the same time, the main film layer became thinner with increasing annealing temperature, mainly at around 700 °C; the thickness reduction reached approximately 17% for Cr_2O_3, 14% for CTO, and 9% for CAO at 900 °C (Figure 32 b). This thinning is attributed to structural rearrangement, reduced defect density, and especially material loss through evaporation, including the possible formation and volatilization of chromium-containing species. The slight densification of CTO at high temperature is likely related to its greater thickness reduction, which may have led to a more compact film structure [II].

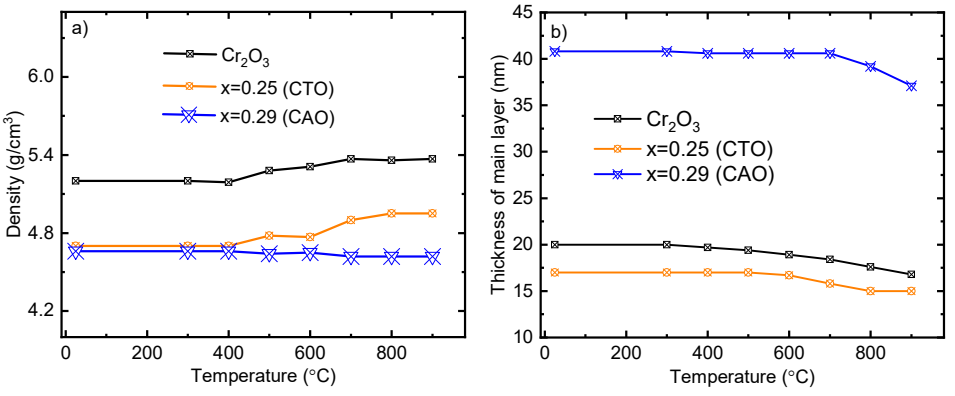

Figure 32. Variations of a) density and b) film thickness values at different annealing temperatures for binary and ternary CTO and CAO films.

8. CONCLUSIONS

Chromium oxide (Cr_2O_3) is a multifunctional ceramic material known for its high hardness, wear resistance, corrosion resistance, as well as its useful optical and electronic properties. This thesis demonstrates that the structural, mechanical, tribological, and optical properties of chromium oxide thin films synthesized by atomic layer deposition (ALD) can be effectively engineered through the formation of ternary compounds with Me = Ti, Al, and Hf elements and by variation of the atomic ratio x = Me/(Me + Cr).

Binary component Cr_2O_3 films were synthesized using a novel $Cr(thd)_3$-O_3 ALD process on silicon substrates. The growth rate of the films increased from 0.032 to approximately 0.105 Å/cycle when the deposition temperature (T_G) increased from 200 °C to 275 °C. Formation of the eskolaite (α-Cr_2O_3) was observed for the films deposited at T_G = 250–300 °C. Films deposited at ≤225 °C were X-ray amorphous. The density of the films characterized by XRR, changed from 4.9 to 5.23 g/cm^3, and the surface roughness from 0.4 nm to 3.4 nm with increasing T_G from 200 to 300 °C.

The formation of ternary Cr-Me-O films introduced substantial structural modifications. In Cr-Ti-O (CTO) films deposited using the super-cycle formula [k × (CrO_2Cl_2 – CH_3OH) + l × ($TiCl_4$ – H_2O)], the eskolaite phase was preserved over a wide composition range, indicating that Ti incorporation (up to ~9 at%) does not disrupt the host lattice but instead introduces lattice defects and modifies crystallinity. A key observation was the significant changes in the nanostructure for the films on Si substrate, where $\langle D \rangle_v$ decreased from approximately 28 nm in binary Cr_2O_3 to about 7 nm with increasing Ti content up to x = 0.24. Similar behavior in decrease in crystallinity of the CTO films deposited by ALD super-cycle of [k × ($Cr(thd)_3$-O_3) + ($TiCl_4$-O_3)] was observed where by increasing the atomic ratio of Ti (Ti/(Ti+Cr) from zero to 0.45, the films phase composition changed from polycrystalline to x-ray amorphous. Cr-Al-O (CAO) films deposited by [k × ($Cr(thd)_3$-O_3) + (TMA-O_3)] on Si substrates exhibited predominantly X-ray amorphous structures using regular GIXRD analysis. However, 14 times slower GIXRD scan revealed the presence of weak and very broad diffraction peaks belong to the face-centered cubic lattice. High-resolution TEM analysis confirmed the presence of nanoscale crystallites (3–5.5 nm) in CAO films with x = 0.40 embedded in an amorphous matrix, forming a nanocomposite structure. A clear dependence of crystallinity and phase composition on the Hf content was found in Cr-Hf-O (CHO) films deposited by [k × ($Cr(thd)_3$-O_3) + ($HfCl_4$-O_3)] on Si substrates, which showed a strong effect of hafnium on lattice stability: at low Hf content ($x \leq 0.12$), the films were crystalline (eskolaite), with further increase they became X-ray amorphous, and at high concentration ($x > 0.9$) crystalline phases (tetrahedral or cubic HfO_2) reappeared.

Although the epitaxial growth of binary α-Cr_2O_3 films on c-plane sapphire substrate was known previously, the appearance of ternary CAO films within a defined compositional window on c-plane sapphire in epitaxial relationship

(0001) $[11–20]_{film}$ || (0001) $[11–20]_{\alpha–Al2O3}$, containing crystalline domains with slightly different cell parameters, was one interesting novel result.

The film density in ternary systems depended on the composition, lying within the range of values for binary oxides, but this dependence was not strictly linear and deviated from a simple mixing rule. This behavior suggested that the actual microstructure, porosity, and degree of crystallinity of the films affect the density in addition to the chemical composition.

Significant improvements were observed in the mechanical properties. While binary Cr_2O_3 film with thickness of 95 nm deposited by $CrCl_2O_2$-CH_3OH exhibited a hardness and elastic modulus of ~15 and ~152 GPa, respectively, the CTO film with $x = 0.24$ and 84 nm of thickness, showed the hardness and elastic modulus of 20.5 GPa, and 205 GPa, respectively, at comparable indentation depth. The CTO thin films obtained by using ALD super-cycle [k× ($Cr(thd)_3 – O_3$) + ($TiCl_4$-O_3)] with thickness in the range of 20–22 nm showed hardness values of 15.2 and 16.7 GPa, while the binary 21 nm thick Cr_2O_3 film showed hardness of ~12.5 GPa. CAO films reached hardness of ~17.5–18.4 GPa at $x = 0.29–0.40$. In CHO films, the maximum hardness of ~19 GPa was achieved at low Hf concentration (Hf/(Hf+Cr) = 0.05), while at higher compositions the values approached those of binary Cr_2O_3. These results clearly demonstrate that the formation of ternary compounds improves hardness by approximately 20–40% relative to binary component chromium oxide films. The origin of this mechanical enhancement lies in microstructural engineering. In CTO films with ALD process of [k × ($CrO_2Cl_2 – CH_3OH$) + l × ($TiCl_4 – H_2O$)], the decrease of $\langle D \rangle_v$ from 28 nm to 7 nm indicates a strong grain-refinement effect, leading to increased hardness through mechanisms similar to Hall–Petch strengthening. Additionally, the coexistence of a nanocrystalline/amorphous composite structure that provides resistance to dislocation motion and crack propagation could be the reason of mechanical property improvement.

The observed increased of H^3/E^2 ratios for ternary CAO and CHO films and nanowear tests performed at loads between 60 and 180 μN revealed that ternary films exhibit improved resistance to plastic deformation, and are significantly more wear resistant compared to binary component Cr_2O_3 film. In particular, CAO films showed up to ~80% reduction in wear rate at $x = 0.40$. This improvement can be attributed to the combined effects of higher hardness, making plastic deformation in the surface difficult. Thus, formation of ternary compound film can be an effective strategy for significantly improving the tribological lifetime of mechanical components coated with these films.

In addition to mechanical and tribological improvements, the optical properties of the films were strongly affected by the ratio of Cr and Me in these thin films. Binary Cr_2O_3 films exhibited refractive indices in the range of 2.26 to 2.53 at 633 nm, depending on the precursors used for deposition, deposition parameters and the phase composition of the films. By tuning composition to a ternary compound, the refractive index of ternary films could be systematically influenced. CTO films [k × ($CrO_2Cl_2 – CH_3OH$) + l × ($TiCl_4 – H_2O$)] showed relatively stable

refractive index values. A decrease of n from 2.2 to 1.9 at wavelength of 633 nm by increasing x from 0.29 to 0.55 was observed in the CAO films.

There were also changes in the optical bandgap width (E_g) depending on the composition of the films. Binary Cr_2O_3 films deposited by $Cr(thd)_3$ in combination with ozone, on silicon substrate showed an indirect band gap of approximately ~2.75 ± 0.1 eV. In CTO films deposited using supercycle [10 × (CrO_2Cl_2+ CH_3OH) + l × ($TiCl_4$-H_2O)], the indirect transition E_g was approximately 2.2 eV. A similar trend was observed for CTO films deposited using ALD super-cycle [k × ($Cr(thd)_3$-O_3) + ($TiCl_4$– O_3)], where the indirect E_g values were approximately 2.0 and 2.2 eV. In CAO films, the indirect E_g was ~2.65 eV when x = 0.29 and 0.40, and increased to ~3.3 eV at x = 0.55. In contrast, CHO films exhibited indirect band gap close to the E_g of binary Cr_2O_3 films (~2.75–2.80 eV) when x varied in the range of 0.05–0.36. These results show that the optical properties of Cr-Me-O ternary films can be tailored to certain limits for applications in both the visible and wider spectral ranges.

One of the most important and novel results is the increase in the phase composition and atomic structure stability of ternary Cr-Me-O films at higher temperatures. While binary Cr_2O_3 films showed phase composition changes already at 500 °C, these changes did not appear in CTO and CAO films when heated to 900 °C. In addition, CAO films proved to be significantly more effective in inhibiting oxygen diffusion than CTO or Cr_2O_3 films. Such an increase in thermal stability and inhibition of oxidation are among the most important properties of the material from the point of view of microcircuits, protective coatings and other technological applications that must operate in a wide temperature range. In summary, the novel results of this work show that the properties of thin films created on the basis of Cr_2O_3 can be purposefully directed using ALD through ternary alloying and composition control and the type of base material. The addition of Ti, Al, and Hf allowed the creation of a material with higher mechanical strength, lower wear, a wider optical application range and significantly higher thermal stability. Therefore, Cr-Me-O thin films are promising materials for protective coatings, optoelectronics, and high-temperature functional coatings.

SUMMARY IN ESTONIAN

Aatomkihtsadestatud kroomi sisaldavate kolmikelemendiliste õhukeste kilede mikrostruktuuri optimeerimine.

Käesolev töö näitas, et kroomoksiidi (Cr_2O_3) õhukeste kilede struktuurilised, mehaanilised, triboloogilised ja optilised omadused muutuvad märgatavalt, kui aatomkihtsadestuse (ALD) abil kasvatada ternaarsed Cr-Me-O ühendid (Me = Ti, Al, Hf), muutes seejuures sobivalt kolmanda elemendi osakaalu (x = Me/(Me+Cr)). Töö tulemused kinnitavad, et koroomoksiidil põhinevate materjalide baasil saab luua funktsionaalseid kattematerjale, mille omadusi saab koostise ja mikrostruktuuri kaudu eesmärgipäraselt disainida.

Uudse $Cr(thd)_3$–O_3 ALD protsessiga räni monokristallile kasvatatud 5–64 nm paksuste Cr_2O_3 kilede kasvukiirus suurenes 0.03 Å/tsükkel kuni 0.105 Å/tsüklini, kui kasvu temperatuuri tõsteti 200 °C-lt 275 °C-ni. Eskolaiidi (α-Cr_2O_3) kristalliline faas moodustus temperatuuridel 250–275 °C, samal ajal kui madalamatel temperatuuridel kasvatatud kiled ei olnud kristallilised. Kasvutemperatuuri tõusuga kaasnes kilede tiheduse suurenemine 4.90 g/cm^3-lt kuni 5.23 g/cm^3-ni ja pinnakareduse kasv 3 nm võrra (0.4 nm kuni 3.4 nm), mis olid hästi korrelatsioonis kilede kristallilisuse muutusega ning viitasid olulistele muutustele kile pinna morfoloogias.

Ternaarsete Cr-Me-O kilede puhul ilmnesid märkimisväärsed nanostruktuursed muutused sõltuvalt kolmanda elemendi lisamise määrast. Räni alustele kasvatatud Cr-Ti-O (CTO) kiledes säilis eskolaiidi trigonaalne faas laias koostisvahemikus, mis näitas, et Ti osakaal kuni ≈9 at% ei põhjusta faasiüleminekut, vaid tekitab pigem võrevigu ja muudab kristallilisust. Ti sisalduse suurenedes alates binaarsest Cr_2O_3 kuni ternaarseni $Cr_{1.76}Ti_{0.24}O_3$ vähenes kristalliitide mõõde neli korda (28→7nm), mis viitas märgatavale nanostruktuursuse suurenemisele.

Cr-Al-O (CAO) kilede puhul, mille koostised olid x = 0.29 and 0.40 ning mis olid kasvatatud Si alusele, tuvastati kuubilise sümmeetriaga nanokristallide olemasolu. Selleks kasutati tavalisest 14 korda aeglasemat GIXRD mõõterežiimi, et parandada signaal-müra suhet ja võimaldada nõrkade difraktsioonimaksimumide eristamist.

Kõrge ruumilise lahutusega TEM analüüs kinnitas väikeste, 3–5.5 nm läbimõõduga, nanokristallide olemasolu põhiliselt amorfses kiles, moodustades nanokomposiitse struktuuri. Lisaks ilmnes selge orientatsiooniefekt safiiralusel kasvatatud kiledel. Kui binaarse Cr_2O_3 kile epiteksiaalne kasv safiiri (001) tasandile oli juba varem teada, siis ternaarsetel CAO kiledel avastati kaksikdomeenne epitaksiaalne kasv teatud koostistel. Saadus tulemus näitas, et koostise kontroll võimaldab mitte üksnes materjali omadusi muuta, vaid ka suunata kile struktuuri moodustumise viisi amorfsest polükristalliseks või epitaksiaalseks.

Cr-Hf-O (CHO) kiledel leiti selge kristallilisuse ja faasilise koostise sõltuvus Hf sisaldusest, mis näitas hafniumi tugevat mõju võre stabiilsusele: väikesel Hf sisaldusel ($x \leq 0.12$) olid kiled kristallilised (eskolaiit), Hf osakaalu suurenemisel

muutusid amorfseks ning suurtel kontsentratsioonidel ($x > 0.9$) ilmusid uuesti kristallilised faasid (tetragonaalne või kuubiline, monokliinne HfO_2).

Kilede tihedus sõltus ternaarsetes süsteemides koostisest, jäädes binaarsete oksiidide tiheduste piirides. Sõltuvus ei olnud siiski rangelt lineaarne vaid kaldus kõrvale lihtsast segamisreeglist. Selline käitumine viitas sellele, et lisaks keemilisele koostisele mõjutavad tihedust ka kile tegelik mikrostruktuur, poorsus ja kristallilisuse aste.

Kõige olulisemad tulemused saadi kilede mehaanilistes omaduste analüüsil. Kui binaarse Cr_2O_3 kile, mille paksus oli 95 nm, kõvadus ja elastsusmoodul ulatusid vastavalt väärtuseni 14.8 GPa ja ≈150 GPa, siis samadel mõõtmistingimustel saavutas CTO kile koostisel $x = 0.24$ ja paksusel 84 nm kõvaduse 20.5 GPa ning elastsusmooduli 205 GPa. CAO kilede puhul suurenes kõvadus väärtuseni 17.5–18.4 GPa koostisvahemikus $x = 0.29 – 0.40$, ning CHO kilede maksimaalne kõvadus 18.6 GPa saadi väikesel Hf sisaldusel $x = 0.05$. Kokkuvõttes näitavad tulemused, et ternaarsetes Cr-Me-O kiledes on võimalik saada kõvaduse suurenemist ligikaudu 20–40% võrra võrreldes binaarsete Cr_2O_3 kiledega. See on seletatav eelkõige muutustega mikrostruktuuris: kristallilisuse vähenemine, nanokristallilise ja amorfse faasi kooseksisteerimine ning nendest tingituna plastilise deformatsiooni ja dislokatsioonide liikuvuse pidurdumine.

Lisaks kinnitasid ka triboloogilised mõõtmised (materjali kulumine hõõrumisel) mehaaniliste omaduste paranemist. Nanokulumise testides koormustel 60–180 μN osutusid ternaarseid elemente sisaldavad kiled oluliselt kulumiskindlamaks, kui see oli puhta Cr_2O_3 kile korral. Eriti silmapaistev oli CAO kilede käitumine, kus kulumiskiirus vähenes kuni ≈80% koostisel $x = 0.40$. See näitab, et ternaarsed CAO oksiidkiled võimaldavad oluliselt pikendada üliõhukeste katete triboloogilist eluiga.

Kilede optiliste omaduste ja koostise vahel leiti mitmeid seoseid. Binaarsete Cr_2O_3 kilede murdumisnäitaja (n) oli 633 nm lainepikkusel vahemikus ~2.26 to 2.53, sõltuvalt paksusest, ALD lähteaine liikidest, faasikoostisest ja tihedusest. Ternaarsetes süsteemides oli n muudetav koostise kaudu: CTO kilede puhul oli muutus väike, CAO kilede korral vähenes n väärtus ligikaudu väärtuselt 2.2 kuni väärtuseni 1.9 koostise suurenedes vahemikus $x = 0.29$ kuni $x = 0.55$. CHO kilede puhul muutus n vahemikus 2.26–2.16, kui x muutus vahemikus 0.05–0.67. Samuti esinesid muutused optilise keelutsoon laiuses (E_g) sõltuvalt kilede koostisest. Binaarsete Cr_2O_3 kilede kaudne keelutsoon oli ligikaudu vahemikus ~2.75–3.0 eV, CTO kilede puhul vähenes E_g väärtuseni ~2.0–2.2 eV. CAO kiledes muutus E_g vahemikus ~2.65–3.3 eV. Hf lisamine ei muutnud kroomoksiidkilede Eg väärtust oluliselt ning Eg väärtus püsis vahemikus ~2.75–2.80 eV, kui x oli vahemikus 0,05–0,36. Need tulemused näitavad, et Cr-Me-O kolmikkomponent kilede optilisi omadusi saab teatud piires sihipäraselt muuta rakendusteks nii nähtavas kui ka laiemas spektraalvahemikus.

Üheks olulisemaks ja uudseks tulemuseks on ternaarsete Cr-Me-O kilede faasilise koostise ja aatomstruktuuri stabiilsuse suurenemine kõrgematel temperatuuridel. Kui binaarne Cr_2O_3 näitas faasilise koostise muutusi juba temperatuuril 500 °C, siis CTO ja CAO kiledesi ei olnud neid muutusi võimalik tuvastada

isegi kuumutamisel temperatuurini 900 °C. Lisaks osutusid CAO kiled hapniku difusiooni oluliselt efektiivsemalt pärssivaks, kui seda olid CTO või Cr_2O_3 kiled. Selline termilise stabiilsuse kasv ja oksüdatsiooni pärssimine on materjali ühed olulisemad omadused kõrgetemperatuursete mikrolülituste, kaitsekatete ja teiste tehnoloogiliste rakenduste seisukohast, mis peavad töötama laias temperatuuride vahemikus.

Kokkuvõttes näitavad selle töö uudsed tulemused, et Cr_2O_3 baasil loodavate õhukeste kilede omadusi saab ALD abil eesmärgipäraselt suunata ternaarse legeerimise ja koostise kontrolli ning alusmaterjali valiku kaudu. Ti, Al ja Hf lisamine võimaldas luua materjali, millel on suurem mehaaniline vastupidavus, väiksem kulumine, laiem optiline rakendusvaldkond ning oluliselt suurem termiline stabiilsus. Seetõttu on Cr-Me-O õhukesed kiled paljulubavad materjalid kaitsekatete, optoelektroonika ja kõrgetemperatuuriliste funktsionaalsete pinnakatete jaoks.

ACKNOWLEDGEMENTS

Writing these acknowledgements marks the final step of my Ph.D. journey. As I reflect on these years, I realize how fortunate I have been to meet and work with so many wonderful people whose support, guidance, and encouragement made this achievement possible. Although it is impossible to fully express my gratitude to everyone who has been part of this journey, I would like to take this opportunity to acknowledge those who have had the greatest impact on my academic and personal life.

First and foremost, I would like to express my deepest gratitude to my supervisors, Dr. Hugo Mändar, Dr. Lauri Aarik, and Dr. Taivo Jõgiaas, for their invaluable guidance, continuous support, patience, and encouragement throughout my doctoral studies. Their scientific expertise and insightful discussions have played a fundamental role in shaping this research and my development as a researcher. I am grateful to Dr. Aarne Kasikov for his training and assistance in the measurement and analysis of the optical properties of thin films. I appreciate all the support and guidance that I have received from all people at the Laboratory of Thin Film Technology and the Institute of Physics, and their help in carrying out my research work. I would like to thank Prof. Kaupo Kukli, the head of the Laboratory of Thin Film Technology. I am thankful to Dr. Harry Alles for the financial support of my last year of Ph.D.

During my doctoral studies, I had the privilege of collaborating with several leading research groups and laboratories in the fields of Materials Science, particularly thin film technology. These collaborations greatly enriched my research experience and broadened my scientific perspective. I would like to express my sincere gratitude to Dr. Tanel Käämbre and Dr. Rainer Pärna from our neighboring laboratory for their invaluable assistance and expertise in XAS and XPS analyses. My heartfelt thanks go to Prof. Karine Mougin and Dr. Loïc Vidal at the University of Haute-Alsace, France, for their warm hospitality, generous support, and the opportunity to collaborate with their research group. I am also deeply grateful to Prof. Juris Purans, Prof. Smagul Karazhanov, Dr. Timurs Safiulins, Dr. Boris Polyakov, and Dr. Martinš Zubkins, at the Institute of Solid-State Physics, University of Latvia, where I had the opportunity to expand my knowledge and expertise in the field of chromogenic thin film technology. I would like to extend my sincere appreciation to Prof. Maarit Karppinen at the Aalto University, Finland, not only for kindly hosting my research visit and providing access to her laboratory, but also for her support in writing postdoctoral grants for the near future after my Ph.D. defense. I would like to thank Dr. Ramin Ghiyasi and Juha Linjala at Aalto University for their guidance, technical support, and willingness to share their knowledge throughout my visit.

Moving to Estonia, a new country far away from my family and lifelong friends, was one of the greatest challenges of my life. This journey would not have been possible without the wonderful friends I met along the way. I feel incredibly fortunate to have built such meaningful friendships during these five years. To all

my friends, thank you for your kindness, support, and for sharing countless moments with me. You made me feel that I was surrounded by a second family.

Now this part is for my wonderful family: my dear parents and parents-in-law, and my lovely siblings. This achievement would not have been possible without your endless love and support. The hardest part of these years was being far away from all of you. Despite the distance, your encouragement and unwavering belief in me gave me the strength to keep going. I am deeply grateful not only for your support throughout my doctoral studies but for the love, guidance, and sacrifices you have given me throughout my entire life. I would also like to dedicate a special mention to my wonderful nephews: Amir, Matin, Hadi, Armin, and Ata. I hope seeing their names in these acknowledgements brings a smile to their faces and inspires them to dream big, pursue their own ambitions, and always believe in themselves.

Elyad, this part is especially for you. We started this journey together, and throughout these years, you stood by my side through every challenge, always offering your support, encouragement, and belief in me. Your patience, kindness, and constant presence made even the most difficult moments feel manageable. Thank you for being my source of strength and for making this journey not only easier but also truly enjoyable.

REFERENCES

[1] M. Mohammadtaheri, Y. Li, Q. Yang, Hard Cr_2O_3 coatings on SS316L substrates prepared by reactive magnetron sputtering technique: a potential candidate for orthopedic implants, Environ Sci Pollut Res 28 (2021) 25146–25154. https://doi.org/10.1007/s11356-019-05006-3.

[2] A.L. Ji, W. Wang, G.H. Song, Q.M. Wang, C. Sun, L.S. Wen, Microstructures and mechanical properties of chromium oxide films by arc ion plating, Materials Letters 58 (2004) 1993–1998. https://doi.org/10.1016/j.matlet.2003.12.029.

[3] K. Huang, L. Li, L. Wang, G. Li, Y. Xu, Effect of DC bias and RF self-bias on the structure and properties of chromium oxide coatings prepared by vacuum cathodic arc deposition, Vacuum 164 (2019) 325–331. https://doi.org/10.1016/j.vacuum.2019.03.024.

[4] R.C. Ku, W.L. Winterbottom, Electrical conductivity in sputter-deposited chromium oxide coatings, Thin Solid Films 127 (1985) 241–256. https://doi.org/10.1016/0040-6090(85)90195-6.

[5] C.-S. Cheng, H. Gomi, H. Sakata, Electrical and Optical Properties of Cr_2O_3 Films Prepared by Chemical Vapour Deposition, Phys. Stat. Sol. (a) 155 (1996) 417–425. https://doi.org/10.1002/pssa.2211550215.

[6] P. Borisov, A. Hochstrat, V.V. Shvartsman, W. Kleemann, P.M. Hauck, Magnetoelectric Cr_2O_3 for spintronic applications, Integrated Ferroelectrics 99 (2008) 69–76. https://doi.org/10.1080/10584580802107700.

[7] T. Larbi, B. Ouni, A. Gantassi, K. Doll, M. Amlouk, T. Manoubi, Structural, optical and vibrational properties of Cr_2O_3 with ferromagnetic and antiferromagnetic order: A combined experimental and density functional theory study, Journal of Magnetism and Magnetic Materials 444 (2017) 16–22. https://doi.org/10.1016/j.jmmm.2017.07.103.

[8] P. Makushko, T. Kosub, O.V. Pylypovskyi, N. Hedrich, J. Li, A. Pashkin, S. Avdoshenko, R. Hübner, F. Ganss, D. Wolf, A. Lubk, M.O. Liedke, M. Butterling, A. Wagner, K. Wagner, B.J. Shields, P. Lehmann, I. Veremchuk, J. Fassbender, P. Maletinsky, D. Makarov, Flexomagnetism and vertically graded Néel temperature of antiferromagnetic Cr_2O_3 thin films, Nat Commun 13 (2022) 6745. https://doi.org/10.1038/s41467-022-34233-5.

[9] M. Hafeez, A. Siddique Saleemi, S. Ur Rehman, M. Adrees, S. Mehmood, I.A. Mir, L. Zhu, CVD growth of layered Cr_2O_3 hexagonal flakes for optoelectronic applications, Applied Surface Science 536 (2021) 147713. https://doi.org/10.1016/j.apsusc.2020.147713.

[10] S. Ye, Magnetoelectric switching energy of antiferromagnetic Cr_2O_3 used for spintronic logic devices and memory, Physica Rapid Research Letters 16 (2022) 2100396. https://doi.org/10.1002/pssr.202100396.

[11] S.G. Kaleel, M.H. Suhail, H. Kamil, Effect of thermal annealing on the electrical properties and gas sensing for pulsed laser deposition Cr_2O_3 Thin Films, Journal of Physics: Conference Series. 1829 (2021) 012020. https://doi.org/10.1088/1742-6596/1829/1/012020.

[12] M.D. Bijker, J.J.J. Bastiaens, E.A. Draaisma, L.A.M. de Jong, E. Sourty, S.O. Saied, J.L. Sullivan, The development of a thin Cr_2O_3 wear protective coating for the advanced digital recording system, Tribology International 36 (2003) 227–233. https://doi.org/10.1016/S0301-679X(02)00191-3.

[13] Y. Wu, D. He, S. Li, X. Liu, S. Wang, L. Jiang, Deuterium permeation properties of Y2O3/Cr2O3 composite coating prepared by MOCVD on 316L stainless steel, International Journal of Hydrogen Energy 41 (2016) 7425–7430. https://doi.org/10.1016/j.ijhydene.2016.03.132.

[14] D. He, S. Li, X. Liu, C. Zhang, Q. Yu, S. Wang, L. Jiang, Preparation of Cr_2O_3 film by MOCVD as hydrogen permeation barrier, Fusion Engineering and Design 89 (2014) 35–39. https://doi.org/10.1016/j.fusengdes.2013.11.005.

[15] B. Bhushan, G.S.A.M. Theunissen, X. Li, Tribological studies of chromium oxide films for magnetic recording applications, Thin Solid Films 311 (1997) 67–80. https://doi.org/10.1016/S0040-6090(97)00453-7.

[16] M. Ishtiaq, D. Ali, R. Ahmad, I. Muneer, T.M. Khan, Tuning optical and electrical characteristics through Cu doping in spray pyrolysis fabricated Cr_2O_3 thin films, Optical Materials 148 (2024) 114930. https://doi.org/10.1016/j.optmat.2024.114930.

[17] J. Singh, V. Verma, R. Kumar, Preparation and structural, optical studies of Al substituted chromium oxide (Cr_2O_3) nanoparticles, Vacuum 159 (2019) 282–286. https://doi.org/10.1016/j.vacuum.2018.09.033.

[18] A. Zekaik, H. Benhebal, B. Benrabah, Synthesis and characterization of Cu doped chromium oxide (Cr_2O_3) thin films, High Temperature Materials and Processes 38 (2019) 806–812. https://doi.org/10.1515/htmp-2019-0037.

[19] E. Arca, K. Fleischer, I.V. Shvets, Magnesium, nitrogen codoped Cr_2O_3: A p-type transparent conducting oxide, Applied Physics Letters 99 (2011) 111910. https://doi.org/10.1063/1.3638461.

[20] M. Mohammadtaheri, Y. Li, J. Corona-Gomez, Q. Yang, An investigation on synthesis and characterization of superhard Cr-Zr-O coatings, Surface and Coatings Technology 375 (2019) 694–700. https://doi.org/10.1016/j.surfcoat.2019.06.102.

[21] A. Bahrami, A. Delgado, C. Onofre, S. Muhl, S.E. Rodil, Structure, mechanical properties and corrosion resistance of amorphous Ti-Cr-O coatings, Surface and Coatings Technology 374 (2019) 690–699. https://doi.org/10.1016/j.surfcoat.2019.06.061.

[22] N.-E. Laadel, M. El Mansori, N. Kang, S. Marlin, Y. Boussant-Roux, Permeation barriers for hydrogen embrittlement prevention in metals – A review on mechanisms, materials suitability and efficiency, International Journal of Hydrogen Energy 47 (2022) 32707–32731. https://doi.org/10.1016/j.ijhydene.2022.07.164.

[23] A.J.M. Mackus, J.R. Schneider, C. MacIsaac, J.G. Baker, S.F. Bent, Synthesis of doped, ternary, and quaternary materials by atomic layer deposition: a review, Chemistry of Materials 31 (2019) 1142–1183. https://doi.org/10.1021/acs.chemmater.8b02878.

[24] K. Lahtinen, P. Maydannik, P. Johansson, T. Kääriäinen, D.C. Cameron, J. Kuusipalo, Utilisation of continuous atomic layer deposition process for barrier enhancement of extrusion-coated paper, Surface and Coatings Technology 205 (2011) 3916–3922.
https://doi.org/10.1016/j.surfcoat.2011.02.009.

[25] M. Leskelä, M. Ritala, Atomic layer deposition (ALD): from precursors to thin film structures, Thin Solid Films 409 (2002) 138–146.
https://doi.org/10.1016/S0040-6090(02)00117-7.

[26] H. Xu, M.K. Akbari, S. Kumar, F. Verpoort, S. Zhuiykov, Atomic layer deposition – state-of-the-art approach to nanoscale hetero-interfacial engineering of chemical sensors electrodes: A review, Sensors and Actuators B: Chemical 331 (2021) 129403.
https://doi.org/10.1016/j.snb.2020.129403.

[27] A. Tarre, J. Aarik, H. Mändar, A. Niilisk, R. Pärna, R. Rammula, T. Uustare, A. Rosental, V. Sammelselg, Atomic layer deposition of Cr_2O_3 thin films: Effect of crystallization on growth and properties, Applied Surface Science 254 (2008) 5149–5156.
https://doi.org/10.1016/j.apsusc.2008.02.016.

[28] L. Aarik, H. Mändar, P. Ritslaid, A. Tarre, J. Kozlova, J. Aarik, Low-Temperature Atomic Layer Deposition of α-Al_2O_3 Thin Films, Crystal Growth & Design 21 (2021) 4220–4229.
https://doi.org/10.1021/acs.cgd.1c00471.

[29] E. Vaiopoulou, P. Gikas, Regulations for chromium emissions to the aquatic environment in Europe and elsewhere, Chemosphere 254 (2020) 126876.
https://doi.org/10.1016/j.chemosphere.2020.126876.

[30] S. Sakthinathan, G.A. Meenakshi, S. Vinothini, C.-L. Yu, C.-L. Chen, T.-W. Chiu, N. Vittayakorn, A Review of Thin-Film Growth, Properties, Applications, and Future Prospects, Processes 13 (2025) 587.
https://doi.org/10.3390/pr13020587.

[31] H.K. Raut, V.A. Ganesh, A.S. Nair, S. Ramakrishna, Anti-reflective coatings: A critical, in-depth review, Energy and Environmental Science 4 (2011) 3779.
https://doi.org/10.1039/c1ee01297e.

[32] S.J. McDonnell, R.M. Wallace, Atomically-thin layered films for device applications based upon 2D TMDC materials, Thin Solid Films 616 (2016) 482–501.
https://doi.org/10.1016/j.tsf.2016.08.068.

[33] N. Kaiser, Review of the fundamentals of thin-film growth, Applied Optics 41 (2002) 3053.
https://doi.org/10.1364/AO.41.003053.

[34] K. Zweibel, Past, present, future, Progress in Photovoltaics 3 (1995) 279–293.
https://doi.org/10.1002/pip.4670030503.

[35] P.H. Lissberger, Optical applications of dielectric thin films, Reports on Progress in Physics 33 (1970) 197–268.
https://doi.org/10.1088/0034-4885/33/1/305.

[36] M.M. Sabzehmeidani, S. Gafari, S. jamali, M. Kazemzad, Concepts, fabrication and applications of MOF thin films in optoelectronics: A review, Applied Materials Today 38 (2024) 102153.
https://doi.org/10.1016/j.apmt.2024.102153.

[37] H. Baqiah, N. Zhang, M.M. Awang Kechik, N. Mohammed Al-Hada, S. Kiong Tiong, A.A. Al-Zahrani, J. Liu, Q. Li, S. Xu, Crystal growth, optical, photoluminescence and magnetic properties of sol-gel $GdFeO_3$ thin film, Ceramics International 50 (2024) 13892–13900. https://doi.org/10.1016/j.ceramint.2024.01.305.
[38] I.H. Lee, Y.G. Khim, J. Eom, J.Y. Kee, B.K. Choi, H.J. Kim, R. Kim, M.Y. Jung, K.J. Lee, Y. Kim, W.-S. Noh, B. Lee, H. Suh, H.J. Chang, S.O. Won, C. Jang, H. Ryu, D.R. Lee, S.H. Chang, H.H. Lee, Y.J. Chang, J.W. Choi, Controlling the magnetic properties of layered Cr2Te3 thin films via ex-situ annealing, Applied Surface Science 648 (2024) 159057. https://doi.org/10.1016/j.apsusc.2023.159057.
[39] E.H. Rhoderick, Electrical properties of thin films, British Journal of Applied Physics 15 (1964). https://doi.org/10.1088/0508-3443/15/6/301.
[40] H.-J. Kwon, Applications of thin films in microelectronics, Electronics 11 (2022) 931. https://doi.org/10.3390/electronics11060931.
[41] K.D. Harris, D. Vick, E.J. Gonzalez, T. Smy, K. Robbie, M.J. Brett, Porous thin films for thermal barrier coatings, Surface and Coatings Technology 138 (2001) 185–191. https://doi.org/10.1016/S0257-8972(00)01155-5.
[42] J.R.V. Garcia, T. Goto, Thermal barrier coatings produced by chemical vapor deposition, Science and Technology of Advanced Materials 4 (2003) 397–402. https://doi.org/10.1016/S1468-6996(03)00048-2.
[43] A.G. Evans, D.R. Mumm, J.W. Hutchinson, G.H. Meier, F.S. Pettit, mechanisms controlling the durability of thermal barrier coatings, Progress in Materials Science 46 (2001) 505–553. https://doi.org/10.1016/S0079-6425(00)00020-7.
[44] S. Zhang, J. Wang, R. Wu, L. Liu, B. Pan, C. Liu, Structural and corrosion resistance properties of sputtered zirconium nitride thin films as electrode material for supercapacitor, Journal of Alloys and Compounds 900 (2022) 163506. https://doi.org/10.1016/j.jallcom.2021.163506.
[45] C. Mackin, A. Fasoli, M. Xue, Y. Lin, A. Adebiyi, L. Bozano, T. Palacios, Chemical sensor systems based on 2D and thin film materials, 2D Mater. 7 (2020) 022002. https://doi.org/10.1088/2053-1583/ab6e88.
[46] A. Moumen, G.C.W. Kumarage, E. Comini, P-Type metal oxide semiconductor thin films: synthesis and chemical sensor applications, Sensors 22 (2022) 1359. https://doi.org/10.3390/s22041359.
[47] G. Dai, A study of the sensing properties of thin film sensor to trimethylamine, Sensors and Actuators B: Chemical 53 (1998) 8–12. https://doi.org/10.1016/S0925-4005(98)00286-X.
[48] W.D. Nix, Mechanical properties of thin films, Metallurgical and Materials Transactions A 20A (1989) 2217. https://doi.org/10.1007/BF02666659.
[49] M. Salari Mehr, A. Akbari, E. Damerchi, Electrodeposited Ni-B/SiC micro- and nano-composite coatings: A comparative study, Journal of Alloys and Compounds 782 (2019) 477–487. https://doi.org/10.1016/j.jallcom.2018.12.184.

[50] P. Arunkumar, S.K. Kuanr, K.S. Babu, Thin Film: Deposition, growth aspects, and characterization, In: S. Babu Krishna Moorthy, editor. Thin Film Structures in Energy Applications, Springer International Publishing, Cham, 2015: pp. 1–49. https://doi.org/10.1007/978-3-319-14774-1_1.

[51] N. Wint, D.J. Warren, A.C.A. DeVooys, H.N. McMurray, The use of chromium and chromium (III) oxide PVD coatings to resist the corrosion driven coating delamination of organically coated packaging steel, Journal of Electrochemical Society 167 (2020) 141506. https://doi.org/10.1149/1945-7111/abc360.

[52] X. Li, T. Yao, Y. Jiang, A. Tao, X. Yan, Z. Yang, H. Ye, C. Chen, Microstructure and hardness of Cr_2O_3 films grown by pulsed laser deposition, Thin Solid Films 825 (2025) 140749. https://doi.org/10.1016/j.tsf.2025.140749.

[53] A. Stierle, H. Zabel, Kinetics of Cr_2O_3 growth during the oxidation of Cr(110), Europhysics Letters 37 (1997) 365–370. https://doi.org/10.1209/epl/i1997-00158-3.

[54] X.S. Du, S. Hak, T. Hibma, O.C. Rogojanu, B. Struth, X-rays diffraction on a new chromium oxide single-crystal thin film prepared by molecular beam epitaxy, Journal of Crystal Growth 293 (2006) 228–232. https://doi.org/10.1016/j.jcrysgro.2006.05.013.

[55] H. Ekinci, M. Soltani, N.M.S. Jahed, X. Zhu, B. Cui, D. Pushin, Effect of annealing on the structural, optical and surface properties of chromium oxide (Cr_2O_3) thin films deposited by e-beam evaporation for plasma etching applications, Journal of Alloys and Compounds 875 (2021) 160087. https://doi.org/10.1016/j.jallcom.2021.160087.

[56] M. Julkarnain, J. Hossain, K.S. Sharif, K.A. Khan, Optical properties of thermally evaporated Cr_2O_3 thin films, Canadian Journal on Chemical Engineering and Technology 3 (2012) 81-85.

[57] M. Zhu, F. Li, G. Zhou, X. Jin, X. Wang, L. Wang, F. Song, Microstructures and electrical properties of nanostructured Cr_2O_3 thin films deposited by dual-target reactive high-power impulse magnetron sputtering, Vacuum 164 (2019) 293–299. https://doi.org/10.1016/j.vacuum.2019.03.035.

[58] D.-Y. Wang, J.-H. Lin, W.-Y. Ho, Study on chromium oxide synthesized by unbalanced magnetron sputtering, Thin Solid Films 332 (1998) 295–299. https://doi.org/10.1016/S0040-6090(98)01266-8.

[59] Y. Yin, Y. Pan, L.X. Hang, D.R. McKenzie, M.M.M. Bilek, Direct current reactive sputtering Cr–Cr_2O_3 cermet solar selective surfaces for solar hot water applications, Thin Solid Films 517 (2009) 1601–1606. https://doi.org/10.1016/j.tsf.2008.09.082.

[60] S.-Y. Jeong, J.-B. Lee, H. Na, T.-Y. Seong, Epitaxial growth of Cr_2O_3 thin film on Al_2O_3 (0001) substrate by radio frequency magnetron sputtering combined with rapid-thermal annealing, Thin Solid Films 518 (2010) 4813–4816. https://doi.org/10.1016/j.tsf.2010.01.046.

[61] M. Witthaut, R. Cremer, K. Reichert, D. Neuschütz, Preparation of Cr_2O_3 -Al_2O_3 solid solutions by reactive magnetron sputtering, Microchimica Acta 133 (2000) 191–196. https://doi.org/10.1007/s006040070092.

[62] P.M. Sousa, A.J. Silvestre, O. Conde, Cr_2O_3 thin films grown at room temperature by low pressure laser chemical vapour deposition, Thin Solid Films 519 (2011) 3653–3657. https://doi.org/10.1016/j.tsf.2011.01.382.

[63] J. Wang, A. Gupta, T.M. Klein, Plasma enhanced chemical vapor deposition of Cr_2O_3 thin films using chromium hexacarbonyl ($Cr(CO)_6$) precursor, Thin Solid Films 516 (2008) 7366–7372. https://doi.org/10.1016/j.tsf.2008.02.027.

[64] G. Carta, M. Natali, G. Rossetto, P. Zanella, G. Salmaso, S. Restello, V. Rigato, S. Kaciulis, A. Mezzi, A comparative study of Cr_2O_3 thin films obtained by MOCVD using three different precursors, Chemical Vapour Deposition 11 (2005) 375–380. https://doi.org/10.1002/cvde.200406360.

[65] P.M. Sousa, A.J. Silvestre, N. Popovici, O. Conde, Morphological and structural characterization of CrO_2/Cr_2O_3 films grown by Laser-CVD, Applied Surface Science 247 (2005) 423–428. https://doi.org/10.1016/j.apsusc.2005.01.061.

[66] T. Jõgiaas, A. Tarre, H. Mändar, J. Kozlova, A. Tamm, Nanoindentation of chromium oxide possessing superior hardness among atomic-layer-deposited oxides, Nanomaterials 12 (2021) 82. https://doi.org/10.3390/nano12010082.

[67] B. Mandol, N. Mahuli, K. Ohno, L. Scudder, S.K. Sarkar, Atomic layer deposition of chromium oxide—An interplay between deposition and etching, Journal of Vacuum Science & Technology A 39 (2021) 032414. https://doi.org/10.1116/6.0000896.

[68] Y. Liu, D.Y. Chen, Protective coatings for Cr_2O_3-forming interconnects of solid oxide fuel cells, International Journal of Hydrogen Energy 34 (2009) 9220–9226. https://doi.org/10.1016/j.ijhydene.2009.09.022.

[69] A. Afzal, S. Atiq, M. Saleem, S.M. Ramay, S. Naseem, S.A. Siddiqi, Structural and magnetic phase transition of sol–gel-synthesized Cr_2O_3 and $MnCr_2O_4$ nanoparticles, Journal of Sol-Gel Science and Technology 80 (2016) 96–102. https://doi.org/10.1007/s10971-016-4066-4.

[70] M.G. Tsegay, H.G. Gebretinsae, G.G. Welegergs, Sh. Azizi, M.P. Seopela, M. Henini, M. Maaza, Z.Y. Nuru, Optical response of green synthesized thin Cr_2O_3 films prepared via drop and spin coatings, Materials Today: Proceedings (2023). https://doi.org/10.1016/j.matpr.2023.06.225.

[71] Z. Pei, H. Xu, Y. Zhang, Preparation of Cr_2O_3 nanoparticles via C_2H_5OH hydrothermal reduction, Journal of Alloys and Compounds 468 (2009) L5–L8. https://doi.org/10.1016/j.jallcom.2007.12.086.

[72] S. Bhadauria, S. Saxena, R. Prasad, P. Sharma, R. Prasad, R. Dwivedi, Synthesis of ethylene carbonate from cyclocondensation of ethylene glycol and urea over $ZnO•Cr_2O_3$ catalyst system controlled by co-precipitation method, European Journal of Chemistry 3 (2012) 235–240. https://doi.org/10.5155/eurjchem.3.2.235-240.460.

[73] K.K. Kar, ed., Handbook of Nanocomposite Supercapacitor Materials I: Characteristics, Springer International Publishing, Cham, 2020. https://doi.org/10.1007/978-3-030-43009-2.

[74] A. Mittal, G.J. Albertsson, G.S. Gupta, S. Seetharaman, S. Subramanian, Some thermodynamic aspects of the oxides of chromium, Metallurgical and Materials Transactions B 45 (2014) 338–344. https://doi.org/10.1007/s11663-014-0027-x.

[75] R. Vidya, P. Ravindran, A. Kjekshus, H. Fjellvåg, Crystal and electronic structures of Cr_3O_8 and Li Cr_3O_8: Probable cathode materials in Li batteries, Physical Review B 73 (2006) 235113. https://doi.org/10.1103/PhysRevB.73.235113.

[76] H. Sawada, Residual electron density study of chromium sesquioxide by crystal structure and scattering factor refinement, Materials Research Bulletin 29 (1994) 239–245.
https://doi.org/10.1016/0025-5408(94)90019-1.
[77] K. Momma, F. Izumi, VESTA: a three-dimensional visualization system for electronic and structural analysis, Journal of Applied Crystallography 41 (2008) 653–658.
https://doi.org/10.1107/S0021889808012016.
[78] V. Sammelselg, I. Netšipailo, A. Aidla, A. Tarre, L. Aarik, J. Asari, P. Ritslaid, J. Aarik, Chemical resistance of thin film materials based on metal oxides grown by atomic layer deposition, Thin Solid Films 542 (2013) 219–224.
https://doi.org/10.1016/j.tsf.2013.06.079.
[79] P. Almodóvar, F. Santos, J. González, J. Ramírez-Castellanos, J.M. González-Calbet, C. Díaz-Guerra, A.J. Fernández Romero, Study of Cr_2O_3 nanoparticles supported on carbonaceous materials as catalysts for O_2 reduction reaction, Journal of Electroanalytical Chemistry 895 (2021) 115441.
https://doi.org/10.1016/j.jelechem.2021.115441.
[80] T.R. McGuire, E.J. Scott, F.H. Grannis, Antiferromagnetism in a Cr_2O_3 Crystal, Physical Review 102 (1956) 1000–1003.
https://doi.org/10.1103/PhysRev.102.1000.
[81] S. Foner, High-field antiferromagnetic resonance in Cr_2O_3, Physical Review 130 (1963) 183–197.
https://doi.org/10.1103/PhysRev.130.183.
[82] S. Punugupati, J. Narayan, F. Hunte, Strain induced ferromagnetism in epitaxial Cr_2O_3 thin films integrated on Si(001), Applied Physics Letters 105 (2014) 132401.
https://doi.org/10.1063/1.4896975.
[83] D. Halley, N. Najjari, H. Majjad, L. Joly, P. Ohresser, F. Scheurer, C. Ulhaq-Bouillet, S. Berciaud, B. Doudin, Y. Henry, Size-induced enhanced magneto-electric effect and multiferroicity in chromium oxide nanoclusters, Nat Commun 5 (2014) 3167.
https://doi.org/10.1038/ncomms4167.
[84] Z. Yang, J. Zhang, D. Gao, Z. Zhu, G. Yang, D. Xue, Unexpected surface super-paramagnetism in antiferromagnetic Cr_2O_3 nanoparticles, RSC Advances 5 (2015) 46705–46710.
https://doi.org/10.1039/C5RA04009D.
[85] X. Pang, K. Gao, A.A. Volinsky, Microstructure and mechanical properties of chromium oxide coatings, J. Mater. Res. 22 (2007) 3531–3537.
https://doi.org/10.1557/JMR.2007.0445.
[86] A.B. Khelifa, S. Khamlich, Z.Y. Nuru, L. Kotsedi, A. Mebrahtu, M. Balgouthi, A.A. Guizani, W. Dimassi, M. Maaza, Growth and characterization of spectrally selective Cr_2O_3/Cr/Cr_2O_3 multilayered solar absorber by e-beam evaporation, Journal of Alloys and Compounds 734 (2018) 204–209.
https://doi.org/10.1016/j.jallcom.2017.11.036.
[87] A.S. Kao, M.F. Doerner, V.J. Novotny, Processing effects on the tribological characteristics of reactively sputtered chromium oxide (Cr_2O_3) overcoat films, Journal of Applied Physics 66 (1989) 5315–5321.
https://doi.org/10.1063/1.343722.
[88] F. Luo, X. Pang, K. Gao, H. Yang, Y. Wang, Role of deposition parameters on microstructure and mechanical properties of chromium oxide coatings, Surface and Coatings Technology 202 (2007) 58–62.
https://doi.org/10.1016/j.surfcoat.2007.04.066.

[89] K. Khojier, H. Savaloni, Z. Ashkabusi, N.Z. Dehnavi, Structural, mechanical and tribological characterization of chromium oxide thin films prepared by post-annealing of Cr thin films, Applied Surface Science 284 (2013) 489–496. https://doi.org/10.1016/j.apsusc.2013.07.123.

[90] I. Saeki, T. Ohno, D. Seto, O. Sakai, Y. Sugiyama, T. Sato, A. Yamauchi, K. Kurokawa, M. Takeda, T. Onishi, Measurement of Young's modulus of oxides at high temperature related to the oxidation study, Materials at High Temperatures 28 (2011) 264–268. https://doi.org/10.3184/096034011X13182685579795.

[91] R.E. Kirby, E.L. Garwin, F.K. King, A.R. Nyaiesh, Surface properties of Cr_2O_3, Journal of Applied Physics 62 (1987) 1400–1405. https://doi.org/10.1063/1.339644.

[92] B. Karlsson, C.G. Ribbing, Optical constants and spectral selectivity of stainless steel and its oxides, Journal of Applied Physics 53 (1982) 6340–6346. https://doi.org/10.1063/1.331503.

[93] Y. Marinova, J.M. Hohemberger, E. Cordoncillo, P. Escribano, J.B. Carda, Study of solid solutions, with perovskite structure, for application in the field of the ceramic pigments, Journal of the European Ceramic Society 23 (2003) 213–220. https://doi.org/10.1016/S0955-2219(02)00182-6.

[94] M.M. Abdullah, F.M. Rajab, S.M. Al-Abbas, Structural and optical characterization of Cr 2 O 3 nanostructures: Evaluation of its dielectric properties, AIP Advances 4 (2014) 027121. https://doi.org/10.1063/1.4867012.

[95] T. Ivanova, K. Gesheva, A. Cziraki, A. Szekeres, E. Vlaikova, Structural transformations and their relation to the optoelectronic properties of chromium oxide thin films, Journal of Physics: Conference Series 113 (2008) 012030. https://doi.org/10.1088/1742-6596/113/1/012030.

[96] T. Ivanova, M. Surtchev, K. Gesheva, Characterization of CVD Chromium Oxide Thin Films, Phys. Stat. Sol. (a) 184 (2001) 507–513. https://doi.org/10.1002/1521-396X(200104)184:2<507::AID-PSSA507>3.0.CO;2-O

[97] P. Hones, M. Diserens, F. Lévy, Characterization of sputter-deposited chromium oxide thin films, Surface and Coatings Technology 120–121 (1999) 277–283. https://doi.org/10.1016/S0257-8972(99)00384-9.

[98] P. Hones, F. Lévy, N.X. Randall, Influence of deposition parameters on mechanical properties of sputter-deposited Cr_2O_3 thin films, Journal of Materials Research 14 (1999) 3623–3629. https://doi.org/10.1557/JMR.1999.0489.

[99] M. Mohammadtaheri, Q. Yang, Y. Li, J. Corona-Gomez, The effect of deposition parameters on the structure and mechanical properties of chromium oxide coatings deposited by reactive magnetron sputtering, Coatings 8 (2018) 111. https://doi.org/10.3390/coatings8030111.

[100] F. Hajakbari, A. Hojabri, Investigation of Structural, morphological and optical properties of chromium oxide thin films prepared at different annealing times, Journal of Applied Chemical Research 12 (2918) 58–67. https://api.semanticscholar.org/corpusID:54768509.

[101] A.V. Almaev, B.O. Kushnarev, E.V. Chernikov, V.A. Novikov, P.M. Korusenko, S.N. Nesov, Structural, electrical and gas-sensitive properties of Cr_2O_3 thin films, Superlattices and Microstructures 151 (2021) 106835. https://doi.org/10.1016/j.spmi.2021.106835.

[102] T.I. Gandhi, R. Ramesh Babu, K. Ramamurthi, Structural, morphological, electrical and optical studies of Cr doped SnO_2 thin films deposited by the spray pyrolysis technique, Materials Science in Semiconductor Processing 16 (2013) 472–479. https://doi.org/10.1016/j.mssp.2012.07.008.

[103] P. Bhardwaj, J. Singh, R. Kumar, R. Kumar, V. Verma, Structural, optical and magnetic characterization of Ni2+ ions doped chromium oxide (Cr_2O_3) nanoparticles, Solid State Sciences 115 (2021) 106581. https://doi.org/10.1016/j.solidstatesciences.2021.106581.

[104] D. Mardare, G.I. Rusu, F. Iacomi, M. Girtan, I. Vida-Simiti, Chromium-doped titanium oxide thin films, Materials Science and Engineering: B 118 (2005) 187–191. https://doi.org/10.1016/j.mseb.2004.12.083.

[105] H.D. Liu, Q. Wan, B.Z. Lin, L.L. Wang, X.F. Yang, R.Y. Wang, D.Q. Gong, Y.B. Wang, F. Ren, Y.M. Chen, X.D. Cheng, B. Yang, The spectral properties and thermal stability of CrAlO-based solar selective absorbing nanocomposite coating, Solar Energy Materials and Solar Cells 122 (2014) 226–232. https://doi.org/10.1016/j.solmat.2013.12.010.

[106] A. Zhussupbekova, K. Zhussupbekov, R. Verre, D. Caffrey, K. Shiel, I.V. Shvets, K. Fleischer, An in situ study of precursor decomposition via refractive index sensing in p-type transparent copper chromium oxide, Chemistry of Materials 34 (2022) 3020–3027. https://doi.org/10.1021/acs.chemmater.1c03910.

[107] J.M. Kalita, M.P. Sarma, G. Wary, Electrical conductivity and X-ray sensing properties of TiO_2:Cr thin film synthesised by chemical bath deposition method, Thin Solid Films 726 (2021) 138656. https://doi.org/10.1016/j.tsf.2021.138656.

[108] A.D. Kahraman, C. Yolcu, F. Kahraman, Effect of the loads on the wear resistance of the Cr_2O_3–TiO_2 coated AA 6082 alloy under unlubricated conditions, Materials Research Express 6 (2019) 086559. https://doi.org/10.1088/2053-1591/ab1d23.

[109] P. Bagde, S.G. Sapate, R.K. Khatirkar, N. Vashishtha, S. Tailor, Friction and wear behaviour of plasma sprayed Cr_2O_3-TiO_2 coating, Materials Research Express 5 (2018) 026410. https://doi.org/10.1088/2053-1591/aaacf4.

[110] P. Baraskar, R. Chouhan, A. Agrawal, R.J. Choudhary, P. Sen, Weak ferromagnetism at room temperature in Ti incorporated Cr_2O_3 thin film, Physica B: Condensed Matter 571 (2019) 36–40. https://doi.org/10.1016/j.physb.2019.06.031.

[111] A. Zekaik, H. Benhebal, B. Benrabah, A. Chibout, N. Tayebi, A. Kharroubi, A. Ammari, C. Dalache, Sol–Gel Synthesis of Nickel-Doped Cr_2O_3 Thin Films, Journal of Molecular and Engineering Materials 05 (2017) 1750012. https://doi.org/10.1142/S2251237317500125.

[112] C.M. Koller, V. Dalbauer, A. Schmelz, R. Raab, P. Polcik, J. Ramm, P.H. Mayrhofer, Structure, mechanical properties, and thermal stability of arc evaporated $(Al_{1-x}Cr_x)_2O_3$ coatings, Surface and Coatings Technology 342 (2018) 37–47. https://doi.org/10.1016/j.surfcoat.2018.02.077.

[113] K. Pedersen, J. Bøttiger, M. Sridharan, M. Sillassen, P. Eklund, Texture and microstructure of Cr_2O_3 and $(Cr,Al)_2O_3$ thin films deposited by reactive inductively coupled plasma magnetron sputtering, Thin Solid Films 518 (2010) 4294–4298. https://doi.org/10.1016/j.tsf.2010.01.008.

[114] L. Mao, J. Xiao, G. Sun, X. Wei, D. Wu, P. Cao, C. Zhang, Microstructure and wear behaviors of Cr_2O_3-Al_2O_3 composite coatings deposited by atmospheric plasma spraying, Surface and Coatings Technology 444 (2022) 128619. https://doi.org/10.1016/j.surfcoat.2022.128619.

[115] S. Ponmudi, R. Sivakumar, C. Sanjeeviraja, C. Gopalakrishnan, T. Okamoto, Development of room temperature sensor based on high quality rhombohedral Al_2O_3:Cr_2O_3 (1:1) thin film with bone-like morphological feature for ultrasensitive detection of NH3 gas, Journal of Materials Science: Materials in Electronics 31 (2020) 10123–10141. https://doi.org/10.1007/s10854-020-03558-6.

[116] B. Warcholinski, A. Gilewicz, A.S. Kuprin, G.N. Tolmachova, V.D. Ovcharenko, T.A. Kuznetsova, T.I. Zubar, A.L. Khudoley, S.A. Chizhik, Mechanical properties of Cr-O-N coatings deposited by cathodic arc evaporation, Vacuum 156 (2018) 97–107. https://doi.org/10.1016/j.vacuum.2018.07.017.

[117] S. Spitz, M. Stueber, H. Leiste, S. Ulrich, H.J. Seifert, Microstructure evolution of radio-frequency magnetron sputtered oxide thin films in the Cr–Zr–O system, Thin Solid Films 548 (2013) 143–149. https://doi.org/10.1016/j.tsf.2013.09.038.

[118] D. Levchuk, H. Bolt, M. Döbeli, S. Eggenberger, B. Widrig, J. Ramm, Al–Cr–O thin films as an efficient hydrogen barrier, Surface and Coatings Technology 202 (2008) 5043–5047. https://doi.org/10.1016/j.surfcoat.2008.05.012.

[119] A. Khatibi, A. Genvad, E. Göthelid, J. Jensen, P. Eklund, L. Hultman, Structural and mechanical properties of corundum and cubic $(Al_x\ Cr_{1-x})_{2+y}O_{3-y}$ coatings grown by reactive cathodic arc evaporation in as-deposited and annealed states, Acta Materialia 61 (2013) 4811–4822. https://doi.org/10.1016/j.actamat.2013.05.002.

[120] A. Khatibi, J. Palisaitis, C. Höglund, A. Eriksson, P.O.Å. Persson, J. Jensen, J. Birch, P. Eklund, L. Hultman, Face-centered cubic $(Al_{1-x}Cr_x)_2O_3$, Thin Solid Films 519 (2011) 2426–2429. https://doi.org/10.1016/j.tsf.2010.11.052.

[121] N. Uekawa, K. Kaneko, Dopant Reduction in p-Type Oxide Films upon Oxygen Absorption, The Journal of Physical Chemistry 100 (1996) 4193–4198. https://doi.org/10.1021/jp952784m.

[122] D. Mercier, R. Zazpe, X. Wang, M. Michaux, J. Rodriguez-Pereira, S. Zanna, A. Seyeux, J.M. Macak, P. Marcus, Enhanced corrosion resistance of 2024 aluminum alloys with Cr_2O_3 thin layers by Atomic Layer Deposition, Corrosion Science 256 (2025) 113167. https://doi.org/10.1016/j.corsci.2025.113167.

[123] T.S. Tripathi, J.-P. Niemelä, M. Karppinen, Atomic layer deposition of transparent semiconducting oxide $CuCrO_2$ thin films, Journal of Materials Chemistry C 3 (2015) 8364–8371. https://doi.org/10.1039/C5TC01384D.

[124] V. Sammelselg, A. Tarre, J. Lu, J. Aarik, A. Niilisk, T. Uustare, I. Netšipailo, R. Rammula, R. Pärna, A. Rosental, Structural characterization of TiO_2–Cr_2O_3 nano-laminates grown by atomic layer deposition, Surface and Coatings Technology 204 (2010) 2015–2018. https://doi.org/10.1016/j.surfcoat.2009.11.039.

[125] R. Pärna, A. Tarre, A. Gerst, H. Mändar, A. Niilisk, T. Uustare, A. Rosental, V. Sammelselg, Influence of annealing on atomic layer deposited Cr_2O_3-TiO_2 thin films, Optoelectronic Materials and Devices, Proceedings of SPIE 6596 (2006) 659618.
https://doi.org/10.1117/12.726496.
[126] Yu.K. Ezhovskii, Surface modification of silicate matrices with chromium oxides, Russian Journal of Physical Chemistry A 89 (2015) 1471–1475.
https://doi.org/10.1134/S0036024415080117.
[127] J.-H. Kim, J.-C. Kang, The chromium accumulation and its physiological effects in juvenile rockfish, Sebastes schlegelii , exposed to different levels of dietary chromium (Cr (6+)) concentrations, Environmental Toxicology and Pharmacology 41 (2016) 152–158.
https://doi.org/10.1016/j.etap.2015.12.001.
[128] L.B. Paiva, J.G. de Oliveira, R.A. Azevedo, D.R. Ribeiro, M.G. da Silva, A.P. Vitória, Ecophysiological responses of water hyacinth exposed to Cr3+ and Cr6+, Environmental and Experimental Botany 65 (2009) 403–409.
https://doi.org/10.1016/j.envexpbot.2008.11.012.
[129] H. Oliveira, T.M. Santos, J. Ramalho-Santos, M. de Lourdes Pereira, Histopathological Effects of Hexavalent Chronium in Mouse Kidney, Bulletin of Environmental Contamination and Toxicology 76 (2006) 977–983.
https://doi.org/10.1007/s00128-006-1014-y.
[130] Yu.K. Ezhovskii, V.Yu. Kholkin, The preparation and properties of chromium oxide nanolayers on semiconducting matrices, Russian Journal of Physical Chemistry A 82 (2008) 1154–1158.
https://doi.org/10.1134/S0036024408070170.
[131] S. Götzendörfer, C. Polenzky, S. Ulrich, P. Löbmann, Preparation of $CuAlO_2$ and $CuCrO_2$ thin films by sol–gel processing, Thin Solid Films 518 (2009) 1153–1156.
https://doi.org/10.1016/j.tsf.2009.02.153.
[132] H.-Y. Chen, K.-P. Chang, Influence of post-annealing conditions on the formation of delafossite-$CuCrO_2$ films, ECS Journal of Solid State Science and Technology 2 (2013) P76–P80.
https://doi.org/10.1149/2.014303jss.
[133] J.S. Ponraj, G. Attolini, M. Bosi, Review on atomic layer deposition and applications of oxide thin films, Critical Reviews in Solid State and Materials Sciences 38 (2013) 203–233.
https://doi.org/10.1080/10408436.2012.736886.
[134] H. Ryu, S. Kim, Irregular resistive switching behaviors of Al_2O_3-based resistor with Cu electrode, Metals 11 (2021) 653.
https://doi.org/10.3390/met11040653.
[135] D. He, Y. Lei, C. Zhang, S. Li, X. Liu, H. Zhang, Q. Lv, Y. Wu, L. Jiang, Deuterium permeation of Al_2O_3/Cr_2O_3 composite film on 316L stainless steel, International Journal of Hydrogen Energy 40 (2015) 2899–2903.
https://doi.org/10.1016/j.ijhydene.2014.12.058.
[136] V.P. Singh, A. Sil, R. Jayaganthan, Wear of Plasma Sprayed Conventional and Nanostructured Al_2O_3 and Cr_2O_3 Based Coatings, Transactions of the Indian Institute of Metals 65 (2012) 1–12.
https://doi.org/10.1007/s12666-011-0070-0.

[137] M. O. Onoriode-Afunezie, P. Urbanskis, I. Urniežaitė, A. Šulčiūtė, Optimized TiO_2 coatings on AISI 316 Steel for advanced photocatalytic wastewater treatment: mechanism and performance, ACS Omega 10 (2025) 34666–34682. https://doi.org/10.1021/acsomega.5c03565.
[138] S. Jafari, B. Mahyad, H. Hashemzadeh, S. Janfaza, T. Gholikhani, L. Tayebi, Biomedical Applications of TiO_2 Nanostructures: Recent Advances, International Journal of Nanomedicine 15 (2020) 3447-3470. https://doi.org/10.2147/IJN.S249441.
[139] B. Jalvo, M. Faraldos, A. Bahamonde, R. Rosal, Antimicrobial and antibiofilm efficacy of self-cleaning surfaces functionalized by TiO_2 photocatalytic nanoparticles against Staphylococcus aureus and Pseudomonas putida, Journal of Hazardous Materials 340 (2017) 160–170. https://doi.org/10.1007/s10971-010-2387-2.
[140] F. Ali, D. Zhou, M. Ali, H.W. Ali, M. Daaim, S. Khan, M.M. Hussain, N. Sun, Recent progress on energy-related applications of HfO_2-based ferroelectric and antiferroelectric materials, ACS Applied Electronic Materials 2 (2020) 2301–2317. https://doi.org/10.1021/acsaelm.0c00304.
[141] F. Ali, X. Liu, D. Zhou, X. Yang, J. Xu, T. Schenk, J. Müller, U. Schroeder, F. Cao, X. Dong, Silicon-doped hafnium oxide anti-ferroelectric thin films for energy storage, Journal of Applied Physics 122 (2017) 144105. https://doi.org/10.1063/1.4989908.
[142] W. Banerjee, A. Kashir, S. Kamba, Hafnium Oxide (HfO2) – A multifunctional oxide: A review on the prospect and challenges of hafnium oxide in resistive switching and ferroelectric memories, Small 18 (2022) 2107575. https://doi.org/10.1002/smll.202107575.
[143] J.H. Choi, Y. Mao, J.P. Chang, Development of hafnium based high-k materials—A review, Materials Science and Engineering: R: Reports 72 (2011) 97–136. https://doi.org/10.1016/j.mser.2010.12.001.
[144] E. Marguí, I. Queralt, E. de Almeida, X-ray fluorescence spectrometry for environmental analysis: Basic principles, instrumentation, applications and recent trends, Chemosphere 303 (2022) 135006. https://doi.org/10.1016/j.chemosphere.2022.135006.
[145] W.L. Bragg, The diffraction of short electromagnetic waves by a crystal, Proceedings of the Cambridge Philosophical Society 17, 43–57 (1913). Communicated by Professor Sir J. J. Thomson. Read 11 November 1912., in: X-Ray and Neutron Diffraction, Elsevier (1966) 109–125. https://doi.org/10.1016/B978-0-08-011999-1.50015-8.
[146] J. Epp, X-ray diffraction (XRD) techniques for materials characterization, in: Materials Characterization Using Nondestructive Evaluation (NDE) Methods, Elsevier (2016) 81–124. https://doi.org/10.1016/B978-0-08-100040-3.00004-3.
[147] M.R. Sardela, X-Ray Diffraction and Reflectivity, in: M. Sardela (Ed.), Practical Materials Characterization, Springer New York, New York, NY, (2014) 1–41. https://doi.org/10.1007/978-1-4614-9281-8_1.
[148] P. Colombi, P. Zanola, E. Bontempi, R. Roberti, M. Gelfi, L.E. Depero, Glancing-incidence X-ray diffraction for depth profiling of polycrystalline layers, Journal of Applied Crystallography 39 (2006) 176–179. https://doi.org/10.1107/S0021889805042779.

[149] I. Saito, T. Miyazaki, K. Yamamoto, Depth-Resolved Structure Analysis of Cylindrical Microdomain in Block Copolymer Thin Film by Grazing-Incidence Small-Angle X-ray Scattering Utilizing Low-Energy X-rays, Macromolecules 48 (2015) 8190–8196. https://doi.org/10.1021/acs.macromol.5b01883.
[150] V. Valvoda, M. Järvinen, On the harris texture index, Powder Diffraction 5 (1990) 200–203. https://doi.org/10.1017/S0885715600015797.
[151] A.L. Patterson, The Scherrer formula for X-ray particle size determination, Physical Review 56 (1939) 978–982. https://doi.org/10.1103/PhysRev.56.978.
[152] A.W. Burton, K. Ong, T. Rea, I.Y. Chan, On the estimation of average crystallite size of zeolites from the Scherrer equation: A critical evaluation of its application to zeolites with one-dimensional pore systems, Microporous and Mesoporous Materials 117 (2009) 75–90. https://doi.org/10.1016/j.micromeso.2008.06.010.
[153] M. Yasaka, X-ray thin-film measurement techniques, The Rigaku Journal 26.2 (2010) 1–9.
[154] J. Yano, V.K. Yachandra, X-ray absorption spectroscopy, Photosynthesis Research102 (2009) 241–254. https://doi.org/10.1007/s11120-009-9473-8.
[155] F.A. Stevie, R. Garcia, J. Shallenberger, J.G. Newman, C.L. Donley, Sample handling, preparation and mounting for XPS and other surface analytical techniques, Journal of Vacuum Science and Technology A: Vacuum, Surfaces, and Films 38 (2020) 063202. https://doi.org/10.1116/6.0000421.
[156] B. Bhushan, Depth-sensing nanoindentation measurement techniques and applications, Microsystem Technologies 23 (2017) 1595–1649. https://doi.org/10.1007/s00542-017-3372-2.
[157] W.C. Oliver, G.M. Pharr, Measurement of hardness and elastic modulus by instrumented indentation: Advances in understanding and refinements to methodology, Journal of Materials Research 19 (2004) 3-20. https://doi.org/10.1557/jmr.2004.19.1.3.
[158] G.M. Pharr, W.C. Oliver, Measurement of Thin Film Mechanical Properties Using Nanoindentation, MRS Bulletin 17 (1992) 28–33. https://doi.org/10.1557/S0883769400041634.
[159] S. Zhang, Nanostructured thin films and coatings: mechanical properties, Boca Raton (FL): CRC Press (2010).
[160] R. Saha, W.D. Nix, Effects of the substrate on the determination of thin film mechanical properties by nanoindentation, Acta Materialia 50 (2002) 23–38. https://doi.org/10.1016/S1359-6454(01)00328-7.
[161] M.G. Tsegay, H.G. Gebretinsae, G. G.Welegergs, M. Maaza, Z.Y. Nuru, Novel green synthesized Cr2O3 for selective solar absorber: Investigation of structural, morphological, chemical, and optical properties, Solar Energy 236 (2022) 308–319. https://doi.org/10.1016/j.solener.2022.03.011.
[162] Ł. Haryński, A. Olejnik, K. Grochowska, K. Siuzdak, A facile method for Tauc exponent and corresponding electronic transitions determination in semiconductors directly from UV–Vis spectroscopy data, Optical Materials 127 (2022) 112205. https://doi.org/10.1016/j.optmat.2022.112205.
[163] William D. Callister-Materials Science and Engineering (9th ed.), Wiley (2014).

[164] T. Arroval, L. Aarik, R. Rammula, V. Kruusla, J. Aarik, Effect of substrate-enhanced and inhibited growth on atomic layer deposition and properties of aluminum–titanium oxide films, Thin Solid Films 600 (2016) 119–125. https://doi.org/10.1016/j.tsf.2016.01.024.
[165] H. Mändar, J. Felsche, V. Mikli, T. Vajakas, AXES 1.9: new tools for estimation of crystallite size and shape by Williamson–Hall analysis, Journal of Applied Crystallography 32 (1999) 345–350. https://doi.org/10.1107/S0021889898011170.
[166] S. Tanuma, C.J. Powell, D.R. Penn, Calculations of electron inelastic mean free paths. V. Data for 14 organic compounds over the 50–2000 eV range, Surface and Interface Analysis 21 (1994) 165–176. https://doi.org/10.1002/sia.740210302.
[167] G. Greczynski, L. Hultman, X-ray photoelectron spectroscopy: Towards reliable binding energy referencing, Progress in Materials Science 107 (2020) 100591. https://doi.org/10.1016/j.pmatsci.2019.100591.
[168] P. Vasconcelos Borges Pinho, A. Chartier, J.-B. Moussy, D. Menut, F. Miserque, Crystal field effects on the photoemission spectra in Cr_2O_3 thin films: From multiplet splitting features to the local structure, Materialia 12 (2020) 100753. https://doi.org/10.1016/j.mtla.2020.100753.
[169] P.V.B. Pinho, A. Chartier, F. Miserque, D. Menut, J.-B. Moussy, Impact of epitaxial strain on crystal field splitting of α-Cr_2O_3 (0001) thin films quantified by X-ray photoemission spectroscopy, Materials Research Letters 9 (2021) 163–168. https://doi.org/10.1080/21663831.2020.1863877.
[170] H.C. Aspinall, Requirements of Precursors for MOCVD and ALD of rare earth oxides, in: M. Fanciulli, G. Scarel (Eds.), Rare Earth Oxide Thin Films, Springer Berlin Heidelberg, (2006) 53–72. https://doi.org/10.1007/11499893_4.
[171] C.D. Travis, R.A. Adomaitis, Modeling alumina atomic layer deposition reaction kinetics during the trimethylaluminum exposure, Theoretical Chemistry Accounts 133 (2014) 1414. https://doi.org/10.1007/s00214-013-1414-0.
[172] Barry, Seán Thomas. Chemistry of Atomic Layer Deposition, Berlin, Boston: De Gruyter, 2022. https://doi.org/10.1515/9783110712537.
[173] A. Hajjaji, M. Gaidi, B. Bessais, M.A.E. Khakani, Effect of Cr incorporation on the structural and optoelectronic properties of TiO_2:Cr deposited by means of a magnetron co-sputtering process, Applied Surface Science 257 (2011) 10351–10357. https://doi.org/10.1016/j.apsusc.2011.06.072.
[174] B. Nalcaci, M. Polat Gonullu, Insight of mechanical and morphological properties of ALD- Al_2O_3 films in point of structural properties, Appl. Phys. A 127 (2021) 460. https://doi.org/10.1007/s00339-021-04601-x.
[175] L. Aarik, H. Mändar, A. Tarre, H.-M. Piirsoo, J. Aarik, Mechanical properties of crystalline and amorphous aluminum oxide thin films grown by atomic layer deposition, Surface and Coatings Technology 438 (2022) 128409. https://doi.org/10.1016/j.surfcoat.2022.128409.
[176] C.S. Pande, K.P. Cooper, Nanomechanics of Hall–Petch relationship in nanocrystalline materials, Progress in Materials Science 54 (2009) 689–706. https://doi.org/10.1016/j.pmatsci.2009.03.008.

[177] S.N. Naik, S.M. Walley, The Hall–Petch and inverse Hall–Petch relations and the hardness of nanocrystalline metals, Journal of Materials Science 55 (2020) 2661–2681.
https://doi.org/10.1007/s10853-019-04160-w.
[178] L. Wang, G. Zhang, R.J.K. Wood, S.C. Wang, Q. Xue, Fabrication of CrAlN nanocomposite films with high hardness and excellent anti-wear performance for gear application, Surface and Coatings Technology 204 (2010) 3517–3524.
https://doi.org/10.1016/j.surfcoat.2010.04.014.
[179] M. Diserens, J. Patscheider, F. Lévy, Mechanical properties and oxidation resistance of nanocomposite TiN–SiNx physical-vapor-deposited thin films, Surface and Coatings Technology 120–121 (1999) 158–165.
https://doi.org/10.1016/S0257-8972(99)00481-8.
[180] Z. Wang, P. Gu, X. Wu, H. Zhang, Z. Zhang, M.Y.M. Chiang, Micro/nano-wear studies on epoxy/silica nanocomposites, Composites Science and Technology 79 (2013) 49–57.
https://doi.org/10.1016/j.compscitech.2013.02.010.
[181] K. Kato, K. Adachi, Wear of advanced ceramics, Wear 253 (2002) 1097–1104.
https://doi.org/10.1016/S0043-1648(02)00240-5.
[182] K.S. Shamala, L.C.S. Murthy, K. Narasimha Rao, Studies on optical and dielectric properties of Al_2O_3 thin films prepared by electron beam evaporation and spray pyrolysis method, Materials Science and Engineering: B 106 (2004) 269–274.
https://doi.org/10.1016/j.mseb.2003.09.036.
[183] P.M. Sousa, S.A. Dias, O. Conde, A.J. Silvestre, W.R. Branford, B. Morris, K.A. Yates, L.F. Cohen, Influence of growth temperature and carrier flux on the structure and transport properties of highly oriented CrO_2 on Al_2O_3 (0001), Chemical Vapour Deposition 13 (2007) 537-545.
https://doi.org/10.1002/cvde.200706592.
[184] A.M. Minyukhina, A.K. Busova, R.I. Korolev, B.A. Makeev, R.N. Skandakov, S.V. Nekipelov, N.A. Zhuk, Oxidation of Cr(III) to Cr(VI) in the synthesis of Bismuth-chromium oxide ceramics, Glass and Ceramics 7–8 (2024).
https://doi.org/10.1007/s10717-024-00695-w
[185] M.O.J.Y. Hunault, Y. Harada, J. Miyawaki, J. Wang, A. Meijerink, F.M.F. de Groot, M.M. van Schooneveld, Direct observation of Cr3+ 3d States in ruby: toward experimental mechanistic evidence of metal chemistry, The Journal of Physical Chemistry A 122 (2018) 4399–4413.
https://doi.org/10.1021/acs.jpca.8b00984.
[186] M.K. Khalaf, D. S. ABD al-kader, J.M. Salh, Annealing effect on structural and optical properties of Cr_2O_3 thin films prepared by R.F magnetron sputtering, IOP Conference Series: Materials Science and Engineering 1105 (2021) 012064.
https://doi.org/10.1088/1757-899X/1105/1/012064.
[187] G. S, D. Kekuda, Improving functional properties in Cr_2O_3 thin films through annealing: a route toward sustainable materials engineering, Applied Physics A 132 (2026) 343.
https://doi.org/10.1007/s00339-026-09533-y.
[188] H.C. Barshilia, K.S. Rajam, Growth and characterization of chromium oxide coatings prepared by pulsed-direct current reactive unbalanced magnetron sputtering, Applied Surface Science 255 (2008) 2925–2931.
https://doi.org/10.1016/j.apsusc.2008.08.057.

[189] V.K. Malinovsky, V.N. Novikov, N.V. Surovtsev, A.P. Shebanin, Investigation of amorphous states of SiO_2 by raman scattering spectroscopy, Physics of the Solid State 42 (2000) 65–71. https://doi.org/10.1134/1.1131169.
[190] M. Sabzi, S. Mousavi Anijdan, M. Shamsodin, M. Farzam, A. Hojjati-Najafabadi, P. Feng, N. Park, U. Lee, A review on sustainable manufacturing of ceramic-based thin films by chemical vapor deposition (CVD): reaction kinetics and the deposition mechanisms, Coatings 13 (2023) 188. https://doi.org/10.3390/coatings13010188.

COPIES of ORIGINAL PUBLICTIONS

CURRICULUM VITAE

Name: Salari Mehr Mahtab
ORCID: 0000-0002-9338-006X
Date of birth: 05.11.1991

Degrees

Doctoral Candidate in Materials Science (Sep 2021 – Aug 2026)

Laboratory of Thin Film Technology, Institute of Physics, University of Tartu, Tartu, Estonia.

M.Sc. Materials Engineering-Nanomaterials (Sep 2014 – Feb 2017)

Faculty of Materials Engineering, Sahand University of Technology, Tabriz, Iran

Other education and expertise

Visiting Researcher (Nov 2025–present)

Department of Chemistry and Materials Science, Aalto University, Espoo, Finland.

Language skills

Turkish (native language)

Persian (native language)

English (full working proficiency; C1)

Estonian (Basic; A2)

Finnish (Basic; A1)

Current employment

Visiting Researcher (Nov 2025–present)

Department of Chemistry and Materials Science, Aalto University, Espoo, Finland.

Doctoral Candidate in Materials Science (Sep 2021 – August 2026)

Laboratory of Thin Film Technology, Institute of Physics, University of Tartu,Tartu, Estonia.

Previous work experience

Project Support Specialist and Researcher (Nov 2024 – Oct 2025)

Laboratory of Thin Film Technology, Institute of Solid State Physics, University of Latvia, Riga, Latvia.

Materials Engineer (Sep 2014 – Feb 2017)

Faculty of Materials Engineering, Sahand University of Technology, Tabriz, Iran

Research funding and grants

AVS ALD/ALE 2025 Student/postdoc travel grant for participation in the AVS 25th International Conference on Atomic Layer Deposition conference, Jeju Island, South Korea (June 2025).

Estonian Doctoral School Mobility Grant for participation in the EuroCVD&ALD conference, Catania, Italy (June 2025)

Cost Action Opera travel grant for participation in training school "Characterization Techniques for Epitaxial Materials", University of Aveiro, Portugal (June 2023)

Erasmus grant winner for participating in the School of Self-Organization and Nanolithography at Paderborn University, Germany (March 2023).

Research output

Mahtab Salari Mehr, Lauri Aarik, Taivo Jõgiaas, Aarne Kasikov, Tanel Käämbre, Rainer Pärna, Ramin Ghiyasi, Maarit Karppinen, Hugo Mändar, "Structural, Mechanical, and Optical properties of Atomic Layer Deposited $(Cr_{1-x}Al_x)_2O_3$ films on sapphire substrates", Materials Advances, 2026 (accepted, in print)

Martins Zubkins, Mahtab Salari Mehr, Viktors Vibornijs, Emija Letko, Edvards Strods, Anatolijs Sarakovskis, Karlis Kundzins, Smagul Karazhanov, Juris Purans, Nanocrystalline Photochromic LaHO Films with Rapid Optical Recovery for Passive Light-Control Coatings, ACS Applied Nano Materials, 9 (2026) 7459–7468, https://doi.org/10.1021/acsanm.5c05856.

Mahtab Salari Mehr, Alireza Akbari, "Optimization and Characterization of Ni-B/SiC Nanocomposite Coatings: Effects of Deposition Parameters on Hardness and Corrosion Resistance", Protection of Metals and Physical Chemistry of Surfaces, 61 (2025) 368–380, https://doi.org/10.1134/S2070205125700224.

Mahtab Salari Mehr, Lauri Aarik, Taivo Jõgiaas, Aarne Kasikov, Jekaterina Kozlova, Loïc Vidal, Karine Mougin, Hugo Mändar, "Atomic Layer Deposition, Mechanical, Wear Resistance, and Optical Properties of $(Cr_{1-x}Al_x)_2O_3$ Films on Si (100)", 50 (2024) 50367–50376, Ceramics International, https://doi.org/10.1016/j.ceramint.2024.09.382.

Mahtab Salari Mehr, Lauri Aarik, Taivo Jõgiaas, Hugo Mändar, "Annealing Effect on Structural and Mechanical Properties of Atomic Layer Deposited Cr_2O_3 Films Doped with Ti and Al", IEEE conference (NAP) Proceedings, 2024, https://doi.org/10.1109/NAP62956.2024.10739705.

Mahtab Salari Mehr, Lauri Aarik, Taivo Jõgiaas, Aivar Tarre, Aarne Kasikov, Kaspar Roosalu, Hugo Mändar, "Ti doped Cr_2O_3 Thin Films: Atomic Layer Deposition, Mechanical and Optical Properties", Journal of Alloys and Compounds, 968 (2023) 172041, https://doi.org/10.1016/j.jallcom.2023.172041.

Mahtab Salari Mehr, Lauri Aarik, Taivo Jõgiaas, Aarne Kasikov, Elyad Damerchi, Hugo Mändar, "Mechanical and Optical Properties of Cr_2O_3 Thin Films Grown by Atomic Layer Deposition Method Using Cr $(thd)_3$ and Ozone." Nanomaterials, 13 (2023) 2702, https://doi.org/10.3390/nano13192702.

Mahtab Salari Mehr, Alireza Akbari, Elyad Damerchi, "Electrodeposition of Ni-B/SiC micro and nano composite coatings: a comparative study." Journal of Alloys and Compounds, 782 (2019) 477–487, https://doi.org/10.1016/j.jallcom.2018.12.184.

Elyad Damerchi, Amir Abdollah-zadeh, Reza Poursalehi, Mahtab Salari Mehr, "Effects of Functionally Graded TiN Layer and Deposition Temperature on the Structure and Surface Properties of TiCN Coating Deposited on Plasma Nitrided H13 Steel by PACVD Method." Journal of Alloys and Compounds, 772 (2019) 612–624, https://doi.org/10.1016/j.jallcom.2018.09.083.

Conferences and workshops

Mahtab Salari Mehr, Lauri Aarik, Taivo Jõgiaas, Hugo Mändar, "Mechanical Properties and Wear Resistance of Atomic Layer Deposited Ternary Cr-Hf-O Films: A Comparative Study with Binary Chromium Oxide and Hafnium Oxide Film", 25th International Conference on Atomic Layer Deposition; ALD/ALE 2025, Jeju Island, South Korea (Oral Presentation).

Mahtab Salari Mehr, Lauri Aarik, Taivo Jõgiaas, Aarne Kasikov, Hugo Mändar, "Atomic Layer Deposition of Hard Epitaxial $(Cr_{1-x}Alx)_2O_3$ Thin Films on Sapphire.", EURO CVD & ALD international conference 2025, Catania, Italy (Oral Presentation).

Mahtab Salari Mehr, Lauri Aarik, Taivo Jõgiaas, Hugo Mändar, "Atomic Layer Deposition, Mechanical Properties and Wear Resistance of Ternary $(Cr_{1-x}Al_x)_2O_3$ Films", 41th International Scientific Conference of ISSP Ul, 2025, Riga, Latvia (Oral Presentation).

Mahtab Salari Mehr, Lauri Aarik, Taivo Jõgiaas, Aarne Kasikov, Jekaterina Kozlova, Hugo Mändar, "Atomic Layer Deposition and Characterization of Chromium-Aluminum Oxide Films", International conferences 'Functional materials and Nanotechnologies-2024' and Nanotechnology and Innovation in the Baltic Sea Region (FMNT& NIBS) 2024, Tartu, Estonia (Oral Presentation).

Mahtab Salari Mehr, Lauri Aarik, Taivo Jõgiaas, Hugo Mändar, "Annealing Effect on Structural and Mechanical Properties of Atomic Layer Deposited Cr_2O_3 Films Doped with Ti and Al", IEEE 14th International Conference "Nanomaterials: Applications & Properties (IEEE NAP)" 2024, Riga, Latvia (Oral Presentation).

Mahtab Salari Mehr, Lauri Aarik, Taivo Jõgiaas, Hugo Mändar, "Tailoring the Properties of Oxide Films by Doping Using Atomic Layer Deposition Method.", 24th International Conference on Atomic Layer Deposition/10th International Atomic Layer Etching Workshop (ALD/ALE), 2024, Helsinki, Finland (Poster Presentation).

International Summer School “Advanced Materials for Chromogenic Device Applications” and “Thin Films: Synthesis and Characterization”, University of Latvia, Riga, Latvia, 2024.

Mahtab Salari Mehr, Lauri Aarik, Taivo Jõgiaas, Hugo Mändar, “The Effect of Dopant Element on Mechanical and Optical Properties of Cr_2O_3 Thin Films”, EuroCVD/Baltic ALD conference, 2023, Leuven, Belgium, (Poster Presentation).

Training School on Characterization Techniques for Epitaxial Materials, University of Aveiro, Portugal, 2023.

Erasmus+ Blended Intensive Program Spring School on Self-Organization and Nanolithography, University of Paderborn, Germany, 2023.

Mahtab Salari Mehr, Lauri Aarik, Taivo Jõgiaas, Hugo Mändar, “Atomic Layer Deposition of the $Cr_xAl_yO_3$ Films”, Graduate School of Functional Materials and Technologies Scientific Conference (GSFMT), 2023, Tartu, Estonia, (Oral Presentation).

Mahtab Salari Mehr, Lauri Aarik, Taivo Jõgiaas, Aivar Tarre, Hugo Mändar, “Effect of precursors on properties of atomic layer deposited Cr-Ti-O thin films”, 22nd International Conference on Atomic Layer Deposition, 2022, Ghent, Belgium, (Poster Presentation).

Mahtab Salari Mehr, Lauri Aarik, Taivo Jõgiaas, Aarne Kasikov, Peeter Ritslaid, Hugo Mändar, “Effect of Ti doping on the microstructure and optical properties of Cr-Ti-O thin films”, Graduate School of Functional Materials and Technologies Scientific Conference (GSFMT), 2022, Tallinn, Estonia, (Poster Presentation).

Teaching merits

Teaching Assistant, Development of Materials II, Institute of Physics, University of Tartu, 2023–2025.

Awards and honors

Awarded for organizing the International Hybrid Summer School in Solar Energy Materials and Smart Devices, University of Latvia, Riga, Latvia, 2025.

Certified for participating in the Horizon Europe Proposal Writing training course, Pillar II, Brussels, Belgium, 2025.

Recipient of an Excellent grade for master’s thesis, 2017.

Ranked 2nd among M.Sc. Materials Engineering-Nanomaterials students, (2015–2017).

Ranked 128th in the National M.Sc. Nanotechnology Examination among 5230 participants, 2014.

Ranked 2nd among B.Sc. Materials Science and Engineering students, 2014.

ELULOOKIRJELDUS

Nimi: Mahtab Salari Mehr
ORCID: 0000-0002-9338-006X
Sünniaeg: 05.11.1991
Kodakondsus: Iraani

Haridus

2021–2026 Tartu Ülikool, füüsika instituut, doktoriõpe,
2014–2017 Magistrantuur, nanomaterjalide inseneeria
Materjalid Inseneeria Teaduskond, Sahand Tehnoloogia Ülikool

Töökogemus

Külalisteadlane (alates november, 2025)
Keemia ja Materjaliteaduse Osakond, Aalto Ülikool, Espoo, Soome.
Abispetsialist ja uurija (november, 2024 – oktoober, 2025)
Kiletehnoloogi labor, Tahke Keha Füüsika Instituut, Läti Ülikool, Riia, Läti
Materjaliteaduse insener (september, 2014 – veebruar 2017)
Materjalid Inseneeria Teaduskond, Sahand Tehnoloogia Ülikool, Tabriz, Iraan

Keelte oskus

Türgi (emakeel)
Pärsia (emakeel)
Inglise (hea, C1)
Eesti (baasteadmised; A2)
Soome (baasteadmised; A1)

Saadud uurimistoetused ja grandid

AVS ALD/ALE 2025 Üliõpilaste ja järeldoktorite reisitoetus osalemiseks AVS 25. rahvusvahelisel aatomkihtsadestamise konverentsil Jeju saarel, Lõuna-Koreas (juuni 2025).

Eesti doktorikooli toetus osalemiseks konverentsil EuroCVD&ALD, Catania, Itaalia (juuni 2025)

Cost Action Opera reisitoetus osalemiseks koolituskoolis „Epitaksiaalsete materjalide iseloomustamise tehnikad“, Aveiro Ülikool, Portugal (juuni 2023)

Erasmuse toetuse võitja osalemiseks iseorganiseerumise ja nanolitograafia koolis Paderborni Ülikoolis, Saksamaal (märts 2023).

Publikatsioonid

Mahtab Salari Mehr, Lauri Aarik, Taivo Jõgiaas, Aarne Kasikov, Tanel Käämbre, Rainer Pärna, Ramin Ghiyasi, Maarit Karppinen, Hugo Mändar, "Structural, Mechanical, and Optical properties of Atomic Layer Deposited $(Cr_{1-x}Al_x)_2O_3$ films on sapphire substrates", Materials Advances, 2026 (avaldamisel).

Martins Zubkins, Mahtab Salari Mehr, Viktors Vibornijs, Emija Letko, Edvards Strods, Anatolijs Sarakovskis, Karlis Kundzins, Smagul Karazhanov, Juris Purans, Nanocrystalline Photochromic LaHO Films with Rapid Optical Recovery for Passive Light-Control Coatings, ACS Applied Nano Materials, 9 (2026) 7459–7468, https://doi.org/10.1021/acsanm.5c05856.

Mahtab Salari Mehr, Alireza Akbari, "Optimization and Characterization of Ni-B/SiC Nanocomposite Coatings: Effects of Deposition Parameters on Hardness and Corrosion Resistance", Protection of Metals and Physical Chemistry of Surfaces, 61 (2025) 368–380, https://doi.org/10.1134/S2070205125700224.

Mahtab Salari Mehr, Lauri Aarik, Taivo Jõgiaas, Aarne Kasikov, Jekaterina Kozlova, Loïc Vidal, Karine Mougin, Hugo Mändar, "Atomic Layer Deposition, Mechanical, Wear Resistance, and Optical Properties of $(Cr_{1-x}Al_x)_2O_3$ Films on Si (100)", 50 (2024) 50367–50376, Ceramics International, https://doi.org/10.1016/j.ceramint.2024.09.382.

Mahtab Salari Mehr, Lauri Aarik, Taivo Jõgiaas, Hugo Mändar, "Annealing Effect on Structural and Mechanical Properties of Atomic Layer Deposited Cr_2O_3 Films Doped with Ti and Al", IEEE conference (NAP) Proceedings, 2024, https://doi.org/10.1109/NAP62956.2024.10739705.

Mahtab Salari Mehr, Lauri Aarik, Taivo Jõgiaas, Aivar Tarre, Aarne Kasikov, Kaspar Roosalu, Hugo Mändar, "Ti doped Cr_2O_3 Thin Films: Atomic Layer Deposition, Mechanical and Optical Properties", Journal of Alloys and Compounds, 968 (2023) 172041, https://doi.org/10.1016/j.jallcom.2023.172041.

Mahtab Salari Mehr, Lauri Aarik, Taivo Jõgiaas, Aarne Kasikov, Elyad Damerchi, Hugo Mändar, "Mechanical and Optical Properties of Cr_2O_3 Thin Films Grown by Atomic Layer Deposition Method Using $Cr(thd)_3$ and Ozone." Nanomaterials, 13 (2023) 2702, https://doi.org/10.3390/nano13192702.

Mahtab Salari Mehr, Alireza Akbari, Elyad Damerchi, "Electrodeposition of Ni-B/SiC micro and nano composite coatings: a comparative study." Journal of Alloys and Compounds, 782 (2019) 477–487, https://doi.org/10.1016/j.jallcom.2018.12.184.

Elyad Damerchi, Amir Abdollah-zadeh, Reza Poursalehi, Mahtab Salari Mehr, "Effects of Functionally Graded TiN Layer and Deposition Temperature on the Structure and Surface Properties of TiCN Coating Deposited on Plasma Nitrided H13 Steel by PACVD Method." Journal of Alloys and Compounds, 772 (2019) 612–624, https://doi.org/10.1016/j.jallcom.2018.09.083.

Konverentsiettekanded

Mahtab Salari Mehr, Lauri Aarik, Taivo Jõgiaas, Hugo Mändar, “Mechanical Properties and Wear Resistance of Atomic Layer Deposited Ternary Cr-Hf-O Films: A Comparative Study with Binary Chromium Oxide and Hafnium Oxide Film”, 25th International Conference on Atomic Layer Deposition; ALD/ALE 2025, Jeju Island, South Korea (Oral Presentation).

Mahtab Salari Mehr, Lauri Aarik, Taivo Jõgiaas, Aarne Kasikov, Hugo Mändar, “Atomic Layer Deposition of Hard Epitaxial (Cr1-xAlx)2O3 Thin Films on Sapphire.”, EURO CVD & ALD international conference 2025, Catania, Italy (Oral Presentation).

Mahtab Salari Mehr, Lauri Aarik, Taivo Jõgiaas, Hugo Mändar, “Atomic Layer Deposition, Mechanical Properties and Wear Resistance of Ternary $(Cr_{1-x}Al_x)_2O_3$ Films”, 41th International Scientific Conference of ISSP Ul, 2025, Riga, Latvia (Oral Presentation).

Mahtab Salari Mehr, Lauri Aarik, Taivo Jõgiaas, Aarne Kasikov, Jekaterina Kozlova, Hugo Mändar, “Atomic Layer Deposition and Characterization of Chromium-Aluminum Oxide Films”, International conferences ‘Functional materials and Nanotechnologies-2024’ and Nanotechnology and Innovation in the Baltic Sea Region (FMNT& NIBS) 2024, Tartu, Estonia (Oral Presentation).

Mahtab Salari Mehr, Lauri Aarik, Taivo Jõgiaas, Hugo Mändar, “Annealing Effect on Structural and Mechanical Properties of Atomic Layer Deposited Cr2O3 Films Doped with Ti and Al”, IEEE 14th International Conference “Nanomaterials: Applications & Properties (IEEE NAP)” 2024, Riga, Latvia (Oral Presentation).

Mahtab Salari Mehr, Lauri Aarik, Taivo Jõgiaas, Hugo Mändar, “Tailoring the Properties of Oxide Films by Doping Using Atomic Layer Deposition Method.”, 24th International Conference on Atomic Layer Deposition/10th International Atomic Layer Etching Workshop (ALD/ALE), 2024, Helsinki, Finland (Poster Presentation).

International Summer School “Advanced Materials for Chromogenic Device Applications” and “Thin Films: Synthesis and Characterization”, University of Latvia, Riga, Latvia, 2024.

Mahtab Salari Mehr, Lauri Aarik, Taivo Jõgiaas, Hugo Mändar, “The Effect of Dopant Element on Mechanical and Optical Properties of Cr_2O_3 Thin Films”, EuroCVD/Baltic ALD conference, 2023, Leuven, Belgium, (Poster Presentation).

Training School on Characterization Techniques for Epitaxial Materials, University of Aveiro, Portugal, 2023.

Erasmus+ Blended Intensive Programme Spring School on Self-Organization and Nanolithography, University of Paderborn, Germany, 2023.

Mahtab Salari Mehr, Lauri Aarik, Taivo Jõgiaas, Hugo Mändar, “Atomic Layer Deposition of the $Cr_xAl_yO_3$ Films”, Graduate School of Functional Materials and Technologies Scientific Conference (GSFMT), 2023, Tartu, Estonia, (Oral Presentation).

Mahtab Salari Mehr, Lauri Aarik, Taivo Jõgiaas, Aivar Tarre, Hugo Mändar, "Effect of precursors on properties of atomic layer deposited Cr-Ti-O thin films", 22nd International Conference on Atomic Layer Deposition, 2022, Ghent, Belgium, (Poster Presentation).

Mahtab Salari Mehr, Lauri Aarik, Taivo Jõgiaas, Aarne Kasikov, Peeter Ritslaid, Hugo Mändar, "Effect of Ti doping on the microstructure and optical properties of Cr-Ti-O thin films", Graduate School of Functional Materials and Technologies Scientific Conference (GSFMT), 2022, Tallinn, Estonia, (Poster Presentation).

Õpetamise kogemus

Õppeassistent "Development of Materials II", Tartu Ülikool, füüsika instituut, 2023–2025.

Auhinnad ja erialased saavutused

Auhinnatud rahvusvahelise hübriidsuvekooli korraldamise eest päikeseenergia materjalide ja nutiseadmete alal, Läti Ülikool, Riia, Läti, 2025.

Sertifitseeritud osalemise eest Horizon Europe'i ettepanekute kirjutamise koolituskursusel, II sammas, Brüssel, Belgia, 2025.

Suurepärase hinde saanud magistritöö eest, 2017.

2. koht materjalitehnika ja nanomaterjalide magistriõppe üliõpilaste seas (2015–2017).

128. koht nanotehnoloogia magistriõppe riiklikul eksamil 5230 osaleja seas, 2014.

2. koht materjaliteaduse ja inseneriteaduse bakalaureuseõppe üliõpilaste seas, 2014.

DISSERTATIONES SCIENTIAE MATERIALIS UNIVERSITATIS TARTUENSIS

1. **Martin Järvekülg**. Tubular microstructures by Hf-, Zr- and Ti-butoxide gel sheet rolling. Tartu, 2011, 112 p.
2. **Sergei Vlassov**. Investigation of nanoscale interactions and mechanical properties of nanostructures using quartz tuning fork based real-time measurements. Tartu, 2011, 171 p.
3. **Margus Kodu**. Pulsed Laser Deposition of Magnesium Oxide and Barium Ternary Oxides for Plasma Display Protective Layers. Tartu, 2011, 89 p.
4. **Rainer Pärna**. Surface studies of some oxide films. Tartu, 2011, 129 p.
5. **Jevgeni Šulga**. Self-assembly and interaction of nanostructures. Tartu, 2011, 114 p.
6. **Wojciech Kuznik**. Quantum-chemical computer simulations of the linear and non-linear optical properties of pyrazoloquinoline and dicyanopyrazine derivatives. Tartu, 2012, 89 p.
7. **Leonid Dorogin**. Structural and tribological properties of zero- and one-dimensional nanocrystals. Tartu, 2012, 193 p.
8. **Viljar Palmre**. Fabrication and characterization of microporous carbon-based electroactive polymer actuators. Tartu, 2012, 99 p.
9. **Madis Paalo**. Synthesis of CNT-metal oxide nanocomposites: sol-gel process, rheology, structural and functional properties. Tartu, 2014, 175 p.
10. **Raul Välbe**. Developement of ionic liquid composites by sol-gel method for elaboration of industrial nano- and microstructures. Tartu, 2014, 97 p.
11. **Urmas Joost**. Impurity and preparation dependent properties of titania thin films. Tartu, 2014, 155 p.
12. **Madis Umalas**. Application of sol-gel technology for production of ceramic nanocomposites and functional coatings. Tartu, 2015, 136 p.
13. **Elena Samsonova**. Energy transfer probe as a tool to study morphological and structural origins of fluorescence quenching in rare-earth doped nanophosphors. Tartu, 2015, 114 p.
14. **Jay Mondal**. Novel Corrosion Protective Nanostructured Composite Coatings. Tartu, 2016, 104 p.
15. **Kathriin Utt**. Metal oxide mesostructures for optical applications. Tartu, 2016, 88 p.
16. **Kaido Siimon**. Electrospun gelatin cross-linked by glucose. Tartu, 2016, 84 p.
17. **Marko Part**. Combined three-dimensional sol-gel structures and atomic layer deposited thin films. Tartu, 2017, 162 p.
18. **Pejman Rasti**. Analysis of Remote Sensing Image Super Resolution using Fluid Lenses. Tartu, 2017, 188 p.
19. **Ivo Romet**. Recombination luminescence of doped borates: origin and application prospects in dosimetry. Tartu, 2017, 111 p.

20. **Vladimir I. Kondratiev**. Processing and characterization of transparent electrode materials. Tartu, 2017, 111 p.
21. **Taivo Jõgiaas**. Mechanical properties of atomic layer deposited thin films and nanocomposites. Tartu, 2017, 125 p.
22. **Lauri Aarik**. Atomic layer deposition and characterization of thin oxide films for application in protective coatings. Tartu, 2017, 180 p.
23. **Triin Kangur**. Preparation and functional properties of stochastic micro-structured sol-gel silica materials. Tartu, 2018, 96 p.
24. **Marta Berholts**. Fragmentation of ionic and hydrogen-bonded molecules induced by synchrotron radiation. Tartu, 2018, 126 p.
25. **Priit Priimägi**. Development and optimization of 3D-microbatteries. Tartu, 2018, 118 p.
26. **Siim Hödemann**. Residual stress determination in chemically strengthened and thermally tempered glass plates using scattered light method. Tartu, 2019, 146 p.
27. **Jekaterina Kozlova**. Complex characterization of graphene structures on nanometer level. Tartu, 2019, 206 p.
28. **Kristjan Kalam**. Magnetic, electric and structural properties of atomic layer deposited zirconia-based nanolaminates and mixtures. Tartu, 2020, 94 p.
29. **Triinu Vihmann**. Ionic liquids: synthesis and application in lubrication and lithography. Tartu, 2020, 102 p.
30. **Helina Seemen**. Atomic layer deposition and microscopic analysis of magnetically and electrically polarizable thin solid films. Tartu, 2021, 126 p.
31. **Ekaterina Vagapova**. Fluorescence quenching in inorganic crystalline solids activated by neodymium ions; from bulk to micro- and nanocrystals. Tartu, 2021, 116 p.
32. **Evgenii Strugovshchikov**. First-principles studies on rare-earth metal-hydride-based smart materials. Tartu, 2021, 166 p.
33. **Maido Merisalu**. Nanostructured Coatings for Car and Aerospace Industries. Tartu, 2022, 179 p.
34. **Elena Vinogradova**. Optical centers and quantum entangled states of Nd3+ ions in doped fluoride crystals. Tartu, 2023, 92 p.
35. **Dmytro Danilian**. "Photocatalytic materials for water treatment and antimicrobial applications". Tartu, 2024, 139 p.
36. **Kristel Möls**. Metastable TiO_2-II in atomic layer deposited thin and ultrathin films: stabilization, properties and impact on film growth. Tartu, 2024, 112 p.
37. **Helle-Mai Piirsoo**. Mechanical Properties of Nanocomposites with Artificial Periodic Structure. Tartu, 2024, 144 p.
38. **Artjom Berholts**. Light-enhanced sensors of oxidizing gases based on single-layer CVD graphene. Tartu, 2024, 97 p.
39. **Alexandra Nefedova**. Oxide nanostructures as antiviral coatings for textiles. Tartu, 2025, 133 p.
40. **Mati Kook**. Photoexcited processes in ionic liquid vapors. Tartu, 2025, 131 p.